



Alessandra Edda Baas

---

Jet Eta Intercalibration of the ATLAS Detector using the  
Trigger Combination Method

Diplomarbeit

HD-KIP 12-78



Department of Physics and Astronomy

University of Heidelberg

Diploma thesis

in Physics

submitted by

Alessandra Edda Baas

born in Cologne

2012



**Jet Pseudorapidity Intercalibration of the ATLAS Detector**  
**using**  
**the Trigger Combination Method**

This diploma thesis has been carried out by Alessandra Edda Baas

at the

Kirchhoff-Institute for Physics

under the supervision of

Prof. Dr. Hans-Christian Schultz-Coulon



## Zusammenfassung

Beim ATLAS Experiment ist die korrekte Energieskala von Jets (JES) und ihre Unsicherheit ein entscheidender Faktor für viele Physikanalysen. Die Interkalibration in der Pseudorapidität von Jets ist eine wichtige in-situ Methode zur Validierung der JES Korrektur und zur Bestimmung ihrer Unsicherheit. In dieser Methode werden die transversalen Impulse von Dijets ausbalanciert.

Diese Arbeit präsentiert eine neue Methode um geeignete Dijetereignisse zu selektieren. Die Standardmethoden der Jet Pseudorapiditätsinterkalibrierung verlangen volleffiziente Jet Trigger innerhalb eines bestimmten transversalen Impuls Bereiches und verlieren aufgrund des sogenannten Prescale-Mechanismus bei der Datennahme Statistik. Die Triggerkombinierungsmethode (TCM) kombiniert viele Jet Trigger, unter der Voraussetzung, dass sie einen voll effizienten Satz von Triggern bilden, um die vorhandenen Ereignisse mit Jets bestmöglich zu nutzen. Dieses Selektionsverfahren wurde auf die Klassische Methode der Jet Pseudorapiditätsinterkalibrierung angewandt. Das resultierende Ansprechverhalten der Kalorimeter auf Jets wurde mit Ergebnissen aus Simulationen und der Standardmethoden verglichen. Beide Vergleiche zeigen sehr gute Übereinstimmungen. Systematische Studien haben kleine systematische Fehler in den zentralen Detektoregionen ergeben, allerdings sind die Unsicherheiten in der Vorwärtsrichtung größer. Der dominierende Beitrag zur Unsicherheit kommt von zusätzlichen weichen Abstrahlungen und kann höchstwahrscheinlich durch weitere systematische Studien reduziert werden. Die TCM hat das Potential ein gute Alternative zur Matrix Methode zu werden.

## Abstract

At the ATLAS experiment, the accurate determination of the jet energy scale (JES) and its uncertainty is crucial for many physics measurements. The jet pseudorapidity intercalibration is an important in-situ measurement to validate the JES correction and to estimate its uncertainty by balancing transverse momenta of a dijet system.

This thesis presents a new way of selecting appropriate dijet events. The standard methods require a fully efficient trigger for a given transverse momentum bin and hence lose statistics due to high prescale factors during data taking. The Trigger Combination Method (TCM) combines many different jet triggers, if the set of all triggers is fully efficient, to allow an optimized usage of the available statistics. This event selection method has been applied to the Classical Method of the jet pseudorapidity intercalibration. The obtained calorimeter responses have been compared with results from simulation as well as results from the standard methods. Both comparisons show overall a good agreement. Furthermore, systematical studies showed only small systematical errors for the central region, but larger errors in the forward region. This error is mostly due to variations in additional soft radiation and can most likely be reduced by further studies, so that the TCM provides a good alternative to the Matrix Method.



---

# Contents

<b>1. Introduction</b>	<b>1</b>
<b>2. Jet Physics</b>	<b>4</b>
2.1. Standard Model . . . . .	4
2.2. Dijet Production . . . . .	7
2.3. New Physics Searches with Jets . . . . .	12
<b>3. Large Hadron Collider and ATLAS Experiment</b>	<b>15</b>
3.1. Large Hadron Collider . . . . .	15
3.2. ATLAS Detector . . . . .	18
3.3. ATLAS Trigger System . . . . .	32
<b>4. Jet Reconstruction and Calibration in ATLAS</b>	<b>39</b>
4.1. Jet Reconstruction . . . . .	39
4.2. Jet Energy Calibration . . . . .	42
<b>5. In-situ Jet Calibration</b>	<b>49</b>
5.1. Jet Energy Scale Uncertainty . . . . .	49
5.2. Standard Methods for Jet Pseudorapidity Intercalibration . . . . .	52
5.3. Trigger Combination Method . . . . .	58
<b>6. Jet Pseudorapidity Intercalibration with 2011 Data</b>	<b>61</b>
6.1. Dijet Selection . . . . .	61
6.2. Calorimeter Responses . . . . .	70
6.3. Systematical Uncertainty . . . . .	73
<b>7. Conclusions</b>	<b>77</b>
<b>A. Jet Pseudorapidity Intercalibration using 2010 Data</b>	<b>78</b>
<b>B. Calorimeter Responses for 2011 using AntiKt6</b>	<b>82</b>
<b>C. Jet Pseudorapidity Intercalibration using 2012 Data</b>	<b>85</b>
<b>Bibliography</b>	<b>92</b>

# Introduction

NOT ONLY IS THE UNIVERSE STRANGER THAN WE IMAGINE,  
IT IS STRANGER THAN WE CAN IMAGINE.  
*Sir Arthur Eddington (1882-1944)*

The quote from Sir Arthur Eddington reflects our current state of knowledge of our universe also a century later. The curiosity of physicists led to many new discoveries in Particle Physics within the past century. One of the greatest achievements is the theoretical description of the fundamental particles and the interactions between them in the *Standard Model of Particle Physics*. Several high precision measurements confirmed the correctness of the theory, such as the recent discovery of a new boson with a mass of approximately 126 GeV [1, 2], which strongly hints on the existence of the Higgs boson. The Higgs mechanism and the resulting Higgs boson could explain the origin of the fermion masses and the masses of the  $W$ - and  $Z$ -bosons. Despite all these successes, unanswered questions remain which can not be explained by the Standard Model: questions about the difference in magnitudes of the gravitational force compared to the other fundamental forces, about the origin of Dark Matter and Dark Energy, or whether we live in a world with more than the known four dimensions. Physicists do not know exactly how our universe works, but they are trying to develop new theories which can explain the observed phenomena. Whether the theories can be validated in experiments, or whether the universe is even stranger than that, as Sir Arthur Eddington stated, is what the physicists are attempting to answer with data from the *Large Hadron Collider* at CERN near by Geneva at the Swiss-French border. It is the worlds largest particle collider, colliding protons at a center-of-mass energy  $\sqrt{s} = 14$  TeV.

One of the unanswered questions is the *hierarchy problem* which addresses the difference in magnitudes between gravity and the other three fundamental forces. In the Standard Model it appears as the problem of correction terms to the bare Higgs boson mass. Due to higher order corrections and the quadratical dependence on the cut off scale of these corrections, the additional term can grow very large - even larger than the currently most probable mass of 126 GeV. Hence, these large corrections must cancel each other, to get a Higgs boson mass of the expected order.

Another unanswered question is, what Dark Matter and Dark Energy are made up. Stars, which are rotating around the center of a galaxy and have a large distance from this center, have a higher rotation velocity than expected. This can be explained by additional non-visible matter in the galaxies. Further hints on Dark Matter arise from the gravitational lens effect, when light is distorted by massive objects. Nevertheless, Dark Matter has not yet been detected directly and its composition is still unknown. Dark Energy is used to explain the

expansion of the universe, but its origin and existence could not be verified in experiments so far.

New physics theories, which could provide answers to some of these remaining questions include *supersymmetrical* theories or theories with extra-dimensions. Supersymmetric theories propose new particles, related to the known SM particles via a supersymmetric transformation between fermions and bosons. Such particles decay in so called *cascades* into other supersymmetric and Standard Model particles. In some extra dimension theories, only gravity can interact in the additional dimensions and hence, they are hard to detect for scientists. In case of compactified extra spacial dimensions, the unification of all forces might be possible at LHC energies and allow the production of microscopic black-holes. Those would have very distinct signatures in the detector, since they immediately decay democratically and sphere-symmetrically via the *Hawking radiation* into Standard Model particles.

Many Standard Model decays and new physics signals include quarks and gluons in their final states. Due to color *confinement*, they cannot be detected as single particles in the detector but rather they will hadronize and form jets. The energy depositions of the particles in the calorimeter is measured at the electromagnetic scale, since it is easy to calibrate the detector using electron test beams at a known energy. Hadrons lose additional energy in inelastic interactions with the calorimeter material which is not measured by the calorimeter. As a consequence of the non-compensating nature of the ATLAS<sup>1</sup> calorimeters, the calorimeter response to hadrons is lower than for electromagnetic particles such as electrons or photons. To compensate the energy loss, as well as losses in passive material before the calorimeters or crack regions of the detector, jets need a special calibration, the *jet energy scale* correction. The calibration constants are determined from simulation by comparing the measured calorimeter jets to matched truth jets from simulation. To validate the simulation based calibration and to estimate its uncertainty several *in-situ* measurements, utilizing collision data, are performed. The physics processes utilized for these measurements are balancing the transverse momenta of a  $Z$ -boson or a photon ( $\gamma$ ) to the transverse momentum of a jet, or balancing dijet events. The jet pseudorapidity intercalibration, is such an in-situ measurement balancing the momenta of the jets in dijet events to estimate the uncertainty on the jet energy scale correction.

At ATLAS, currently two different methods are used to perform the jet pseudorapidity intercalibration: the Classical Method and the Matrix Method [3, 4]. This thesis presents the Trigger Combination Method, a new method to select appropriate dijet events by combining many jet triggers instead of using only one fully efficient trigger. This Method is then applied to the Classical Method of the jet pseudorapidity intercalibration. The obtained calorimeter responses are compared to results from simulation and to official ATLAS results. The thesis is organized as followed: the second Chapter gives an overview of the Standard Model of Particle Physics with a particular emphasize on jets, their production as well as interesting physics processes with jets. Chapter 3 describes the Large Hadron Collider and the ATLAS detector with all its components and the trigger system. In Chapter 4, the jet reconstruction and calibration at ATLAS is described, followed by Chapter 5 where an overview of the jet energy scale uncertainty determination is given, as well as detailed description of the standard

---

<sup>1</sup>A Toroidal LHC ApparatuS.

---

methods for the jet pseudorapidity intercalibration and especially the Trigger Combination Method to select appropriate dijet events. In the sixth Chapter, the jet pseudorapidity intercalibration using 2011 data collected at ATLAS, is presented and the results compared to simulation and official ATLAS results. A summary of the thesis and its conclusions are given in Chapter 7.

# Jet Physics

This Chapter provides a short overview of the Standard Model and points out its strengths and weaknesses. This is followed by a discussion of dijet production at hadron colliders, as the dominating process at LHC. At the end of this Chapter, some Standard Model physics signatures as well as new physics signatures with jets are presented.

## 2.1. Standard Model

The Standard Model of Particle Physics is currently the best description of the known elementary particles and their interactions. It is a relativistic quantum field theory<sup>1</sup> and includes three of the four fundamental forces: the electromagnetic force, the weak force and the strong force. The theory characterizing the electromagnetic force is called *Quantum Electrodynamics* (QED). In 1967, Glashow, Weinberg and Salam [5, 6, 7] unified the electromagnetic and weak forces in one force: the *electroweak force*. The strong interaction is described by *Quantum Chromodynamics* (QCD) and is responsible for the interactions between quarks and gluons. Gravity is the fourth fundamental force but not a part of the SM. It is described by the general theory of relativity developed by Einstein. The Standard Model contains twelve elementary fermions, four gauge bosons mediating the forces and recent observations strongly hint that the Higgs boson is also part of the Standard Model, assigning masses to the fermions and some of the gauge bosons. The matter particles are grouped into three generations, each generation containing a quark and a lepton doublet. Particles of the same generation have similar physical behavior and the masses of particles increases as one moves higher in generation. In Table 2.1, the classification is shown.

There are six *quarks* with different flavors: up (u), down (d), charm (c), strange (s), top (t) and bottom (b). Quarks carry electrical charge, either  $+2/3$  or  $-1/3$  allowing electromagnetic interactions. Additional to the electric charge, quarks carry weak isospin and color charge. The weak isospin couples to the weak force whereas the strong force couples to color charge. This gives quarks the possibility to interact via all three fundamental forces included in the SM. The quark flavor is conserved for electromagnetic and strong interactions, but in weak interactions it can be changed to a different quark flavor. The *Cabibbo-Kobayashi-Maskawa* (CKM) Matrix [8, 9] contains information about the probabilities of the flavor changing decays.

---

<sup>1</sup>In a field theory, forces are described as interactions with an ambient field. Excitations of this field produce matter particles.

## 2.1. Standard Model

fermion	generation			el. charge	color charge	interaction
	I	I	III			
quarks	u	c	t	+2/3	yes	el.-mag., weak, strong
	d	s	b	-1/3	yes	el.-mag., weak, strong
leptons	e	$\mu$	$\tau$	-1	no	el.-mag., weak
	$\nu_e$	$\nu_\mu$	$\nu_\tau$	0	no	weak

**Table 2.1.:** The fermionic part of the Standard Model with quarks and leptons sorted in three generations. Furthermore, the electrical and color charge, as well as the possible types of interactions are given.

boson	spin	interaction	mass [GeV]	range	relative strength
$W^\pm$	1	weak	80	$10^{-3}$ fm	$10^{-13}$
$Z^0$	1		91		
$\gamma$	1	el.-mag.	massless	$\infty$	$10^{-2}$
g	1	strong	massless	1 fm	1
H	0	couples to mass	126	-	-

**Table 2.2.:** The bosonic part of the Standard Model, including the Higgs boson. The vector gauge bosons are given together with their type of interaction, mass, range and relative strength with respect to the strong force.

In addition, there are six *leptons*: electron ( $e^-$ ), muon ( $\mu^-$ ) and tau ( $\tau^-$ ) with their corresponding neutrinos: ( $\nu_e$ ), ( $\nu_\mu$ ) and ( $\nu_\tau$ ). The first three leptons carry electromagnetic charge as well as weak isospin and hence they interact electromagnetically and/or weakly with other SM particles. On the contrary, neutrinos can only interact via the weak force, since they only carry weak isospin. For each lepton generation there exists a quantum number, the *lepton family number*, which would be a conserved quantity in all types of scatterings and decays, if neutrinos were massless. In 1957 Bruno Pontecorvo [10] predicted the existence of neutrino oscillations, where neutrinos of one flavor can convert to neutrinos of a different flavor, with a non zero probability given that they have a non zero mass. Neutrinos were believed to be massless for a long time, however, in experiments neutrino oscillations were observed and hence, they must have a small, non zero mass. Up to now, it was not possible to measure neutrino masses directly, but only to set upper mass limits. From experiments it is known, they the must have masses smaller than  $m_\nu < 2$  eV [11].

The interactions between the fermions is described by a gauge theory, with an  $U(1) \times SU(2)$  symmetry representing the electro weak sector and a  $SU(3)$  symmetry representing the strong section. The bosonic content of the SM is listed in Table 2.2. Bosons have an integer spin and obey Bose-Einstein statistics. The mediator of the electromagnetic force, called photon, has spin 1 and is massless. Since the photon is massless, the range of the electromagnetic force is infinite. The mediators of the strong force are the eight gluons, having spin 1 and

carrying color charge. Like photons, they are massless, but contrary to the electromagnetic force the range of the strong force is not infinite. Gluons, unlike photons, have the possibility to couple to themselves due to the fact that gluons also carry color charge. As a consequence of this gluon self-coupling, the range of the strong interaction is only a few femtometer. Strong interaction is also responsible for binding nucleons in an atomic nucleus. Here, an effective theory describes the interaction, where pions are used to mediate the strong force between the nucleons. With a pion mass of  $m_\pi \approx 140 \text{ MeV}$ , the range  $d$  of this effective theory is  $d \approx 1 \text{ fm}$ , the range of the strong interaction. Furthermore, strong interaction binds the quarks to color neutral mesons ( $q\bar{q}$ ) or baryons ( $qqq$  or  $\bar{q}\bar{q}\bar{q}$ ). When trying to separate two quarks, an interesting feature of the strong interaction, the so called color *confinement*, prevents the separation. With increasing distance between two quarks the magnitude of the strong force between them increases as well. The force becomes so strong that it is not possible to separate the two quarks, but instead a new quark-antiquark pair is produced. Opposite, for very short distances, the strong interaction becomes weaker and the quarks behave almost like free particles. This is called *asymptotic freedom*.

The Z- and  $W^\pm$ -bosons, with spin 1, are the mediators of the weak interaction. The electrically neutral Z-boson has a mass of  $(91.1876 \pm 0.0021) \text{ GeV}$  and is the heaviest known gauge boson. The  $W^\pm$ -bosons are a little less heavy with  $(80.385 \pm 0.015) \text{ GeV}$  and carry electrical charge [11]. Since the mediators of the weak interaction are quite heavy, the range  $d$  of the weak interaction is very short with  $d = 10^{-18} \text{ m}$ . The masses of the Z- and  $W^\pm$ -bosons can be assigned by spontaneous symmetry breaking of the Higgs field in the electroweak sector of the Standard Model. In 1964, the theory of the Higgs mechanism was developed in parallel by Higgs [12], Englert and Brout [13] as well as Guralnik, Hagen and Kibble [14] at the same time. In the Higgs mechanism, an additional SU(2) doublet, with two complex components, is added to the Standard Model [15]

$$\Phi = \begin{pmatrix} \chi_1 + i\chi_2 \\ \chi_0 + i\chi_3 \end{pmatrix} \quad (2.1)$$

with an additional potential

$$V(\Phi) = -\mu^2 \Phi^\dagger \Phi + \lambda (\Phi^\dagger \Phi)^2. \quad (2.2)$$

Minimizing this potential leads to two solutions: a trivial and a non-trivial

$$\langle \Phi^\dagger \Phi \rangle_0 = \begin{cases} 0 & \text{for } \mu^2 > 0 \\ \frac{\mu^2}{2\lambda} & \text{for } \mu^2 < 0. \end{cases} \quad (2.3)$$

where only the non-trivial case is interesting. From the infinite number of choices, one can choose  $\langle \chi_{1,2,3} \rangle_0 = 0$ , and  $\langle \chi_0 \rangle_0 = \frac{\mu^2}{2\lambda} = v$ , with  $v$  being the vacuum expectation value, and the symmetry becomes spontaneously broken. The second component of the original doublet can be written as  $\chi_0 = \frac{1}{\sqrt{2}}(H_0 + v)$  with  $\langle H_0 \rangle_0 = 0$ . The  $H_0$  represents the physical *Higgs field*. Inserting the vacuum expectation value into the Lagrangian, describing the interaction between fermions and the Higgs field, assigns masses to the previously massless fermions

$$m_j = \frac{v}{\sqrt{2}} f_j \quad (2.4)$$

with  $j \in \{u, d, e\}$  and  $f_j$  the respective coupling constants. When inserting the vacuum expectation value into the Lagrangian which describes the interaction between the Higgs field

and the gauge bosons something similar happens. The generator of the SU(2) is the vector  $\vec{W}$  with three entries  $W_{1,2,3}$  and the generator of the U(1) is the scalar boson  $B$ . The first two components of the  $\vec{W}$  can be written as

$$W^\pm = \frac{1}{\sqrt{2}}(W_1 \mp iW_2) \quad (2.5)$$

and the third component  $W_3$  is neutral. After expanding the Lagrangian, which describes the interaction between the gauge bosons and the Higgs field, the  $W^\pm$ -bosons get masses of  $M_{W^\pm} = \frac{1}{2}vg_2$ . The third component  $W_3$  and the scalar boson  $B$  get mixed, yielding into two new particles the massless photon  $\gamma$  and the massive  $Z$ -boson. Its mass is  $M_Z = \frac{1}{2}v\sqrt{g_1^2 + g_2^2}$ , with  $g_1$  and  $g_2$  the coupling of the U(1) and SU(2), respectively. The Higgs field produces an own particle, the Higgs boson with a mass of  $M_{H_0} = 2v^2\lambda$ . The vacuum expectation value  $v$  can not be determined from theory but must be measured in experiments. Latest research results from ATLAS and CMS<sup>2</sup> at the *Large Hadron Collider* (LHC) have observed a previously unknown boson with a mass of  $M_{boson} \approx 126.0$  GeV. The local significance<sup>3</sup> of the excess observed by ATLAS is  $5.9\sigma$  [1]. So far, the new boson is consistent with a SM Higgs boson, but whether this new boson is the SM Higgs or a different particle, has to be verified in further experiments. CMS sees a similar excess at the same mass with comparable significance [2].

## 2.2. Dijet Production

As described in the previous section, due to the color confinement, quarks can not exist as single, free particles. This is also the reason why it is not possible to measure single quarks in a detector. Instead, the process of hadronization happens, where quarks and gluons combine with quarks-antiquark pairs, emerging from vacuum fluctuations, to hadrons and then decay further. These particles are the product of the hadronization and they form a collinear bunch of particles, called a jet. Jets are very important for high-energy physics, since they appear in many physics signals: not only in new physics signals but also in Standard Model processes. At hadron colliders, jet production is one of the most frequent processes. In Figure 2.1 several cross sections are shown for the two hadron colliders Tevatron<sup>4</sup> and LHC. Jet production cross sections for different physics processes, such as the production of b-jets or jets with energies above 100 GeV, are dominant processes at LHC. Hence, jet production and especially dijet production will be discussed in more detail in this Section.

---

<sup>2</sup>Compact Muon Solenoid.

<sup>3</sup>Significance is defined as  $\frac{S}{\sqrt{S+B}}$  where  $S$  is the number of signal events and  $B$  is the number of background events. It is a measure of the probability, that the observed data is not the null hypothesis.

<sup>4</sup>A proton-antiproton collider with a center-of-mass energy of  $\sqrt{s} = 2$  TeV at Fermilab in Illinois, USA. It was the largest hadron collider until LHC started operating. It was shut down in September 2011.

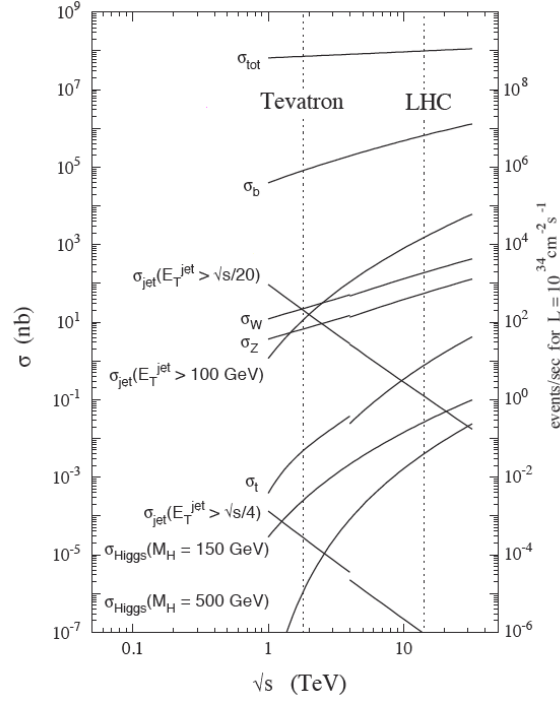


**Figure 2.1.:** Production cross sections and rates at LHC desing luminosity. Various physics processes as a function of the center-of-mass energy at Tevatron and LHC are shown. Jet production is dominant over several orders of magnitude [16].

## Types of Interactions

At the LHC, a proton-proton collider, the main interactions occur between the constituents of the proton: the quarks and gluons, also called partons. Quarks and gluons interact via the strong force and when two partons are scattered, there are two different ways of interaction: the hard and soft scattering.

An interaction is called a *hard interaction*, when  $Q^2 \gg \Lambda$ , which means the momentum transfer between the partons is much larger than the energy scale  $\Lambda$ . In this case, the coupling constant<sup>5</sup>  $\alpha_s(Q^2) \ll 1$  is small and perturbation theory is applicable and gives in leading order

$$\alpha_s(Q^2) = \frac{12 \pi}{(11N_c - 2N_f) \ln \frac{Q^2}{\Lambda}} \quad (2.6)$$

with  $N_c$  the number of different color charges ( $N_c = 3$ ),  $N_f$  the number of participating quark flavors and  $\Lambda$  the QCD scale.

*Soft interactions* are interactions with low momentum transfers  $Q^2 \ll \Lambda$ . Here, the strong coupling constant becomes of the size of unity,  $\alpha_s(Q^2) \approx 1$ , and in this case perturbation theory can not be used anymore to describe the occurring phenomena. The QCD scale  $\Lambda$  defines the energy scale when the strong coupling constant reaches approximately unity at  $\lambda \approx 217 \text{ MeV}$ .

<sup>5</sup>In quantum field theories this coupling 'constant' is an effective constant and dependent on the momentum transfer  $Q^2$ . Hence it is also called *running coupling*.

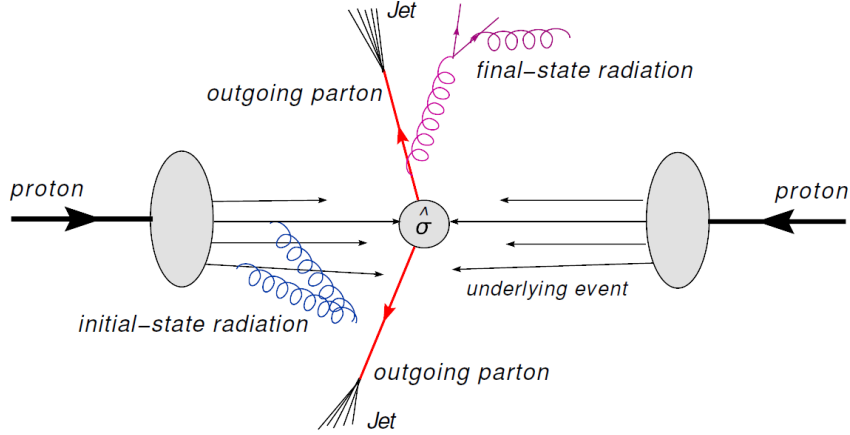


**Figure 2.2.:** Dijet production in the channel  $p_1 + p_2 \rightarrow jet_1 + jet_2 + X$ . Additional to the hard interaction, soft interactions like ISR, FSR and underlying events are shown.  $X$  denotes everything else produced in the interaction, except the two outgoing jets [17].

The  $Q^2$  dependence corresponds to a dependence on the distance between the two partons. Low momentum transfers  $Q^2$  correspond to a larger distance between the participating partons, resulting in a stronger coupling. For large distances, the coupling becomes so strong that it is impossible to separate single quarks from a hadron, the previously mentioned *confinement*. For higher momentum transfers  $Q^2$ , the distance decreases between the participating partons and the coupling strength gets weaker. The limit  $Q^2 \rightarrow \infty$  is called *asymptotic freedom*, since the quarks can behave like free particles.

At LHC, the hard interactions are more interesting than soft interaction processes since new physics processes are expected to occur at high energies, with small cross sections. Most of the hard processes are accompanied by several soft interactions. Soft radiation originates from **Initial-State Radiation** (ISR) where incoming partons radiate gluons before the hard scattering. Likewise the **Final-State Radiation** (FSR), where outgoing partons radiate gluons after the hard scattering. Soft interactions can also occur from so called **Underlying Events** (UE). These are interactions between partons which are not involved in the hard scattering process itself, e.g. *spectator quarks*. Furthermore, interactions with the beam remnants (*multiple scattering*) can also lead to soft particle production. It can also happen that protons, from the same bunch but not participating in the hard interaction, interact via soft scattering with each other. This effect is called *pileup* and occurs mainly at low energies. It is a big issue at LHC, especially at high luminosities. In Figure 2.2 a proton-proton collision is shown with two jets in the final state together with ISR, FSR as well as underlying events. It is crucial to understand all the appearing processes to ensure precise measurements of the outgoing, hard scattered partons.

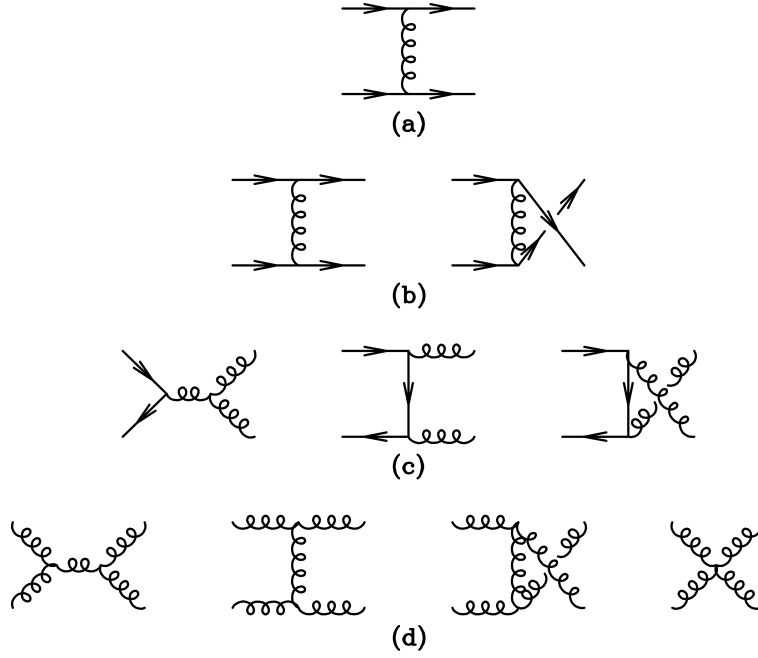


**Figure 2.3.:** Feynman diagrams of leading order dijet production. Quarks and anti-quarks are represented by straight lines, gluons by curly [18].

## Production

Hard scattered interactions between partons are less frequent than soft interactions, but also the more interesting processes. Since this thesis utilizes dijets for the analysis, the production of dijet events for a hadron collider, such as the LHC, is discussed. The inclusive scattering process has the topology:

$$p_1 + p_2 \rightarrow X \quad (2.7)$$

with  $p_{1,2}$  two partons and  $X$  any possible final state. For dijets, a  $2 \rightarrow 2$  topology is desired:

$$p_1 + p_2 \rightarrow x_1 + x_2. \quad (2.8)$$

with  $p_{1,2}$  being partons of the initial protons and  $x_{1,2}$  two possible final partons states. When two incoming partons are hard scattered they can produce two new outgoing partons with high transverse momentum. These outgoing partons are detected as jets. Due to momentum conservation, the two scattered partons have the same but opposite momenta in the center-of-mass frame. In the azimuthal plane the two jets are back-to-back and balanced in the momenta. This feature is also used for the jet pseudorapidity intercalibration, described in Chapter 5. In Figure 2.3 the Feynman diagrams for leading order dijet production are shown. Gluons are represented by the curly lines and straight lines represent quarks or anti-quarks. The first and second diagram are not the same since the first denotes  $qq' \rightarrow qq'$  scattering with two different quark flavors, whereas the second represents  $qq \rightarrow qq$  scattering with the same flavors. From these and higher order diagrams the inclusive cross section can be derived. For two incoming partons  $i, j$  with momentum fractions<sup>6</sup>  $x_i, x_j$  and two outgoing partons

<sup>6</sup>Is also called Bjorken variable. It gives the momentum fraction of the parton.  $x = 1$  for an elastic scattering, and  $0 < x < 1$  for inelastic scattering.

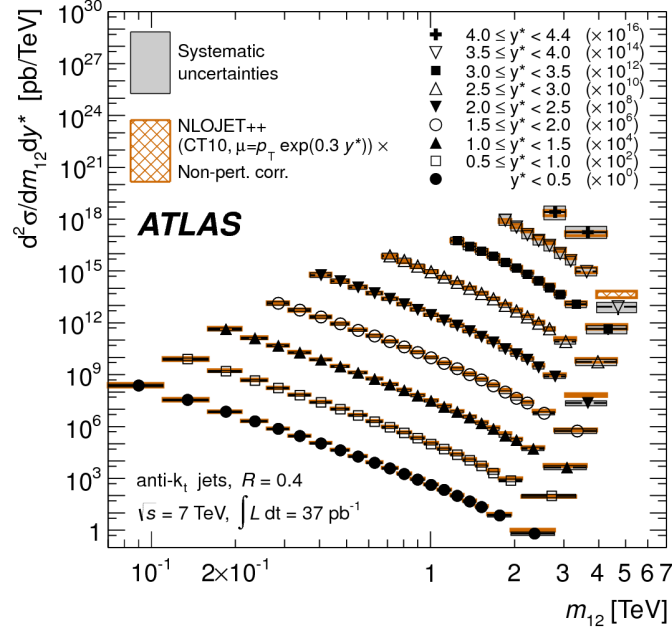


**Figure 2.4.:** The double differential dijet cross section at ATLAS in 2011 [19]. The cross sections are shown as a function of the dijet mass and for several  $\Delta y^*$ -bins.

$k, l$  with rapidities<sup>7</sup> in the laboratory frame  $y_3, y_4$  the inclusive, unpolarized dijet cross section is given by [18]:

$$\frac{d^3\sigma}{dy_3 dy_4 d(p_T^2)} = \frac{1}{16\pi s^2} \sum_{i,j,k,l} \frac{f_i(x_1, \mu^2)}{x_1} \frac{f_j(x_2, \mu^2)}{x_2} \overline{\sum} |\mathcal{M}(ij \rightarrow kl)|^2 \frac{1}{1 + \delta_{kl}}. \quad (2.9)$$

The indices  $i, j, k, l \in \{q, \bar{q}, g\}$  can represent any possible parton, the function  $f_i(x, \mu^2)$  denotes the parton density function for a parton of type  $i$ ,  $\mu$  the momentum scale at which the scattering takes place and  $s$  is the center of mass energy. The  $|\mathcal{M}(ij \rightarrow kl)|^2$  gives the invariant matrix element squared for the transition from initial states  $i, j$  to final states  $k, l$ . Furthermore, it has to be taken into account that incoming particles are unpolarized whereas the polarization of the outgoing particles can not be measured<sup>8</sup>. Hence, for initial state partons the averages of the color and spin state indices have to be taken, whereas for the final state partons the sum over these indices must be used. This is represented by the  $\overline{\sum}$  symbol. The  $\delta_{kl}$  is statistically essential to account for identical final state partons. In Figure 2.4, double differential dijet cross sections as a function of the dijet mass in ATLAS are shown. The other colored lines represent theoretical predictions at next-to-leading-order (NLO) using the simulation sample NLOJET++ with non-perturbative corrections. Several cross sections are shown for different  $\delta y^*$  bins, the difference in rapidity between the first two leading jets, multiplied by a constant factor, for convenience. The cross sections extend over nine orders of magnitudes and the mass range extends over two orders of magnitudes. Over the entire range data and predictions from simulation are in good agreement.

<sup>7</sup>Rapidity  $y$  is defined as  $y = \frac{1}{2} \ln \left( \frac{E+p_z}{E-p_z} \right)$ , see Chapter 3.

<sup>8</sup>This is why it is an unpolarized cross section.

## 2.3. New Physics Searches with Jets

Even though the Standard Model gives very good predictions for many processes, there are still some unanswered questions which can not be explained by the Standard Model. One of the problems of the Standard Model is the *hierarchy problem* which addresses the seemingly so unnatural high difference of the magnitudes between weak force and gravity. In the Standard Model this is reflected by the difference in the Higgs boson mass scale and the Planck scale<sup>9</sup>  $\mathcal{O}(10^{19}$  GeV). The Higgs mass is composed of a bare mass term and a correction term:

$$m_H = m_{bare} + \Delta m_H(\Lambda^2). \quad (2.10)$$

The correction term arises from radiative corrections and higher order loop terms which are quadratically dependent on the cut off scale  $\Lambda$ . The Planck scale would provide a reasonable cut off scale, but the bare mass of the Higgs is expected, from tree level calculations and recent experimental results from LHC, to be at the electroweak scale of  $\mathcal{O}(100$  GeV). In this case the correction term dominates the Higgs mass. In the SM it can only be solved by a fine-tuning, a smart renormalization, which leads to cancellations of major contributions of the correction term.

Further hints for the fact that there is more than the Standard Model are given by Dark Matter. Dark Matter, as the name suggests, neither absorbs nor emits light and hence it is not possible to directly observe it. Nevertheless, its gravitational effects on other astronomic objects strongly hint on its existence. The main contribution to the content of the universe arises from Dark Energy with 72%. Dark Matter contributes with 23% and only the remaining 5% are due to known matter. The Standard Model does not provide a Dark Matter candidate. Another approach for new physics theories utilizes the unification of the forces. Since the successful unification of the electromagnetic and weak force to the electroweak section of the SM, theorists try to find a *Grand Unifying Theory* (GUT) to unify the electroweak force with the strong force. Within the Standard Model such a unification is not possible, not even at very large energy scales.

*SUper SYmmetry* (SUSY) models are new physics theories which could solve many of the open questions. They introduce a new symmetry between fermions and bosons and predict additional particles. By a supersymmetrical transformation, which transforms bosonic (fermionic) SM particles into fermionic (bosonic) SUSY particles, superpartners are related to each other. This basic symmetry provides an elegant solution to the hierarchy problem. All higher order loop corrections would appear for SM as well as for SUSY particles and under the assumption that the SUSY particles are not much heavier than the Standard Model particles, most of the divergent mass terms would be cancelled in a natural way. The most prominent SUSY model, the *Minimal Supersymmetric Standard Model* (MSSM) was proposed in 1981 by Howard Georgi and Savas Dimopoulos [20]. This is a minimal extension to the Standard Model where only all known elementary matter particles and force carriers get superpartners. The superpartners of the SM quarks and leptons are called squarks and sleptons, respectively. Standard Model bosons also have superpartners, for example the gluinos are the superpartners of the gluons and photinos are the superpartners of the photon.

<sup>9</sup>At this scale gravity becomes of the same strength as the other forces, leading to a breakdown of the description of the interaction between elementary particles since quantum gravity effects appear.

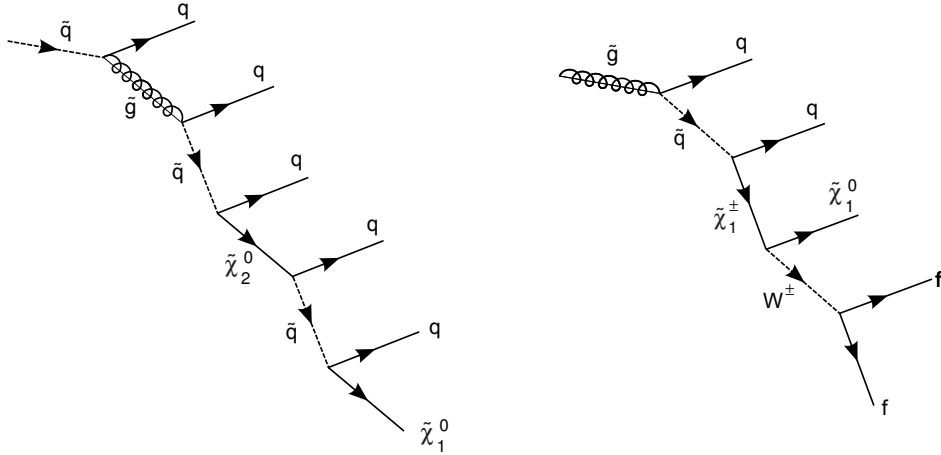


**Figure 2.5.:** Exemplary cascade decay of a squark (left) into five quarks plus a neutralino and a gluino (right) into two quarks, a fermion pair and a neutralino. The neutralinos escape the detector without giving a signal and hence, appear as missing transverse energy.

At the LHC, supersymmetrical particles would be mainly produced via hard scattering of partons:

$$\begin{aligned} gg &\longrightarrow \tilde{g}\tilde{g} \\ gp &\longrightarrow \tilde{g}\tilde{q} \\ qq &\longrightarrow \tilde{q}\tilde{q} \end{aligned}$$

where  $g$  denotes gluons,  $q$  denotes quarks (or anti-quarks) of an arbitrary flavor and  $\tilde{g}, \tilde{q}$  denote gluinos and squarks respectively. At the LHC, quarks and gluinos can be produced with masses up to approximately 1 TeV. For the production of heavier squarks and gluinos the center-of-mass energy of LHC is not sufficient. SUSY particles decay via so called *cascades* into SUSY and SM particles, mainly quarks but also in  $W$  and  $Z$  bosons or fermions. Hence, signal channels include leptons and jets. In general quantum numbers, such as the *lepton number*<sup>10</sup>  $L$  or the *baryon number*<sup>11</sup>  $B$  are not conserved. In particular, a decay of the proton would be allowed. However, there is strong experimental evidence that the proton is stable, so one has to restrict the proton decay otherwise. This is done by requiring the conservation<sup>12</sup> of a new quantum number, the *R-parity*. It is defined

$$R = (-1)^{3(B-L)+2S} \quad (2.11)$$

with  $L$  the lepton number,  $B$  the baryon number and  $S$  the spin. For SM particles the R-parity is always  $R = +1$  and for SUSY particles  $R = -1$ . When R-parity is conserved, this implies the existence of a stable *Lightest Supersymmetrical Particle* (LSP) since the number of produced and/or decayed SUSY particles must be even. The LSP is a light, neutral particle

<sup>10</sup>The lepton number  $L$  is defined as  $L = n_l - n_{\bar{l}}$ , with  $n_l$  the number of leptons and  $n_{\bar{l}}$  the number of antileptons. For leptons it is +1 for antileptons -1.

<sup>11</sup>The baryon number  $B$  is defined as  $B = \frac{1}{3}(n_q - n_{\bar{q}})$ , with  $n_q$  the number of quarks and  $n_{\bar{q}}$  the number of antiquarks. For baryons it is +1 and for antibaryons -1. Mesons have baryon number of 0.

<sup>12</sup>Not all SUSY theories are R-parity conserving.

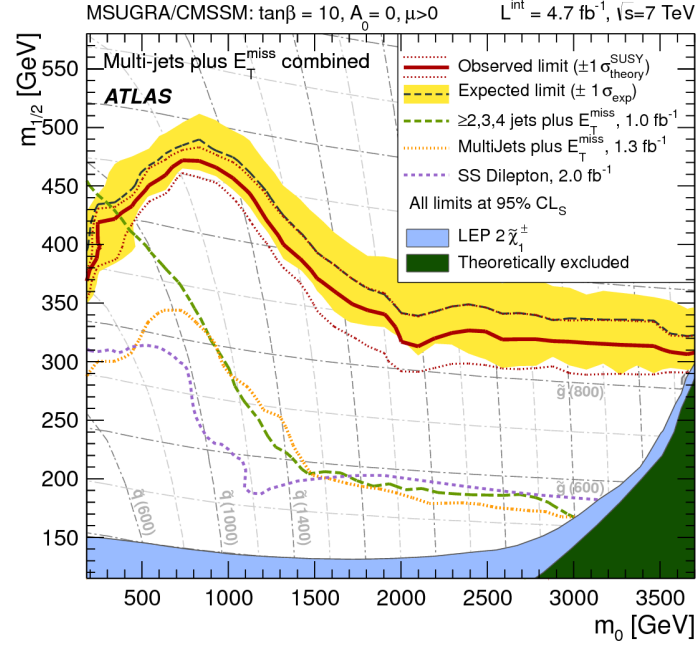


**Figure 2.6.:** Here, the plane of the mass of the first two generation squark masses ( $m_{1/2}$ ) and the sgluino ( $m_0$ ) mass is shown. The curves for the expected (black, dashed line with yellow band) and observed (red line and red dashed lines) exclusions are shown, with a  $1\sigma$  statistical uncertainty band. Different signal channels, which are contributing to the observed limit are also shown [21].

appearing in large amounts and hence it is a perfect Dark Matter candidate. In the MSSM, the neutralino  $\chi^0$  is the LSP candidate.

In a detector such an LSP would escape the detector without leaving a signal and hence is only recognizable as missing transverse energy  $E_T^{miss}$ . The final signal channels for SUSY searches at ATLAS are

$$x \text{ leptons} + y \text{ jets} + E_T^{miss} \quad (2.12)$$

with  $x, y \in \mathbb{N}$ . In Figure 2.5, two exemplary decay cascades for a squark (left) and a gluino (right) are shown. The signal in the detector for the squark decay would be five jets plus missing energy and no leptons. For the gluino decay the signal would be two jets plus one lepton plus missing energy or four jets plus missing energy, dependent on the decay of the  $W^\pm$  boson. Decays with the same final states are also produced via SM processes and are not distinguishable from SUSY decays. The contributions from SM processes to the cross section has to be known very precisely, since new physics signals would enhance the measured signal. In SUSY searches, typical SM background events arise from  $t\bar{t}$ , single top,  $W + jets$ ,  $Z + jets$  or QCD-multijets events. So far no SUSY signals have been found. In Figure 2.6, 95% exclusion limits on SUSY (mSUGRA/CMSSM<sup>13</sup>) are shown. The final observed limit is composed of different signal channels: at least 2, 3 or 4 jets plus missing transverse energy, multijets plus missing transverse energy and same sign dilepton searches. The black line with the yellow band denotes the expected limit with a  $1\sigma$  band. As it can be seen from the Figure, signal channels including jets are essential for SUSY searches.

<sup>13</sup>minimal **S**Uper **G**RAvity (mSUGRA). **C**onstrained **M**inimal **S**upersymmetric **S**tandard **M**odel (CMSSM).

# Large Hadron Collider and ATLAS Experiment

In the first part of this Chapter, the setup and layout of the Large Hadron Collider and the ATLAS detector are described. Technical and physics requirements, as well as financial and location issues, set restrictions on the design and layout. In the second part of the Chapter, the trigger system is presented and discussed. For more details about technical aspects of the LHC or the ATLAS detector, reference [22] is recommended.

## 3.1. Large Hadron Collider

The *Large Hadron Collider* (LHC) is the world's largest particle collider. It is hosted in the previous *Large Electron-Positron Collider* (LEP) tunnel at CERN<sup>1</sup> at the French-Swiss border near by Geneva. It is a circular hadron collider, colliding mainly highly relativistic protons but also heavy ions, like lead ions. Protons and heavy ions have the advantage, compared to electrons, that they do not lose as much energy via *bremsstrahlung*<sup>2</sup> and hence circular proton proton colliders can still be built. The circumference is about 27 km and it is located between 50-175 m below ground. The first beams were successfully collided on 10<sup>th</sup> of September 2008, but unfortunately a technical accident a few days later forced the collider to shut down again to repair the damage. On March, 30<sup>th</sup> 2010, the LHC started operating again at a center-of-mass energy of  $\sqrt{s} = 7$  TeV. At the beginning of the year 2012, the energy was increased to  $\sqrt{s} = 8$  TeV, which is still the current center-of-mass energy. In 2013, a shutdown of 20 months is planned to upgrade hardware and software systems at the LHC and the detectors. After these upgrades, it is anticipated to collide particles at the design center-of-mass energy of  $\sqrt{s} = 14$  TeV.

The tunnel contains two separate pipes, one for each beam, evacuated to a pressure of approximately  $10^{-13}$  atm. Beam intersections are only possible at the *Interaction Points* (IP) of the four main experiments ALICE<sup>3</sup>, ATLAS, CMS and LHCb<sup>4</sup>. The particles are not filled continuously into the accelerator but in so called *bunches*, each containing about  $10^{11}$  protons. Each bunch has a length of approximately 7.6 cm and the LHC is designed to have bunches

<sup>1</sup>European Organization for Nuclear Research. The abbreviation CERN arises from the previous French name *Conseil Européen pour la Recherche Nucléaire*.

<sup>2</sup>Accelerated charge radiates bremsstrahlung. The amount of radiation is larger for light particles compared to heavy particles. Hence electrons lose a lot of energy due to bremsstrahlung, compared to protons.

<sup>3</sup>A Large Ion Collider Experiment.

<sup>4</sup>Large Hadron Collider beauty experiment.

every 25 ns, corresponding to a distance between the bunches of 7 m. Currently bunches are filled with halved frequency, every 50 ns. To keep the particles on course, 1232 superconducting dipole magnets with magnetic fields up to 8.33 T and an operating temperature of 1.9 K are used [23]. To focus the beam, 858 superconducting quadrupole magnets are utilized. Each quadrupole focuses the beam either in vertical or horizontal direction, depending on its alignment. Assembling the two possible alignments behind each other one achieves that the beam is focused in both directions. Further sextupole and octupole magnets are used to improve the focusing. To increase the probability of hard interactions, the bunches are squeezed to a diameter of 16  $\mu\text{m}$  before the beam intersections. The beams are accelerated in eight superconducting **R**adio**F**requency (RF) cavities with a frequency of 400 MHz. Furthermore, the RF cavities are used to correct small deviations of spacing between the bunches.

The event rate at the LHC is given by

$$\frac{dN}{dt} = \dot{N} = \mathcal{L}_{\text{inst}} \cdot \sigma \quad (3.1)$$

with  $\mathcal{L}_{\text{inst}}$  the *instantaneous luminosity* and  $\sigma_{\text{event}}$  the cross section for the studied process. The instantaneous luminosity can be calculated as:

$$\mathcal{L}_{\text{inst}} = \frac{n \cdot N_1 \cdot N_2 \cdot f}{A} \quad (3.2)$$

with  $n$  the number of bunches,  $N_{1,2}$  the number of protons in the two colliding bunches,  $f$  the revolution frequency and  $A$  the area of the particle bunches at the interaction point. Integrating the instantaneous luminosity over the time gives the *integrated luminosity*

$$\mathcal{L} = \int \mathcal{L}_{\text{inst}} \cdot dt \quad (3.3)$$

and gives the total number of expected events. In 2012, the peak luminosity of  $6.76 \cdot 10^{33} \text{ cm}^{-2} \text{ s}^{-1}$  [24] was achieved setting a new world record.

The luminosity delivered by LHC to the experiments is exponentially decreasing for each run. It is reasonable to divide each run into small units, so called *luminosity blocks* to determine the integrated luminosity for each single block. The block size should be as small as possible to minimize data loss in case of technical problems with the detector by only excluding the concerning luminosity blocks. Nevertheless, each luminosity block should be large enough to have sufficient amount of data to assure reasonably small statistical uncertainties for the luminosity calculation of each block. Every event has the corresponding luminosity block number stored and events where the detector was operating without issues are listed in the so called *Good Run List* (GRL), which is used for most of the physics analyses.

## Preaccelerating system

The particles run through a system of preaccelerators before entering the LHC, shown in Figure 3.1. Protons and heavy ions are produced at different sources and hence, have different preaccelerators. The protons are produced from a hydrogen source by stripping off the electrons. Then they are first accelerated by the LINAC<sup>5</sup> to an energy of approximately

<sup>5</sup>A linear accelerator.

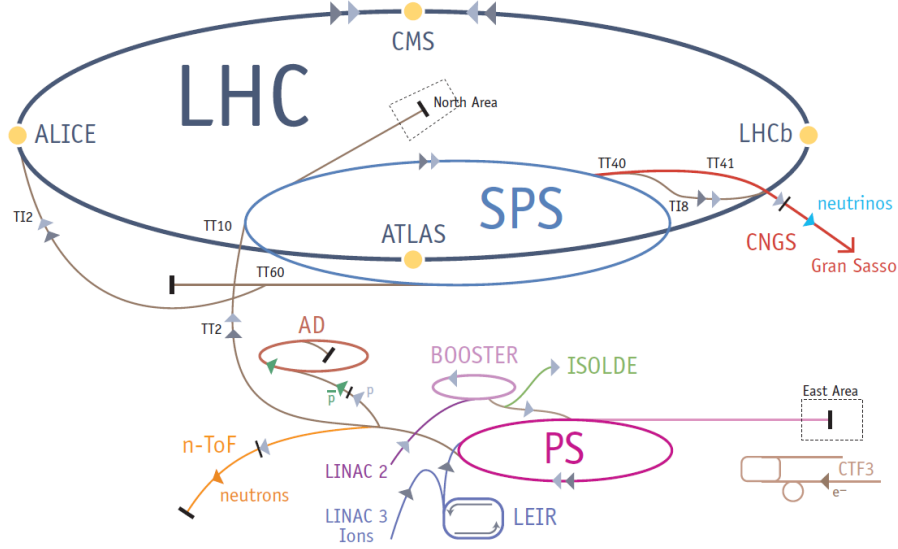


**Figure 3.1.:** Before entering the LHC the particles are going through a system of preaccelerators to be accelerated to an energy of 450 GeV (protons) [25]. Filled in the LHC it takes additional 20 min to accelerate the protons to their final energy of 7 TeV per bunch.

50 MeV and then enter the *Proton Synchrotron Booster* (PSB) to be accelerated to an energy of 1.4 GeV. Afterwards they are filled in the *Proton Synchrotron* (PS), accelerated to an energy of 26 GeV and then in the *Super Proton Synchrotron* (SPS) to an energy of 450 GeV. Finally the particles are filled in the LHC and accelerated to their final energy of several TeV. After entering the LHC, it takes about 20 min to accelerate the proton beams from an energy of 450 GeV to the final design energy of 7 TeV. The heavy ions are first accelerated at LINAC3 and further accelerated at the *Low Energy Ion Ring* (LEIR). Afterwards they are also filled in the PS and follow the same path as protons. Lead ions are designed to have a final energy of 2.76 TeV per nucleon.

## Experiments

There are four main experiments at the LHC: ALICE, ATLAS, CMS and LHCb which are shortly presented here. Besides the four main experiments, there are several smaller experiments such as TOTEM<sup>6</sup>, LHCf<sup>7</sup> or MoEDAL<sup>8</sup>.

ALICE is focused on heavy ion physics. It is a cylindrical detector and has a length of 25 m, a diameter of 16 m and a weight of 10000 t. The heart of the detector is the *Time Projection Chamber* (TPC), a huge gaseous detector which is used for particle identification and tracking of charged particles. It covers the full azimuthal range and a pseudorapidity range of  $|\eta| < 2$ . ALICE was designed to handle the exceptionally high particle multiplicities in lead ion collisions at a center-of-mass energy of  $\sqrt{s} = 5.52$  TeV. At such high densities and temperatures,

<sup>6</sup>TOTAL Elastic and diffractive cross section Measurement.

<sup>7</sup>Large Hadron Collider forward.

<sup>8</sup>MONOpole and EXotics DETector At the LHC.

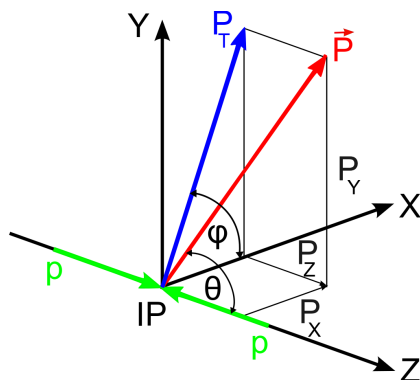


Figure 3.2.: The ATLAS coordinate system.

ALICE aims to detect quark-gluon plasma, a state of matter, when quarks and gluons are deconfined and behave like free particles.

The ATLAS detector is a multipurpose detector, designed for a broad search of new physics signals. It is the largest detector and its volume is dominated by the large, air-cored toroidal magnets. The physics goals of ATLAS and CMS are similar, and hence they are able to validate each other's results. It is described in more detail in the next Section.

The CMS detector is also a multipurpose detector, designed for the search of new physics signals. It is a  $4\pi$  detector, covering full azimuthal range, with a diameter of 16 m, a length of 21 m and a weight of 12500 t. Its calorimeter is made of lead tungsten ( $\text{PbWO}_4$ ) crystals, providing high energy resolution for electrons and photons. It is placed inside a large solenoid magnet, inducing a magnetic field of 4 T allowing a precise muon tracking.

The LHCb detector is a forward spectrometer, the only experiment with an asymmetric design. Its focus is on studies of the matter-antimatter asymmetry in rare b-meson decays. The detector design reflects the specific necessities and is optimized for its purpose. The vertex detector is with a distance of 7 mm the closest detector to the beam line of all experiments. LHCb contains two separate *Ring Imaging Čerenkov Detectors* (RICH) for precise particle identification.

## 3.2. ATLAS Detector

The ATLAS detector is the largest of the four main experiments and a multipurpose detector, designed to search for new physics signals however they might look. To allow such challenging searches, SM processes must be measurable with high accuracy.

Before describing the detector elements, the ATLAS coordinate system and some important variables are introduced. ATLAS uses a right handed coordinate system with the interaction point as its origin, as shown in Figure 3.2. The positive x-axis points from the IP to the center of the LHC and the y-axis from the IP upwards. The z-axis is along the beam line while the x-y plane is perpendicular to the beam line. All transverse variables, such as transverse momentum  $p_t$ , transverse energy  $E_t$  or missing transverse energy  $E_t^{miss}$  are defined as the component of the respective variable in the x-y plane. The detector side at the positive z-axis is called A side, at the negative z-axis is called C side. The azimuthal angle  $\varphi$  is defined

as the angle around the beam axis ranging from 0 to  $2\pi$ . The polar angle  $\theta$  is the angle from the beam line, ranging from 0 to  $\pi$ . Instead of the angle  $\theta$  it is often better to use the *pseudorapidity*, defined as:

$$\eta = -\ln\left(\tan\frac{\theta}{2}\right). \quad (3.4)$$

For particles which are traveling with almost speed of light or when the particle mass can be neglected compared to the energy, the pseudorapidity is becomes the same as the *rapidity*. The rapidity  $y$  is defined as

$$y = \frac{1}{2} \ln\left(\frac{E + p_z}{E - p_z}\right) \quad (3.5)$$

with  $E$  being the energy of the particle and  $p_z$  the component of the momentum along the beam axis. The rapidity difference is invariant under Lorentz boosts and the particle flux is constant in every rapidity interval. Since rapidity and pseudorapidity can be assumed the same for LHC energies, the difference in the pseudorapidity is also approximately invariant under Lorentz boosts. Two equal jets, with one jet being central<sup>9</sup> and the other one more forward<sup>10</sup>, will have different shapes in the  $\varphi$ - $\theta$  plane. The more forward jet will be squeezed, or Lorentz contracted, in  $\eta$ . In the  $\varphi$ - $\eta$  plane the two jets have the same shapes, since they have the same  $\Delta\eta$  values.

The distance  $\Delta R$  between two objects is defined as

$$\Delta R = \sqrt{(\varphi_1 - \varphi_2)^2 + (\eta_1 - \eta_2)^2} = \sqrt{\Delta\varphi^2 + \Delta\eta^2} \quad (3.6)$$

and is often used to isolate objects in the azimuthal-pseudorapidity plane.

The LHC will provide 40 million bunch collisions per second at a design luminosity of  $10^{34} \text{ cm}^{-2}\text{s}^{-1}$ . In each collision up to  $\sim 23$  inelastic interactions can appear, producing up to thousand particles. ATLAS has to detect the interesting decays and take first decisions whether an event is worth to be further analyzed or not within  $2.5 \mu\text{s}$  to allow an optimal usage of the available storage. This decision is taken by many different triggers. The technology of the detector had to be developed over several years to handle all the necessary requirements. Taking technical and physical aspects into account, some of the requirements are:

- Full azimuthal and large pseudorapidity coverage are desired to guarantee correct event reconstruction and allow missing transverse energy measurements. On the other hand space for cables, power supply or cryogenic systems must be provided.
- The detector elements must have high granularity, to manage the high particle multiplicity from pileup, or other inelastic scatterings. The electronics and sensors must be fast to handle the high collision frequency and be radiation-hard to minimize radiation damages or aging of the detector.
- Triggers must have high efficiencies and high background rejection.

<sup>9</sup>When an object is in the central direction, it has small pseudorapidity values.

<sup>10</sup>When an object is in the forward direction, it has large pseudorapidity values.

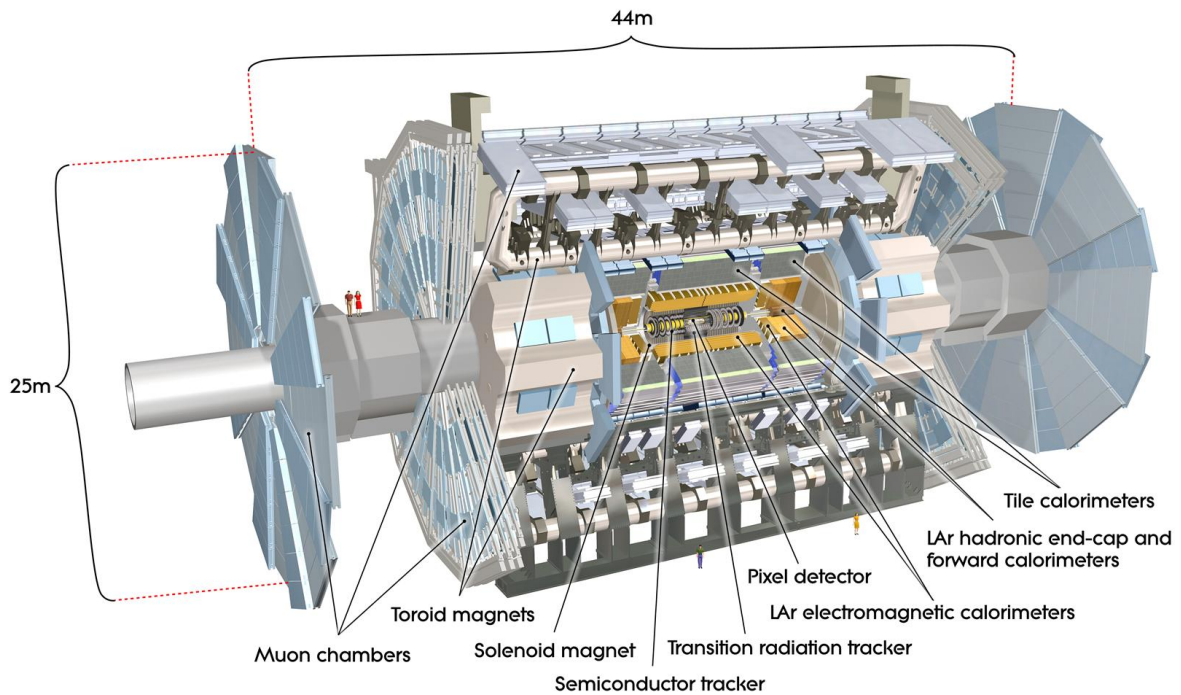


**Figure 3.3.:** The ATLAS detector with its main components. To get a feeling for the size proportions, four humans are also drawn in the picture [22].

- The correct identification of primary and secondary vertices is essential to gain high reconstruction efficiencies and allow  $b$ -tagging<sup>11</sup> of jets or  $\tau$ -tagging<sup>12</sup>.
- Advanced calorimetry technologies are required: electromagnetic calorimeters must have precise electron and photon identification, as well as very good energy measurements for these particles. Additionally, hadronic calorimeters must provide accurate energy measurements of hadronic particles and jets as well as good determination of missing transverse energy.
- The muon detector must provide accurate muon identification and momentum resolution and ensure the assignment of the correct charge to muons over a large range of momenta.

The ATLAS detector is a  $4\pi$  detector with almost full solid angle coverage and it is symmetric in forward and backward direction with respect to the interaction point. ATLAS has a length of 44 m, a diameter of 25 m and a weight of about 7000 t. It is shown in Figure 3.3 with its main components and humans, to demonstrate the size proportions. The detector

<sup>11</sup>Jets which are identified to origin from a  $b$ -quark on parton level, can be marked. Then they are called  $b$ -tagged jets. This can be useful in physics analyses, e.g. top quark measurements. It is the same for  $\tau$ -tagging, when detected particles can be identified to origin from a  $\tau$  decay and can be marked as  $\tau$ -tagged.

<sup>12</sup>Jets which are identified to origin from a  $b$ -quark on parton level, can be marked. Then they are called  $b$ -tagged jets. This can be useful in physics analyses, e.g. top quark measurements. It is the same for  $\tau$ -tagging, when detected particles can be identified to origin from a  $\tau$  decay and can be marked as  $\tau$ -tagged.

is build of several different layers, starting close to the interaction point and outer detector elements are surrounding the previous. The inner detector is closest to the beam pipe and surrounded by a thin solenoid magnet, providing a solenoidal magnetic field of 2 T. This part is responsible for tracking measurements such as vertex identification and location, pattern recognition but also for momentum determinations and electron identification. To provide energy measurements, the electromagnetic (EM) calorimeter and the hadronic tile calorimeters are built surrounding the inner detector. In the forward region, the electromagnetic and hadronic endcap calorimeters as well as the forward calorimeters are built to allow energy measurements also in the forward direction. Electromagnetic and some hadronic calorimeters use liquid argon (LAr) technology and the hadronic tile calorimeter utilizes plastic scintillators for the measurements. It is important to ensure that all calorimeter components are thick enough to absorb all the energy of the particles. If particles still have energy after passing through the calorimeter system, the energy measurement of the particles will not be correct. Furthermore, the particles will give a signal in the outer muon detector, leading to a faulty muon measurement. The second effect is called *punch-through*. The calorimeters are surrounded by three large toroidal magnets, one barrel and two endcap magnets, inducing a magnetic field of 0.5 T to deflect the muons. The outermost part of the detector is the muon spectrometer to identify muons as well as their charge and momentum.

## Inner Detector

The inner detector part is built up of the *pixel detector*, the *SemiConductor Tracker* (SCT) and the *Transition Radiation Tracker* (TRT). The inner detector is shown in Figure 3.4 with the pixel detector closest to the beam pipe, followed by the semiconductor tracker and the transition radiation tracker. The inner detector has a length of 6.2 m and a diameter of 2.1 m. The entire inner detector is pervaded by a 2 T solenoidal magnetic field to deflect charged particles. From the measured particle tracks, the curvature of the deflection and the known magnetic field strength the momentum of the particle can be determined. Furthermore, electrons can be identified by the TRT.

The pixels and SCT sensors are made of silicon as semiconducting material. These components are especially exposed to high radiation doses due to the spatial closeness to the IP. After a certain radiation dose<sup>13</sup>, the original p-typed material becomes effectively n-typed. This effective doping is dependent on the temperature and in order to slow down its growing the sensors have an operation temperature of -5 °C to -10 °C. This also keeps the noise from leakage currents small, before and after the type inversion.

The pixel detector is the first component of the inner detector and the closest to the beam line. It has the highest granularity of all three parts. In the central region,  $|\eta| < 2.5$ , there are three layers of pixel detectors, arranged cylindrically around the beam pipe. The shortest distance between the IP and the first layer is about 50 mm, the distance between the IP and the third layer is 122 mm. In each forward direction the pixel detectors are arranged on three discs perpendicular to the beam axis in a range of  $495 \text{ mm} < z < 650 \text{ mm}$ . The 47232 pixels have a size of  $50 \times 400 \mu\text{m}^2$  and are placed on 1744 identical pixel sensors with a size of  $19 \times$

<sup>13</sup>After a 1 MeV neutron equivalence fluency  $F_{neq} \approx 2 \cdot 10^{13} \text{ cm}^{-2}$  the type inversion occurs.

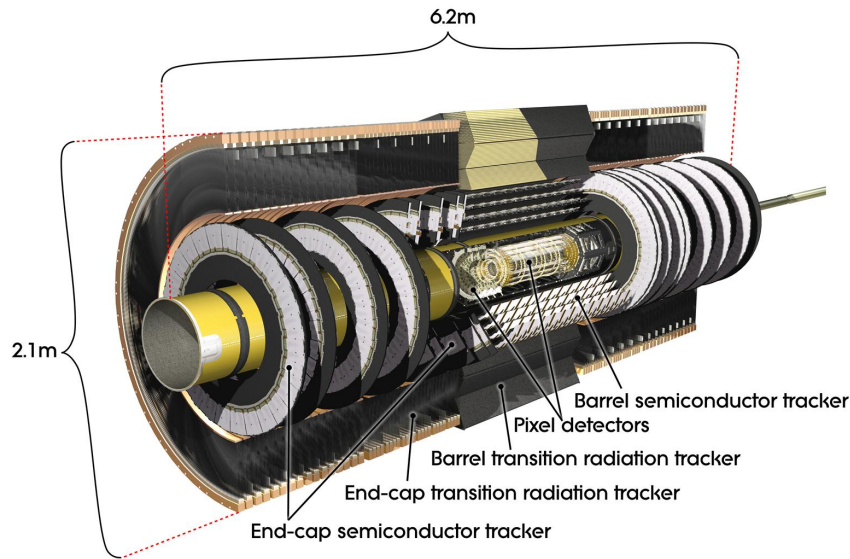


**Figure 3.4.:** The ATLAS inner detector with its main components pixel detectors, the semiconductor tracker and the transition radiation tracker [22].

$63 \text{ mm}^2$ . The total number of read out channels is about 80 million. The intrinsic accuracy of the pixels is  $10 \text{ }\mu\text{m}$  in  $(R-\varphi)$  and  $115 \text{ }\mu\text{m}$  in  $z$  for all three layers. The setup of the pixel detectors was chosen so that each particle should have three hits within the pixel detector. During the upgrade phase 0 in 2013, an additional layer of pixel detectors will be assembled between the beam pipe and the first existing layer [26, 27].

The SCT is the middle component of the inner detector. It is made of four silicon microstrip sensor layers in the barrel region arranged in concentric cylinders around the pixel detector. The length of the cylinders is about 1.7 m and the radii are between 299 mm and 514 mm. In the forward regions, the SCT is made up of seven discs for each side. They are arranged at a distance of 0.85 m to 2.7 m from the IP, perpendicular to the beam axis. In the barrel the strips are aligned parallel to the beam line and in the forward direction they are aligned radially to it. In order to measure both coordinates in the  $(R-\varphi)$  plane, there is a second set of strips which is rotated about 40 mrad with respect to the previous set. The complete barrel region and two discs in the forward regions are doubled with a rotated layer, giving eight layers in the central region and nine in each forward region. Every particle is supposed to have four hits in the SCT. This setup of the SCT allows an intrinsic accuracy of  $17 \text{ }\mu\text{m}$  in  $(R-\varphi)$  and  $580 \text{ }\mu\text{m}$  in  $z$  in central and forward region. There are 1512 SCT sensors in total, covering an area of about  $61 \text{ m}^2$ , leading to more than 6 million read out channels.

The final component of the inner detector is the TRT. In the barrel region it is made up of 73 layers of straw tubes each with a diameter of 4 mm and a length of 144 cm arranged in parallel and concentric to the beam line. The TRT surrounds the SCT at a radius of 554 mm and extends to 1082 mm. It is constructed such that particles within  $|\eta| < 2.0$  have usually about 36 hits in the straw tubes. In the forward region are 160 layers of straw tubes, each straw with a length of 37 cm, set up radially in wheels. It extends from 850 mm to

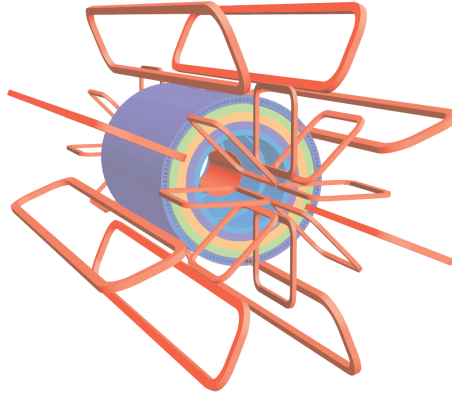


**Figure 3.5.:** A sketch of the ATLAS magnet system (red). In the innermost part the solenoid is located. The tile calorimeter is shown, surrounded by the eight coils of the toroidal barrel. The two toroidal endcaps are rotated  $22.5^\circ$  with respect to the barrel [22].

2700 mm in  $z$  direction from the IP. The straws are made of polyimide and coated with a thin aluminum layer ( $0.2\ \mu\text{m}$ ) and a thicker graphite-polyimide layer ( $6\ \mu\text{m}$ ) on one side and with a polyurethane layer ( $5\ \mu\text{m}$ ) on the other. The total wall thickness of the straws is only  $70\ \mu\text{m}$  but nevertheless they have excellent electrical and mechanical characteristics. In the center of the straw the anode, a tungsten wire plated with a thin gold layer and a diameter of  $31\ \mu\text{m}$ , is placed. The gas mixture in the straws consists of 70% Xe, 27%  $\text{CO}_2$  and 3%  $\text{O}_2$  is kept at 5-10 mbar overpressure. With the anode on ground potential and the cathode having a potential of  $-1530\ \text{V}$  the gain is typically about  $2.5 \cdot 10^4$  with an average electron collection time of 48 ns. With the given properties, the straw tubes provide an intrinsic accuracy of  $130\ \mu\text{m}$  in  $(R - \varphi)$  which is a little less precise as the pixel detector or SCT in contrast provides the TRT significantly more measured points over longer track paths. The total number of read out channels is about 35100.

The TRT is not only used for tracking measurements but also for electron identification. When a charged relativistic particle crosses the interface of two media with very different dielectric constants  $\epsilon_{1,2}$ , it emits so called *transition radiation* photons with energies of a few keV. They are absorbed by the Xenon in the gas mixture and hence, the signal strength becomes stronger compared to the signal only produced by minimum ionization. The amount of transition radiation is dependent on the mass of the particle and lighter particles produce more transition radiation than heavier particles. Hence, electrons are identified as hits with an enhanced signal.

### Solenoid Magnet

The ATLAS magnet system consists of one superconducting *solenoid magnet* providing a magnetic field in the inner detector and three superconducting *toroidal magnets* deflecting muons, shown in Figure 3.5. The solenoid is designed as a 5 cm thick cylindrical shell, surrounding the inner detector with an outer diameter of 2.56 m, a length of 5.8 m and a total weight of about 5.4 t. It provides a magnetic field of 2 T to deflect charged particles in the inner detector. To keep the energy loss in front of the calorimeters at a minimum, it has a

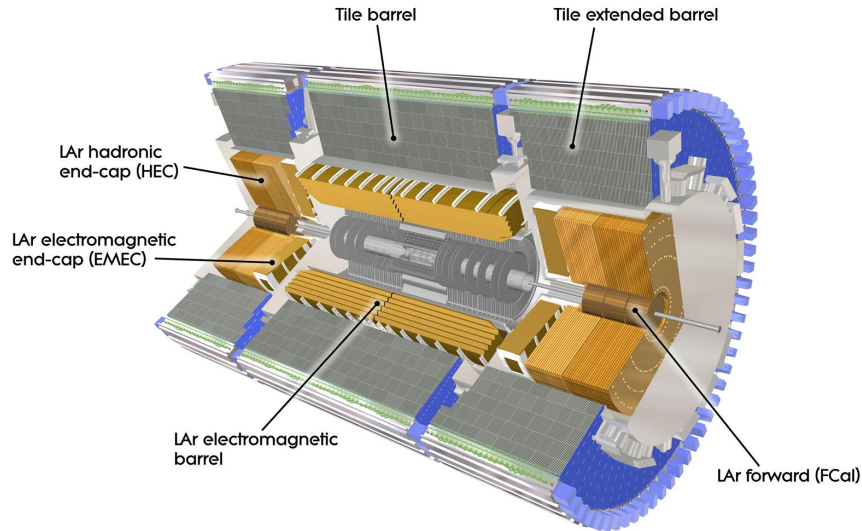


*Figure 3.6.:* The ATLAS calorimeter system with electromagnetic and hadronic calorimeters [22].

radiation length<sup>14</sup> of  $0.66 X_0$ . About 30 minutes are needed to charge or discharge the magnet at its operating temperature of 4.5 K.

## Calorimeter

Calorimeters are used to measure the energy of particles. When passing through the calorimeter, the particles interact with the calorimeter material and produce a shower of secondary particles. When the particle has deposited its complete energy in the calorimeter, the charge from the ionization or the scintillator light can be measured and is proportional to the energy of the original particle. ATLAS uses *sampling calorimeters*<sup>15</sup> for both electromagnetic and hadronic calorimetry, where active and passive material layers alternate. In the active material the deposited energy is measured whereas the passive layers are used to absorb energy of the particles without measuring it. Only small fractions of the energy are deposited in the active layer and finally measured. Hence, it is called the *sampling fraction* and it has to be corrected for the energy loss in the passive material. This method allows the particles to deposit their complete energy in smaller and more compact calorimeters. The ATLAS calorimeter systems is shown in Figure 3.6, with electromagnetic and hadronic calorimeters in central and forward direction.

<sup>14</sup>The radiation length is defined as the length an electron travels in a medium until it has only  $1/e$  of its initial energy.

<sup>15</sup>Contrary to *homogeneous calorimeters* where the entire material contributes to the energy measurement. They often have better energy resolutions compared to sampling calorimeters, but are much more expensive. Homogeneous calorimeters can only be used for electromagnetic calorimetry.

### Electromagnetic Calorimeter

The electromagnetic (EM) calorimeter primarily measures the energy of electrons, positrons and photons. Photons with energies above 5-10 MeV interact with the active medium predominantly via pair production. Photons with lower energies, interact via the photoelectric effect or Compton scattering. Electrons and positrons ionize the active material or lose energy via bremsstrahlung. As the showering develops, thousands of photons or electron-positron pairs can be produced, which further produce photons and electron-positron pairs. This *multiplication* leads to a shower maximum. When the average energy of the particles is below a certain value, multiplication does not further occur and the multiplicity of the secondary particles decreases. The shower depth  $d_{shower}$  is logarithmically dependent on the energy of the incoming particle

$$d_{shower} \propto \log \frac{E}{E_c} \quad (3.7)$$

with  $E$  the energy of the particle and  $E_c$  the critical energy<sup>16</sup>. Hence, calorimeters can have a compact design and still be usable for large energy ranges.

Transverse to the propagation direction the shower is broadened. This is described by the *Molière radius*

$$R_m = 0.0265 X_0 (Z + 1.2) \quad (3.8)$$

with the radiation length  $X_0$  and the atomic number  $Z$  of the calorimeter material. The active medium at ATLAS is liquid argon (LAr) since it has intrinsically characteristics which are favorable, like its radiation hardness, a linear behavior of the energy depositions over time and a stable response over time.

The EM calorimeter at ATLAS is located outside the central solenoid and involves one barrel and two endcaps. All parts consist of accordion-shaped lead absorbers as the passive medium alternating with LAr in between as the active medium. The kapton electrodes are always in the middle of the LAr gap, allowing a maximum drift length of 2.1 mm and a corresponding drift time of 450 ns at 2000 V operation voltage. The *ElectroMagnetic Barrel* (EMB) is located in the region  $|\eta| < 1.475$ , mounted coaxially around the inner detector and is divided into two half-barrels with a small gap of 4 mm at  $z = 0$ . The total length is 6.2 m and the EMB has a weight of 114 t. It extends radially from 1.4 m to 2 m. In front of the EMB at  $|\eta| < 1.8$ , a presampler is installed. This is a thin instrumented LAr layer, which provides an estimation of the energy lost in material in front of the EMB. The total amount of material in front corresponds to  $1.7 X_0$ . As shown in Figure 3.7, in the EMB the waves of the accordion shaped layers are running radially, providing a complete azimuthal  $\varphi$  coverage without any cracks. The folding angle and wave amplitudes change with increasing radius to keep the LAr gaps of the same size. The total thickness of the EMB is between  $22 X_0$  and  $33 X_0$ . The depth is divided into three longitudinal layers: the first has a depth of  $4.3 X_0$ , the second of  $16 X_0$  and the third  $2 X_0$  also depicted in Figure 3.7. The first layer has fine granularity strips in the pseudorapidity,  $\Delta\eta \times \Delta\varphi = 0.025/8 \times 0.1$ , which is important to allow the distinction between photons and neutral pions ( $\pi^0$ ) which decay into two photons. Together with the second layer, it also determines the photon pseudorapidity. The second layer with a

<sup>16</sup>Energy loss at low energies is dominated by ionization and for high energies by bremsstrahlung. The critical energy defines the energy when both processes contribute equally.

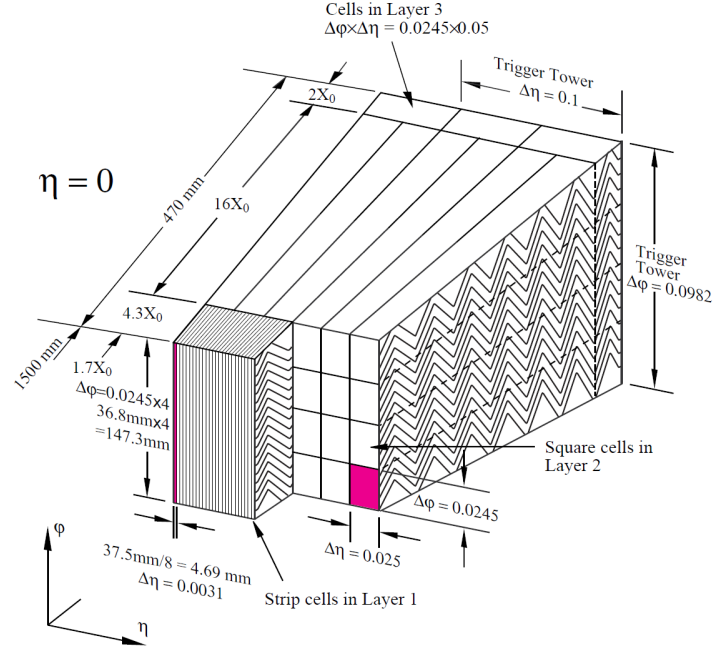


**Figure 3.7.:** An EMB module with accordion layers and different granularities is shown [22].

granularity of  $\Delta\eta \times \Delta\varphi = 0.025 \times 0.025$  is the largest. The shower maximum is supposed to lie within this depth and hence most of the energy is deposited there. The third layer with a granularity of  $\Delta\eta \times \Delta\varphi = 0.05 \times 0.025$ , should contain only energy deposits after the shower maximum. The given granularities are just exemplary for very central regions (approximately  $|\eta| < 1.4$ ), they vary with the pseudorapidity. The calorimeter cells are combined to so called *trigger towers* with  $\Delta\eta \times \Delta\varphi = 0.1 \times 0.1$  and are the input elements for the Level 1 calorimeter trigger. For the entire EMB more than 101700 read out channels are necessary.

The two 63 cm thick and 27 t heavy, wheel shaped *ElectroMagnetic End Caps* (EMEC) are located directly behind the EMB in  $z$  direction and cover a pseudorapidity range of  $1.375 < |\eta| < 3.2$ . The endcaps consist of two separate wheels: an inner wheel at  $2.5 < |\eta| < 3.2$  and an outer wheel at  $1.375 < |\eta| < 2.5$ . The waves of the accordion structure are aligned parallel to beam line in such a way that again, the entire azimuthal range is covered without cracks. Each endcap has a minimum depth of  $24 X_0$  and is also additionally divided into longitudinal segments. Similar to the EMB the outer wheel has three different layers. The inner wheel has only two additional segments, with coarser granularity. For the EMEC, the total number of read out channels is about 62000. The forward region is covered by the forward calorimeter, which will be discussed later.

The energy resolution of the EM calorimeter is given by

$$\frac{\sigma_E}{E} = \frac{10\%}{\sqrt{E}} \oplus 0.7\%. \quad (3.9)$$

The first term, dominant for low energies, is the *statistical term* which takes fluctuations in the showering into account. The *constant term*, arising from systematical detector effects such as non-uniform response performance or calibration errors, becomes dominant at high energies.

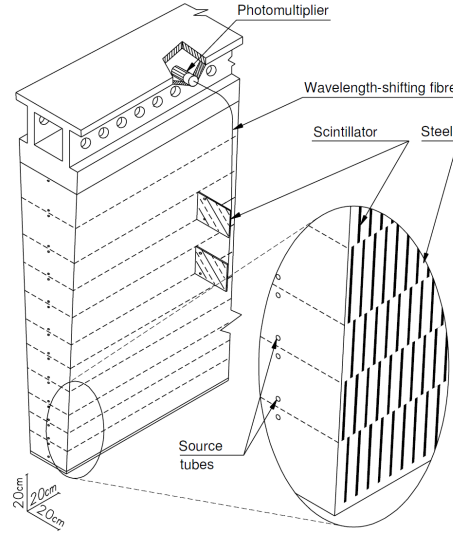


**Figure 3.8.:** An hadronic tile module is shown. The alternating structure of the scintillating tiles and the steel absorbers is visible [22].

### Hadronic Calorimeter

The hadronic calorimeter measures the energy of hadrons, such as protons, neutrons or pions. Hadronic particles interact differently than electromagnetic particles, leading to a different showering development. Hadronic particles interact via the strong force with the nuclei of the calorimeter material losing energy in inelastic processes such as spallation or nuclear fission. This energy is not measured by the calorimeter and called *invisible energy*. In addition, hadronic showers always contain electromagnetic contributions, for example from the pion decay  $\pi^0 \rightarrow \gamma\gamma$ . Hence, the correction for this invisible energy is difficult. One possible way is to use *compensating calorimeters*, where uranium or other fissionable material is used as active calorimeter material. When high energetic hadrons interact with the nuclei, a series of reactions can be initiated and the calorimeter response is enhanced. ATLAS uses *non-compensating calorimeters*, which means the calorimeters use no easily fissionable material and hence an offline calibration has to be applied.

At ATLAS the *hadronic tile calorimeter* uses alternating plastic scintillating tiles as active and steel as passive medium at a volume ratio of 1 : 4.7. A schematic view of one module is shown in Figure 3.8. The more than 464000 scintillating tiles are made of polystyrene, doped with two different wave-shifting fluors<sup>17</sup>. When ionizing particles pass through the scintillator they produce ultraviolet scintillation light in the primary scintillator material. Because the base material is nontransparent for UV photons, the doping materials are necessary to shift the UV light to the visible range. The photons of each tile are collected by two, also wave-shifting polystyrene fibers and read out at the end of each module by two different *Photo Multiplier Tubes* (PMT).

The tile calorimeter consists of three parts: one barrel and two extended barrels. The barrel surrounds the EMB in the region  $|\eta| < 1.0$  and has a length of 5.8 m. The extended barrel

<sup>17</sup>1.5% PTP and 0.044% POPOP.

spans from  $0.8 < |\eta| < 1.7$  with a length of 2.6 m, an inner radius of 2.28 m and an outer radius of 4.25 m. The structure allows full azimuthal coverage without cracks and due to the overlap in the pseudorapidity ranges of barrel and extended barrel, the range  $|\eta| < 1.7$  is almost completely covered. Nevertheless, there is a gap between the barrel and the extended barrel filled with cables, power supply and services for the inner detector and the EM calorimeter. Special steel-scintillating modules are installed in that gap, which allow the estimation of the energy lost in the crack region. The barrels are segmented into 64 modules, corresponding to  $\Delta\varphi \approx 0.1$ , shown in Figure 3.8. By cleverly grouping the wavelength-shifting fibers, each module gets three radial sampling depths. In the barrel, at  $\eta = 0$ , the layers correspond to an interaction lengths<sup>18</sup>  $\lambda$  of  $1.5\lambda$ ,  $4.1\lambda$  and  $1.8\lambda$ , leading to a total tile calorimeter depth of  $7.4\lambda$ . Taking all the material in front of the tile calorimeter into account, the depth at the end corresponds to  $9.7\lambda$ . In the extended barrel the depths are slightly different with  $1.5\lambda$ ,  $2.6\lambda$  and  $1.8\lambda$ . The granularity for the first two layers is  $\Delta\eta \times \Delta\varphi = 0.1 \times 0.1$  and for the third  $\Delta\eta \times \Delta\varphi = 0.2 \times 0.1$ . The barrel has a total of 5760 readout channels and the two extended barrels have 4092.

The two **Hadronic End Cap Calorimeters** (HEC) are placed directly behind the EMEC. Instead of scintillating tiles, LAr is used as active medium and instead of steel, the absorber medium is copper. It extends over  $1.5 < |\eta| < 3.2$  and hence overlaps with the tile calorimeter, which ends at  $|\eta| = 1.7$ . Each HEC is divided into two wheels, the first called HEC1 and the second, behind the first in  $z$  direction, called HEC2. Both, HEC1 and HEC2, have two longitudinal segments, leading to four wheels for each endcap. Each of the four wheels is made of 32 wedge-shaped modules, giving 256 modules in total. HEC1 consists of one 12.5 mm thick front copper plate and 24 copper plates with a thickness of 25 mm. The inner radius of the first nine plates is 0.372 m and the remaining have a radius of 0.475 m. The copper front plate of HEC2 has a thickness of 25 mm and additionally 16 copper plates with a thickness of 50 mm. The inner radius of all HEC2 plates is 0.475 m. The outer radius is 2.03 m. The gaps between the copper plates have a length of 8.5 mm and are divided by three electrodes into four smaller gaps. These smaller gaps with a width of 1.8 mm each, are the LAr drift zones. With a nominal voltage of 1800 V applied, electrons have an average drift time of 430 ns. The sampling fraction for HEC1 is 4.4% and for HEC2 is about 2.2%. The readout cells have a size of  $\Delta\eta \times \Delta\varphi = 0.1 \times 0.1$  for  $1.5 < |\eta| < 2.5$  and in the more forward region  $2.5 < |\eta| < 3.2$  the granularity is coarser with  $\Delta\eta \times \Delta\varphi = 0.2 \times 0.2$ . The two HECs have a total of 5632 readout channels.

The energy resolution of the hadronic calorimeter is

$$\frac{\sigma_E}{E} = \frac{50\%}{\sqrt{E}} \oplus 3\%. \quad (3.10)$$

### Forward Calorimeter

To complete the calorimeter range up to high pseudorapidities two **Forward Calorimeters** (FCal) are installed at both sides of the barrel to cover the very forward ranges. The FCal covers a pseudorapidity region of  $3.1 < |\eta| < 4.9$  and has a small overlap with the EMEC and

<sup>18</sup>The interaction length is defined as the average path a high energetic hadron needs to reduce its energy to  $1/e$  of its initial energy.

the HEC, both extended to  $|\eta| = 3.2$ . It is built as a cylinder into the wheels of the EMEC and HEC coaxially around the beam line. It is 4.7 m away from the IP and the front face is  $\sim 1.2$  m behind the EMB calorimeter to reduce neutron albedo in the inner detector. Hence, the depth is tightly restricted and the entire system must be very dense to ensure that particles deposit their complete energy in the FCal, but at the same time a precise measurement of the energy must be possible. Due to the extremely high particle fluxes, the LAr gaps must be very small to prevent ion buildup and the amount of absorber material must be maximized. Since the FCal is used for electromagnetic and hadronic measurements, each FCal consists of three 45 cm long modules. The first (FCal1) is mainly used for electromagnetic measurements and also uses LAr as active and copper as absorption medium. The second and third layer (FCal2 and FCal3) are optimized for hadronic measurements and also utilize LAr as detection material but tungsten as passive material to minimize the Molière radius and to maximize the absorption of the hadronic energy. The structure of each FCal module is different from the EM calorimeter. The FCal1 module consists of a metal matrix drilled with over 12200 holes to provide the electrode structure. Into the holes the electrodes are assembled parallel to the beam line. Each electrode comprises a copper tube filled with a copper rod and is surrounded by a plastic fiber. In the gap between the rod and the fiber the LAr is filled for the energy measurements. The FCal2 and FCal3 have less electrodes 10200 and 8224 respectively and the rods are made of tungsten instead of copper. The LAr gaps have a width of 0.269 mm for the FCal1, 0.376 mm for the FCal2 and 0.508 mm for the FCal3. They are much smaller compared to the LAr gaps in the EMB or EMEC. For all three modules, the electric field in the gaps is the same, leading to average drift times of 60 ns, 84 ns and 113 ns, respectively. For this setup the total absorption length of the FCal, including all three modules, is about  $10 \lambda$ . The total number of read out channels is over 1700 and the achieved energy resolution of the FCal is

$$\frac{\sigma_E}{E} = \frac{100\%}{\sqrt{E}} \oplus 10\%. \quad (3.11)$$

The combination of electromagnetic and hadronic calorimeters, as well as barrel, endcaps and forward parts allow accurate energy measurements for electrons, photons and hadrons over almost full azimuthal coverage and a large pseudorapidity range of  $|\eta| < 4.9$ .

### Toroid Magnets

The large air-cored toroidal magnets consist of one barrel and two endcaps, also shown in Figure 3.5. The barrel toroid induces a magnetic field in the pseudorapidity range  $|\eta| < 1.4$  and is made of eight coils arranged symmetrically and radially around the beam line. The total length is 25.3 m and the inner and outer radii are 4.7 m and 10.05 m, respectively. The two endcaps are on both sides of the barrel, inducing a magnetic field in the pseudorapidity range  $1.6 < |\eta| < 2.7$ . They have a length of 5 m and an outer radius of 5.35 m. The endcaps are rotated  $22.5^\circ$  with respect to the barrel, to optimize the magnetic field in the transition region  $1.4 < |\eta| < 1.6$ . The toroid magnet induces a magnetic field of  $\sim 0.5$  T at an operating temperature of 4.6 K.

The total magnet system induces a magnetic field in a volume of  $\sim 12000 \text{ m}^3$  and stores a total energy of 1.6 GJ.

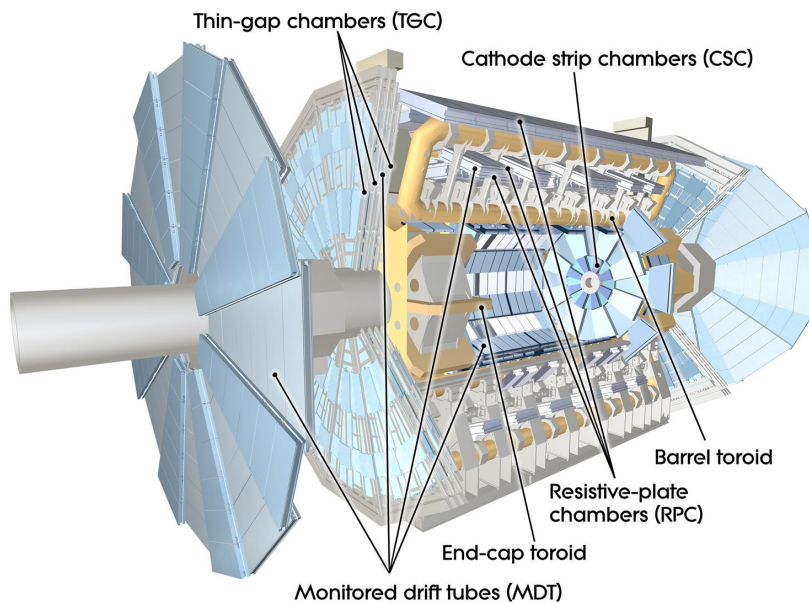


Figure 3.9.: The ATLAS muon system with its main components [22].

## Muon Spectrometer

The muon spectrometer marks the outermost part of the detector. It is possible to put the muon detector behind so much material, since the muons do not lose as much energy as electrons via bremsstrahlung. The muon detector provides, besides the high precision measurements for muon tracks and momentum, its own trigger system. A schematic view of the muon detector with its main components is given in Figure 3.9. The toroidal magnets are providing a magnetic field of 0.5 T to deflect the muons in the  $\eta$ -plane. In the central part  $|\eta| < 1.4$  the particles are deflected due to the magnetic field of the barrel toroids, in the forward region  $1.6 < |\eta| < 2.7$  they are deflected by the field of the endcaps of the toroid and in the region between  $1.4 < |\eta| < 1.6$  the deflection arises from a combination of the two fields. Hence, this last region is referred to as *transition region*. The muon system is made of three cylindrical shells surrounding the previous barrel components at radii 5 m, 7.5 m and 10 m and cover a pseudorapidity range of  $|\eta| < 2.7$ . It is situated in and on the coils of the magnets, divided into eight octants. Each octant consists of two sectors, separated in the  $\varphi$  angle. The sizes are slightly different and hence, they are referred to as small and large sector. They are assembled in such a way that they overlap in the pseudorapidity range to minimize the gap areas in the detector. At  $\eta = 0$ , there is a gap in the muon detector to allow space for services of the magnets, calorimeter and inner detector. It is not bigger than 2 m at the largest point, corresponding to  $|\eta| \leq 0.08$  in the large section and  $|\eta| \leq 0.04$  in the smaller section. In forward direction it is made of four wheels in the  $(x - y)$  plane at distances of 7.4 m, 10.8 m, 14 m and 21.5 m from the IP, respectively.

The precision measurements of the muon momentum is provided by the *Monitored Drift Tubes* chambers (MDT). In the barrel, each chamber is made up of three to eight layers of drift tubes, filled with an Ar-CO<sub>2</sub> gas mixture (39:7) and operated at 3 bar. The anode is a

tungsten-rhenium wire with a diameter of  $d = 50 \mu\text{m}$  at a potential of 2080 V. The advantage of using this gas mixture is that it has good aging properties. The main disadvantage is a non-linear behavior of the spatial drift time relation. Together with the long drift times of up to 700 ns, arising from the radial drift geometry, it reduces the spatial resolution. Furthermore, the spatial-drift time relation is dependent on external conditions, such as temperature or pressure and hence, an online calibration is needed to guarantee high spatial resolutions under changing external conditions. The average resolution of the tubes is  $80 \mu\text{m}$  and the resolution of the chambers is  $80 \mu\text{m}$ . The total number of MDTs in the detector is 1088, covering an area of  $5500 \text{m}^2$ .

In the forward region, the particle flux is extremely high and hence, *Cathode Strip Chambers* (CSC) are used in the pseudorapidity range  $2.0 < |\eta| < 2.7$  of the first wheel in each forward direction. Each chamber is also divided in the azimuthal plane into eight segments containing a small and a large chamber. The CSCs are multiwire proportional chambers, with anode wires of a diameter  $d = 30 \mu\text{m}$  aligned in radial direction so that the cathode planes become divided into orthogonal strips. Both coordinates are measurable with this design, with a resolution of  $40 \mu\text{m}$  in the bending plane, and  $5 \text{mm}$  in the orthogonal, non-bending plane. This difference arises mainly due to the coarser cathode segmentation and the different read out pitches. The gas mixture is also a Ar-CO<sub>2</sub> mix (80 : 20) and, with the anode operating voltage of the 1900 V, the average electron drift time is less than 40 ns, allowing a fast timing resolution of 7 ns. Another advantage of the CSCs are the low neutron sensitivity, due to small gas volumes and a hydrogen-free gas mixture.

Another important task of the muon detector is the triggering of muons. The trigger is designed to accept muons in the pseudorapidity range  $|\eta| < 2.4$  and full azimuthal range. This is a large pseudorapidity range with very different experimental conditions in the central and the forward region, requiring two separate technologies. In the barrel region, *Resistive Plate Chambers* (RPC) are used. There are three layers of RPCs mounted in concentric cylinders around the beam line. The first two, RPC1 and RPC2 are located directly before and behind the middle layer of the MDT and the third, RPC3, is behind the outermost MDT layer. The two inner layers provide a low  $p_T$  muon trigger with  $6 \text{GeV} < p_T < 9 \text{GeV}$  and the two outer layers, allow a high  $p_T$  triggering with  $9 \text{GeV} < p_T < 35 \text{GeV}$ . Each RPC is made of two parallel electrode-plates at distances  $d = 2 \text{mm}$  filled with a gas. The gas is a mixture of C<sub>2</sub>H<sub>2</sub>F<sub>2</sub>/Iso-C<sub>4</sub>H<sub>10</sub>/SF<sub>6</sub> (94.7 : 5 : 0.3), allowing a relatively low operation voltage of 9800 V and is non-flammable. The field between the plates is 4900 V/mm and ionizing particles passing the RCP induce avalanches towards the anodes. The average signal width is about 5 ns. The RPCs provide high rate capabilities as well as good spatial and time resolution.

Complementary, *Thin Gap Chambers* (TGC) are used in the forward region. Two layers of the TGCs are mounted around the inner MDT wheel and seven layers are mounted around the middle MDT wheel. The TGCs are a specific case of multiwire proportional chambers with a wire-to-wire distance of 1.8 mm and a smaller wire-to-cathode distance of 1.4 mm. The gas gaps are 2.8 mm wide and filled with a gas mixture of CO<sub>2</sub>/n-C<sub>5</sub>H<sub>12</sub> (n-pentane) (55 : 45) which is a quenching gas, minimizing streamer occurrences but is also flammable. The anode, at a potential of 2900 V allows a gain of  $3 \cdot 10^5$ . Besides the triggering function, the TGC also provide a second measurement of the muon coordinate in the non-bending azimuthal plane. The TRC has a good time resolution and high rate capabilities.

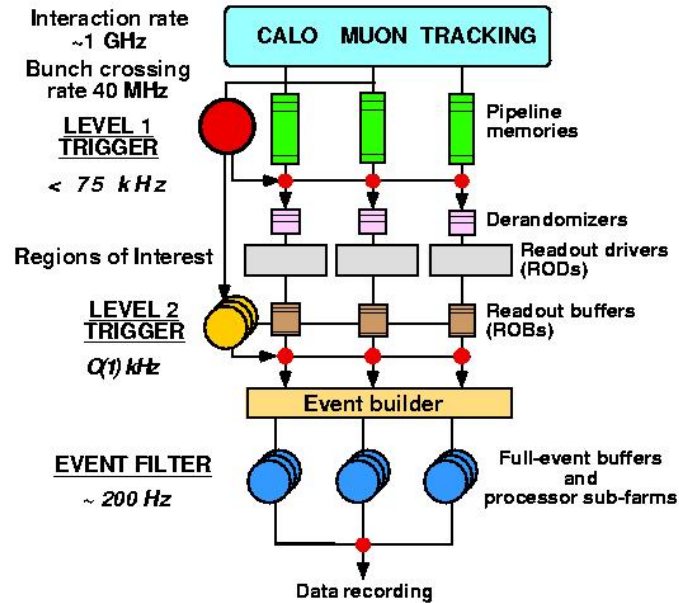


*Figure 3.10.:* The ATLAS Trigger system. The first level reduces the event rate to less than 75 kHz. The second level reduces the rate to 3.5 kHz and finally after the event filter, the rate is reduced to 200 Hz [28].

### 3.3. ATLAS Trigger System

When the LHC is operating at design luminosity, bunch crossings occur every 25 ns in the detector. Each of the collisions has up to 25 inelastic interactions, giving an event rate of 1 GHz. Most of new physics processes have small cross sections and hence, the majority of these events are not useful in the search of new physics. Furthermore, due to limited data storage and bandwidth, an efficient and reliable system of selecting interesting events is required. This is provided by the ATLAS trigger system, which consists of three different levels. Since the first decisions have to be taken before reading out the entire data and storing it, the first level is an online selection implemented in the hardware. On the contrary, the second and third level are software based algorithms also using online data. Each level includes more information of the event than the previous one. When an event is accepted at all three levels it is finally stored. The trigger system reduces the event rate to 200 Hz with an average event size of 1.3 Mbyte. An overview of the entire system is given in Figure 3.10.

#### Data Acquisition System

The *Data Acquisition system* (DAQ) manages the entire data processing, including the raw data from the detector, buffering data which is not needed for trigger decisions, providing data when trigger components require detailed information about objects until the permanent storage of the events. It utilizes over 1600 detector specific read out links at a rate of 75 kHz to move the data. Furthermore, the DAQ includes configuration, controlling and monitoring

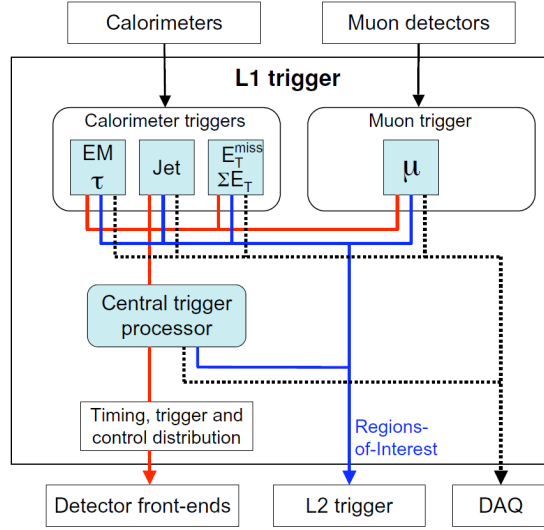


**Figure 3.11.:** The L1 trigger in ATLAS. The calorimeter and muon trigger provide information which are sent to the CTP. There the L1 trigger decision is taken. In case of L1A the signal the event is read out by the DAQ [22].

systems of hardware and software elements to ensure stable data-taking.

## Level-1 Trigger

The *Level-1* (L1) trigger identifies objects such as electrons, photons, muons or jets with high transverse energy as well as events with large missing transverse energy. The L1 trigger is hardware implemented, checking particle multiplicities or flags, marking which thresholds have been passed. Since not all information from the collision is needed, the data is buffered in the *front end electronics* until the decision is taken. The time needed for a decision is shorter than  $2.5\ \mu\text{s}$ . Furthermore, the L1 trigger has to assign the correct bunch crossing (*Bunch Crossing IDentification*, BCID) to each object. This is challenging, since the time-of-flight for muons is longer than 25 ns and the signals in the calorimeter last in average over four bunch crossings (100 ns). An overview of the L1 trigger is given in Figure 3.11. Since the L1 trigger utilizes information from the calorimeter and muon systems, they are called *calorimeter triggers* and *muon trigger*, respectively. The information of these two parts are sent to the *Central Trigger Processor* (CTP) where the final L1 trigger decision is taken. In case an event was accepted, the *L1 Accept* (L1A) is sent back to the detector front end and read out to the DAQ system. The location of the *Region of Interest* (RoI), the region with a large energy deposition, is sent to the *RoI builder* and then to the L2 trigger. Furthermore, the CTP can apply a prescale factor to only take a certain fraction of the accepted data. The concept of prescales is discussed at the end of this Chapter.

## Calorimeter Triggers

The *L1 Calorimeter* (L1Calo) trigger processes 7168 analog trigger tower signals from the EM and hadronic calorimeters. It is located in a service cavern next to the detector. The compact design with minimal cable links and crates allows for a latency of 2.1  $\mu\text{s}$ . The L1Calo trigger has two subsystems to process the data. In the *PreProcessor* (PPr), the analog signal is converted into a digital signal as well as the correct bunch crossing identified. Afterwards, the *Cluster Processor* (CP) parallel to the *Jet/Energysum Processor* (JEP) are implemented. In the CP, electron, photon and tau candidates are detected whereas the JEP produces jet trigger elements and energy sums as well as first rough missing transverse energy estimations. Additionally, the multiplicity as well as flags, marking the passed thresholds, are set and the information sent to the CTP, where the trigger decision is taken.

### Preprocessor

For the preprocessor eight crates are available, four processing electromagnetic trigger towers and four processing hadronic trigger towers. One crate comprises 16 *PreProcessor Modules* (PPM) and on each PPM are 16 *Multi Chip Modules* (MCM), responsible for the main signal processing. Each PPM has 64 analog input signals from trigger towers and hence each MCM processes four trigger tower signals. At a collision rate of 40.08 MHz the FADC<sup>19</sup> converts the analog into a digital signal. To account for differences in the time-of-flight or signal-path length of the signals, the ASIC<sup>20</sup> synchronizes them in steps of 1 ns. This is important to identify the correct bunch crossing of the objects. Since the calorimeter signals last for several bunch crossings, the BCID is done by locating the maximum of the signal. For signals which are not saturated, this can be easily done by a peak-finding algorithm. For saturated signals, an advanced strategy is necessary, to estimate the maximum. The height of the signal corresponds to the energy of the object and in case of a saturated pulse it is higher than 250 GeV. Saturated signals are flagged, but more precise energy measurements are not necessary at that level. Furthermore, by using a look-up table a pedestal subtraction, a noise threshold and energy calibrations are applied. The signals are transmitted to the CP and JEP via three LVDS<sup>21</sup>, to ensure that not all signals of one PPM are sent in parallel.

### Cluster Processor

To identify electron or photon candidates, the CP uses a so called *sliding-window algorithm*, sketched in Figure 3.12 (left). Since these particles are expected to have energy deposits exclusively in the EM calorimeter only trigger towers from this detector part are considered. To identify electrons or photons a window of  $4 \times 4$  trigger towers runs over all possible calorimeter cells, overlapping in  $\varphi$  and  $\eta$  in 0.1 steps. All four possible two-towers transverse energy sums, either  $1 \times 2$  or  $2 \times 1$ , in the inner  $2 \times 2$  window are calculated and at least

<sup>19</sup>Flash Analog Digital Converter.

<sup>20</sup>Application Specific Integrated Circuit.

<sup>21</sup>Low Voltage Differential Signaling.

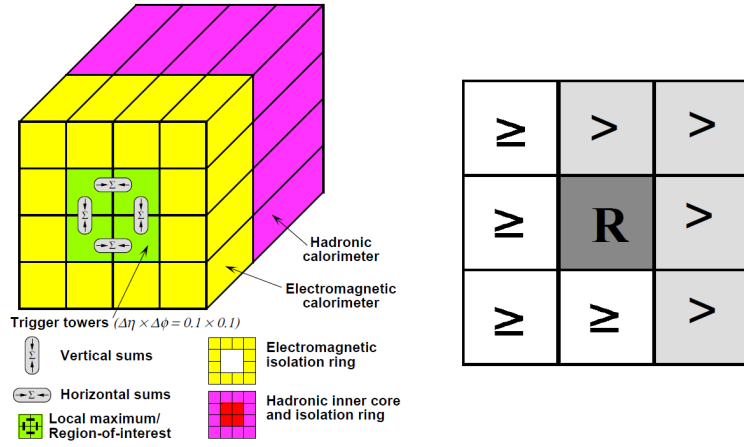


**Figure 3.12.:** Sliding  $4 \times 4$  window with surrounding cells (left). On the right side, the requirements to find a local maximum. 'R' denotes the tested  $2 \times 2$  cluster [22].

one has to have an energy above one of the eight programmable thresholds. Furthermore, isolation criteria are set: not only the energy of the 12 EM trigger towers surrounding the inner  $2 \times 2$  cluster but also the sum of the  $2 \times 2$  hadronic trigger towers behind the inner cluster as well as the 12 hadronic towers around that, must be below certain isolation-vetos. In order to avoid double counting of the cluster, it is required that the sum of the four central electromagnetic and hadronic cells is a local maximum, compared to the eight directly neighboring towers. Four of these neighboring trigger towers must be truly 'smaller' than the maximum, whereas the other four are allowed to be 'smaller than or equal' to the local maximum, seen in Figure 3.12 (right), to avoid the comparison of digital sums with the same values. The corresponding region of interest (RoI) is defined by the location of the  $2 \times 2$  inner cluster. The identification of  $\tau$  leptons is similar, but due to the hadronic decay, energy deposits in the hadronic calorimeter are possible and have to be included in the search.

### Jet/Energy-Sum Module

The jet elements are sums from  $2 \times 2$  EM trigger towers plus  $2 \times 2$  hadronic trigger towers. This is due to the showering of jets, which starts already at the end of the EM calorimeter and has its shower maximum in the hadronic calorimeter. The same sliding-window algorithm as for the CP is used with window sizes of  $2 \times 2$ ,  $3 \times 3$  and  $4 \times 4$  jet elements, corresponding to sizes in  $\eta$  and  $\varphi$  of  $0.4 \times 0.4$ ,  $0.6 \times 0.6$  and  $0.8 \times 0.8$ , respectively. Jet algorithms, using different sizes of jet elements have different advantages; bigger windows include more jet energy and hence have higher efficiencies, whereas smaller windows can resolve smaller jets, which are close to each other. The sums from the different window sizes are compared to the eight adjustable thresholds and are required to be a local maximum, as in the CP, to avoid double-counting. The RoI is defined by the coordinates of the local maximum, shown in Figure 3.13 for variable window sizes. Furthermore, the total transverse energy and the total missing transverse energy are determined.

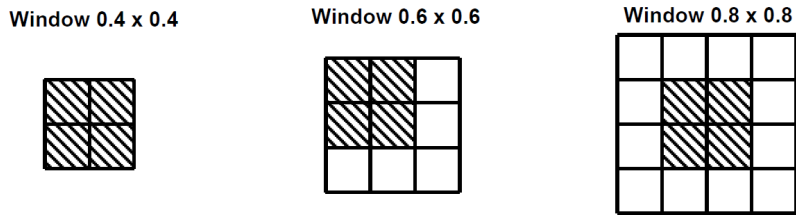


**Figure 3.13.:** Three different sliding window sizes in the JEM. The shaded areas represent the RoI's. For jet algorithms based on  $2 \times 2$  and  $4 \times 4$  jet elements, the position is unambiguous, whereas for the  $3 \times 3$  jet elements four RoI locations are possible [22].

### Central Trigger Processor

After passing the CP or JEM, the multiplicities and flags of the passed thresholds are sent to the CTP. In a lookup table specific trigger conditions are checked and in case they are fulfilled, a flag is set to mark the passed condition. Additional trigger requirements, such as prescale factors for specific trigger conditions are also applied. If the object is accepted by the CTP, the L1-Accept (L1A) signal is sent to the front end electronics, to allow the DAQ to read out the event data. Furthermore, the location of the RoI is sent to the RoI builder and then to the L2 trigger.

### Level-2 trigger

The L2 and the Event Filter combined, are called the *High Level Trigger* (HLT). Contrary to the L1 trigger they are both software based, processing the events on computer farms. After successfully passing the L1 trigger, the coordinates of the RoI are sent to the L2 trigger. The L2 trigger requests detailed event information with full granularity from the DAQ within the RoI. This corresponds to 2% of the entire data of the event, in order to keep the processing time as low as possible, in average about 40 ms per event. Using the full granularity of the calorimeter cells within the RoI, allows a better resolution of the energy. In addition, tracking information of the inner detector are used to improve particle identification, especially of electrons and photons, as well as shower shapes from the calorimeters to distinguish between hadronic and electromagnetic particles. Whether an event is accepted by the L2 trigger depends on the validity of conditions (e.g. multiplicity or energy thresholds), on specifically set prescales and pass through<sup>22</sup> factors. The L2 trigger has an event rejection factor of about 30, reducing the event rate to 3.5 kHz.

### Event Filter

The second part of the HLT is the *Event Filter* (EF) and the final trigger level in ATLAS. When an event is accepted by the L2 trigger, it is sent to the EF where the entire event

<sup>22</sup>Some triggers take a certain amount of data, without applying the specific trigger conditions.

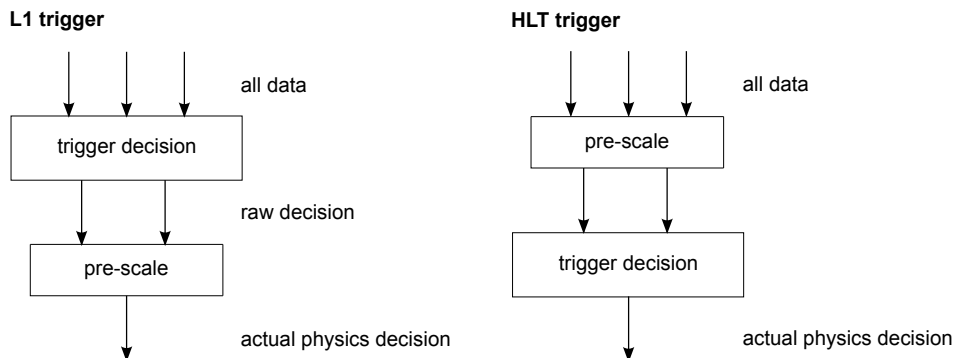


**Figure 3.14.:** The prescales for the ATLAS trigger. The L1 has a deterministic prescale applied after the trigger decision (left), whereas the HLT has a non-deterministic prescale before the trigger decision applied (right).

is reconstructed with full granularity using offline reconstruction algorithms and analysis procedures. With an average decision time of 4 s, the EF reduces the rate to 200 Hz. Similar to the L2 trigger, programmable trigger conditions, prescales and pass-through factors determine the trigger decision. Depending on which trigger conditions were passed, the EF classifies the event in which data stream it is permanently stored. After successfully passing the trigger system, the event is stored for offline processing. The average size of a stored event is about 1.3 megabyte.

## Prescaling

It is expected that many new physics processes appear at high energies which is why events with high energetic particles are especially interesting to study. Due to the limited amount of storage, it is necessary to limit lower threshold triggers in their accepting rate. As already mentioned before, this is done by so called prescales, constant factors, applied to take only a specific percentage of the data. This is necessary since without applying prescale factors, lower threshold triggers will accept a lot more events than higher threshold triggers and it will be impossible to get enough statistics for new physics signals. Prescale factors can vary during one run but are constant within one luminosity block.

For the Trigger Combination Method, presented in Chapter 5, it is important to distinguish between the *raw decision* and the *actual physics decision* of a certain trigger. The data is sent to the trigger where the trigger conditions are tested. Events passing the trigger conditions but not the prescale factor, are said to have a raw decision. Events which passed both selections have an actual physics decision. Prescale factors are applied at all three trigger levels. There are two different ways of applying prescale factors: the *deterministic* way of applying a prescale factor  $p$ , is to start at the first event of each run and simply count the events, rejecting  $p - 1$  events and only taking the  $p^{th}$  event. This is done until the end of the run. Applying a deterministic prescaling is easy to implement but gives a systematic uncertainty. Another way is to apply a *non-deterministic* prescale factor, which is an advanced way of applying the prescale factor and gives no systematical uncertainty. An event is accepted with the probability  $1/p$  generated by a pseudo-random number generator. In Figure 3.14, the prescaling at ATLAS is shown. The prescale factor at L1 is applied in a

deterministic way, after the validation of the trigger conditions. Due to the extremely high statistics, the systematical effects are negligible. At the HLT, non-deterministic prescales are applied before testing the trigger conditions. For large amount of data, it makes no difference in statistics whether a prescale is applied before or after validating the trigger condition. Nevertheless, when applying the prescale factor before taking the trigger decision, it saves computing time, since the algorithms need not to be executed.

# Jet Reconstruction and Calibration in ATLAS

This Chapter starts with a description of the showering development of jets. This is followed by the jet reconstruction process and the used reconstruction algorithms in ATLAS. At the end of this Chapter, the two main jet energy scale correction schemes used in ATLAS are discussed.

## 4.1. Jet Reconstruction

ATLAS uses different algorithms to reconstruct jets from calorimeter depositions in the calorimeter but also to reconstruct jets in simulation samples. In order to understand the reconstruction, the showering development of jets at different levels is discussed.

### Jet Levels

The hard scattering process produces quarks and gluons in the final state, but due to the color confinement these partons will hadronize<sup>1</sup> into color neutral hadrons, such as  $\pi^0$  or  $\pi^\pm$ , and form a bunch of collinear particles. The newly formed hadrons, will further decay and deposit their energy in calorimeter cells close to each other. These energy depositions are used to reconstruct jets in order to reveal the underlying hard subprocess. This is possible, since the jet energy is sensitive to the initial parton energy. The jet has three different levels in the showering process shown in Figure 4.1. First the *parton level*, which is the pure outgoing parton after the hard scattering, before any *parton showering* appears due to soft radiation. When the parton hadronizes and produces several new hadrons, it is referred to as *particle level*. On particle level, the jet signal can be influenced by lost soft tracks due to the magnetic field, additional tracks from underlying events or in-time<sup>2</sup> pileup. Finally, there is the *calorimeter level*, when the particles from the hadronization process deposit their energy in the calorimeter cells. The energy measured in the calorimeter cells can be associated with the energy of the original parton, but several effects need to be considered. At calorimeter

<sup>1</sup>One of the best phenomenological descriptions of hadronization is given by the *Lund String Model* [29]. It is also used to model the hadronization process in the Monte Carlo generator Pythia.

<sup>2</sup>In-time pileup refers to pileup events from the same bunch crossing.

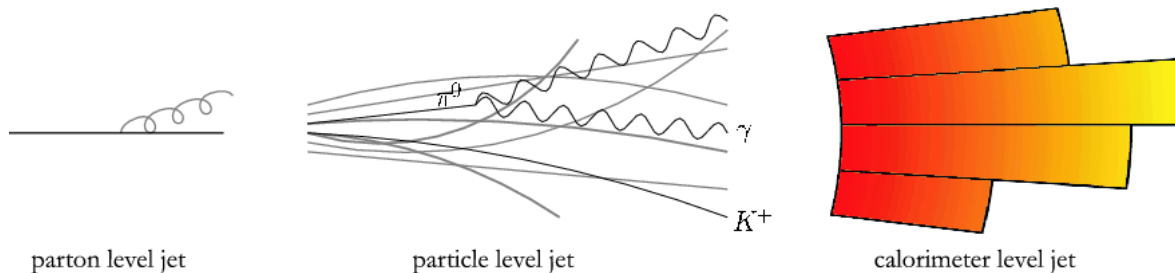


**Figure 4.1.:** These are the three different jet levels in a detector. The parton level, which refers to the bare parton before fragmentation. The particle level addresses the particles which are produced by the hadronization of the original parton and finally, the calorimeter level which refers to the energy depositions in the calorimeter of the particles [30].

level, the measurement of the jet energies is influenced by the non-compensating nature of the calorimeters, energy losses due to passive material, out-of-time<sup>3</sup> pileup events, reconstruction algorithm inefficiencies and electronic noise. To obtain the energy of the original outgoing parton, it is necessary to perform calibration steps on each level of the jet reconstruction.

## Jet Reconstruction Algorithms

As seen in Chapter 2, stable and efficient jet reconstruction algorithms are crucial for many physics analyses. For the measurement of the top mass, an absolute systematical uncertainty of better than 1% is desired and hence, the jet reconstruction algorithms must have properties to provide the possibility of such small uncertainties. The electromagnetic and hadronic calorimeters are the main detector parts to reconstruct jets. The particles deposit their energy in the calorimeter, and this energy depositions are used to combine the calorimeter cells in order to reconstruct jets. The ATLAS calorimeters provide almost full coverage in the pseudorapidity range  $|\eta| < 4.9$ . For many data analyses, jets are needed at different levels and hence have to be reconstructed on all three levels. In order to keep them comparable, the following requirements need to be fulfilled [31]

- **Infrared safety:** The jet reconstruction or the number of reconstructed jets should not be influenced by any soft particle from the parton showering of the original outgoing hard scattered parton.
- **Collinear safety:** When one particle is decaying into two collinear particles, the jet reconstruction should not be influenced by it.
- **Level independence:** On all three levels, parton, particle and calorimeter level, the algorithm should reconstruct corresponding jets and the same underlying hard process.
- **Environment independence:** Stability of the jet reconstruction for different data taking conditions, such as changing instantaneous luminosity, pileup conditions or underlying event activity.

<sup>3</sup>Out-of-time pileup refers to pileup events from other bunch crossings.

- **Detector independence:** The jet reconstruction should not be influenced by the calorimeter region or effects from electronic noise.
- **Boost invariance:** The reconstructed jets should be the same in the lab and the collision frame.
- **Resource saving:** The jet reconstruction should be sufficiently fast and have an acceptable memory usage of the computing resources.

There are several different algorithms to identify and reconstruct jets in a detector like the seeded fixed cone finder, *Seedless Infrared Safe Cone* (SISCone), the  $k_T$  algorithm or the anti- $k_T$  algorithm. Mainly, they can be divided into two types of algorithms: the cone algorithms and the clustering algorithms. The basic concept of cone algorithms is to determine the direction of the dominant energy flow and define the jet as an angular cone around it. The seeded cone algorithms start with the highest  $p_T$  objects, which have passed a certain threshold condition, mark them as seeds and determine the centroid of the objects within a cone with radius  $R$  around the first seed. If the geometric center and the calculated jet center coincide, the jet is regarded as stable and everything is repeated for the next seed. If not, the steps are repeated by choosing the calculated jet center as new cone center and all objects within a new cone of radius  $R$  are taken. This is repeated until the jet is stable according to the mentioned condition. This is done until no seeds are left. One of the main disadvantages is that cone algorithms are neither infrared nor collinear safe. An exception is the SISCone algorithm which is constructed such that it is infrared stable, but for large particle multiplicities it becomes problematic since the total run time is rather long ( $\mathcal{O}(N \cdot 2^N)$ ) [32, 33].

The main reconstruction algorithm in ATLAS is the AntiKt<sup>4</sup> algorithm [34], which is a modification of the  $k_T$  algorithm<sup>5</sup>. Compared to other algorithms it has several advantages. As it will be shown, the AntiKt algorithm is infrared and collinear stable and forms cone-like shaped jets. The used variables to find and reconstruct jets are the distance  $d_{ij}$  between two preclusters  $i$  and  $j$ , and  $d_{iB}$  the distance between a precluster  $i$  and the beamline  $B$ .

The steps of the AntiKt algorithm are:

1. List all so called preclusters, initially consisting of partons, particles or calorimeter towers, dependent on which jet level the reconstruction is executed, and assign the transverse momentum  $k_T$ , azimuthal angle  $\varphi_i$  and the rapidity  $y_i$  to each precluster.
2. For each precluster  $i$  determine the distance between the precluster and the beamline

$$d_{iB} = \frac{1}{k_{Ti}^2}. \quad (4.1)$$

<sup>4</sup>Same as anti- $k_t$  algorithm.

<sup>5</sup>The  $k_T$ , the anti- $k_T$  and the Cambridge/Aachen algorithms are very similar in their reconstruction steps. A generalization of the determination of the distances is given by:  $d_{iB} = k_{Ti}^{2p}$  and  $d_{ij} = \min(k_{Ti}^{2p}, k_{Tj}^{2p}) \frac{\Delta_{ij}^2}{R^2}$ . The  $k_t$  algorithm has  $p = 1$ , the Cambridge/Aachen algorithm is the case with  $p = 0$  and the anti- $k_T$  algorithm has  $p = -1$ .

3. For each pair of preclusters  $(i, j)$  with  $i \neq j$  determine the distance between them

$$d_{ij} = \min \left( \frac{1}{k_{Ti}^2}, \frac{1}{k_{Tj}^2} \right) \frac{\Delta_{ij}^2}{R^2} \quad (4.2)$$

with  $\Delta_{ij}^2 = (y_i - y_j)^2 + (\varphi_i - \varphi_j)^2$ .

4. Determine which of the two distances is the minimum

$$d_{min} = \min (d_{iB}, d_{ij}) \quad (4.3)$$

if

- a)  $d_{min} = d_{ij}$  merge the two preclusters into a new precluster and add the four-vectors, to obtain the new four-vector  $k_{new} = k_i + k_j$ .
- b)  $d_{min} = d_{iB}$  preclusters can not be merged and precluster  $i$  is assigned to be a stable jet. Take the precluster out of the list of preclusters.

5. Repeat everything until no further precluster is left.

This algorithm reconstructs jets which are clustered in a cone with radius  $R$ . In ATLAS, the standard cone sizes  $R = 0.4$  and  $R = 0.6$  are used for data analysis. The main advantages of the AntiKt algorithm is that it still combines close particles first, but soft particles are combined with hard particles before being combined with other soft particles. That makes the algorithm infrared stable. Collinear particles are also clustered first, making the algorithm collinear stable, too. Another advantage is that the shape is more 'cone-like' than for other clustering algorithms. One of the disadvantages is the computing time: for  $N$  particles in an event, between  $N^{3/2}$  and  $N^3$  calculations are necessary, making the algorithm relatively slow.

## 4.2. Jet Energy Calibration

Jets, which are reconstructed from calorimeter depositions, are at the electromagnetic (EM) scale. To obtain the jets at the hadronic scale a calibration has to be applied. Not only jets reconstructed from collision data need a calibration, but also jets reconstructed in simulation samples. In the simulations, detector effects are also implemented and hence, the simulated calorimeter depositions, which are used to reconstruct jets, are also at EM scale. The following calibration description, is explained for calorimeter jets from data but works the same for calorimeter jets from simulation.

The *Jet Energy Scale* (JES) calibration corrects the jet energy, measured in the calorimeter at EM scale, to the right values at hadronic scale [35]. The jet energy measurements are influenced by several effects, which the JES calibration needs to correct for, such as:

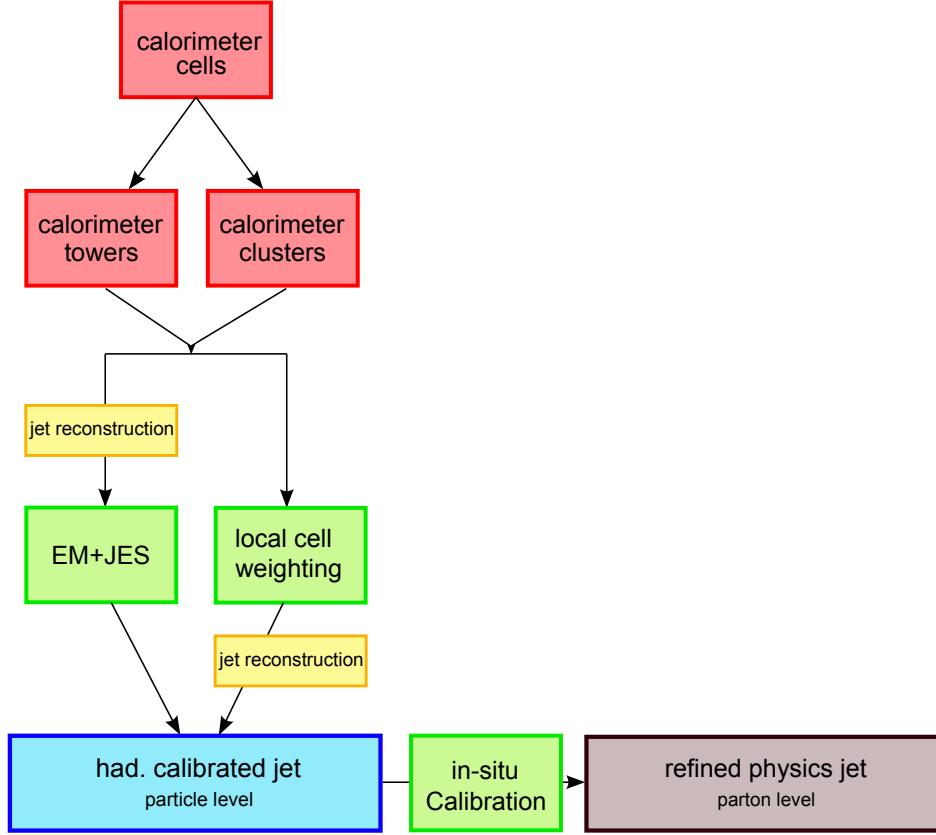


**Figure 4.2.:** A simplified diagram of the two main calibration schemes. Both utilize signals from the calorimeter cells, either in form of towers or clusters. For the EM+JES scheme, the jets are first reconstructed and then calibrated to the hadronic scale, whereas the LCW first calibrates the calorimeter cells and then reconstructs the jets with these calibrated clusters. In the end, the jet at parton level can be obtained with several in-situ measurements. Red denotes the calorimeter level, green the calibration processes, yellow the jet reconstruction, blue the jet at particle level and brown the refined physics jet at parton level.

- the non-compensating nature of the ATLAS calorimeters. Hadronic particles have lower energy responses in the calorimeter, compared to electromagnetic particles with the same energy.
- particles which escape the calorimeter and do not deposit any energy (leakage).
- the passive material in front of the calorimeter which causes energy losses of the particles before they enter the calorimeter.
- energy losses due to the jet reconstruction algorithms and calorimeter clustering.

In ATLAS, there are two main jet calibration schemes, the *EM+JES* and the *Local Cell Weighting* (LCW), both sketched in Figure 4.2. In both methods the calibration constants are determined from simulation and both methods utilize the energy depositions from the calorimeter cells at EM scale. These cells are either grouped into calorimeter towers with a projective fixed 2-dimensional grid size of  $\Delta\eta \times \Delta\varphi = 0.1 \times 0.1$  or 3-dimensional topological

clusters. To build a cluster, seed cells are identified by requiring them to pass a certain signal-to-noise ratio. Then neighboring and perimeter cells are tested iteratively on weaker noise thresholds and merged into topological clusters if they pass the condition. Then it depends which calibration scheme is used. The EM+JES scheme is a relatively simple calibration, applying jet energy and pseudorapidity dependent correction factors to each jet reconstructed at EM scale. The LCW first calibrates the cells of a cluster to the hadronic scale and then reconstructs jets with these calibrated calorimeter clusters. After the calibration to particle level, several in-situ measurements can be used to obtain the jet at parton level, see next chapter.

This thesis utilizes jets calibrated with the EM+JES scheme, the current standard calibration in ATLAS which is described in more detail in the next section. The LCW is a more advanced calibration and it is planned to use it as standard calibration in the future and hence, it is only shortly presented at the end.

## EM+JES Scheme

In the EM+JES scheme, the jet energy at hadronic level is obtained by using corrections from in-situ measurements as well as simulation based calibration constants. Jets are reconstructed before the calibration either using calorimeter towers or calorimeter clusters as input. The calibration scheme itself is divided into three steps: first a pileup correction, second a pseudorapidity correction and third the final energy correction.

The pileup correction is the first step in the calibration process. It is applied to the jet energy measured at EM scale. In-time pileup events can cause additional energy depositions in the reconstructed jets from particles which are not originating from the hard scattering vertex. To account for the additional energy, the average energy deposition in the calorimeter cells from randomly triggered events is determined, as a function of the jet pseudorapidity and the number of primary vertices. This is a good way to estimate the contributions to the jet energy from in-time pileup events. As correction, this average additional energy is subtracted from the measured jet energy. In Figure 4.3, the average energy due to pileup in 2010 is shown as a function of the number of vertices. For four primary vertices in the event, the additional energy is about 1 GeV to 2 GeV, dependent on the transverse momentum of the track of the jet. The jet energy resolution is influenced by less than 1% from pileup.

After the pileup correction, the direction of the jet is corrected to ensure that the jet is originating from the primary vertex. This is necessary, since the jets are reconstructed starting at the geometrical center of the detector instead of at the primary vertex. The primary vertex is defined as the vertex with the highest value for the sum of the squared transverse momenta of the tracks associated with the vertex,  $\sum p_{T,track}^2$ . The new direction, from the primary vertex to the centroid of the jet, is used to recalculate the jet kinematics as the vector sum of the four-momenta of the topological clusters. This correction does not change the jet energy but improves the angular resolution and leads to a small improvement, of less than 1%, of jet transverse momentum response.

The actual calibration constants are derived afterwards from simulation by comparing the kinematics of the reconstructed calorimeter jet with a corresponding truth level jet from

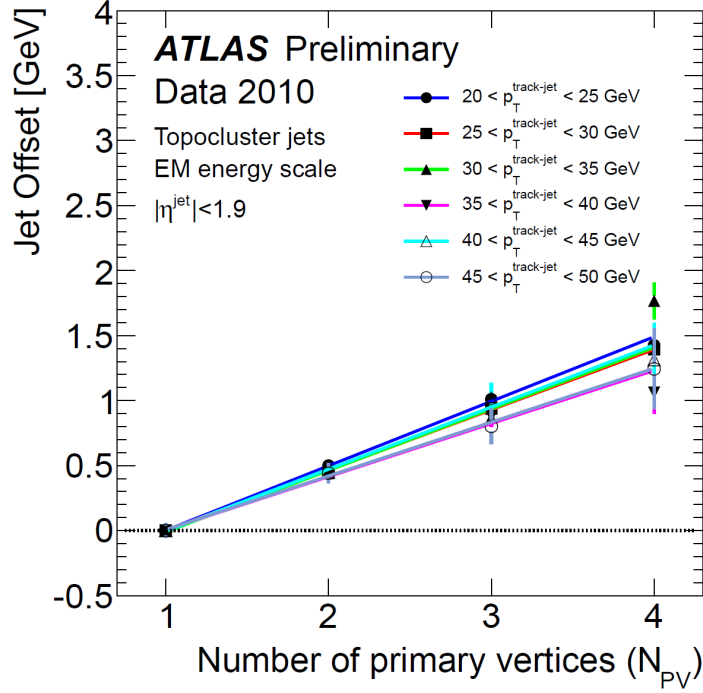


**Figure 4.3.:** The additional energy in the calorimeter due to in-time pileup, as a function of the number of primary vertices [36].

simulation. All isolated<sup>6</sup> calorimeter jets which are successfully matched<sup>7</sup> to an isolated truth jet at particle level from simulation are utilized for the determination of the calibration factors. For each pair of matched calorimeter-truth jets, the response  $\mathcal{R}$  at EM scale is determined in bins of  $E_{truth}$  and  $\eta_{det}$  via

$$\mathcal{R} = \frac{E_{calo}^{EM}}{E_{truth}}. \quad (4.4)$$

The pseudorapidity  $\eta_{det}$  is the uncorrected pseudorapidity value before the origin correction. For each  $(E_{truth}, \eta_{det})$  bin, the  $E_{calo}^{EM}/E_{truth}$  distribution is fitted with a gaussian distribution, and the position of the maximum value of the fit results in the mean jet energy response  $\langle \mathcal{R} \rangle$  in this bin. Furthermore, the average calorimeter jet energy  $\langle E_{calo}^{EM} \rangle$  is also calculated for all bins. Then, for a fixed  $\eta_{det}$  bin  $i$ , the discrete points  $(\langle E_{calo}^{EM} \rangle_k, \langle \mathcal{R} \rangle_k)$  for every  $E_{truth}$  bin  $k$  are fitted with a function

$$\mathcal{C}_{cal,i}(E_{calo}^{EM}) = \sum_{j=0}^N a_j (\ln E_{calo}^{EM})^j \quad (4.5)$$

with  $N \in \{1, \dots, 6\}$ , depending on the accuracy of the fit and the free parameters  $a_j$ . The determined function  $\mathcal{C}_{cal,i}(E_{calo}^{EM})$  describes the jet response as a continuous function of the calorimeter jet energy. A calorimeter jet with a measured energy of  $E_{calo}^{EM}$ , at EM scale, is

<sup>6</sup>An isolated jet has, within a radius of  $2.5R$ , no further jets with  $p_T > 7$  GeV.  $R$  is the radius parameter of the jet reconstruction algorithm.

<sup>7</sup>Successfully matched means the two jets coincide within a radius of  $\Delta R = \sqrt{\Delta\eta^2 + \Delta\phi^2} = 0.3$ .

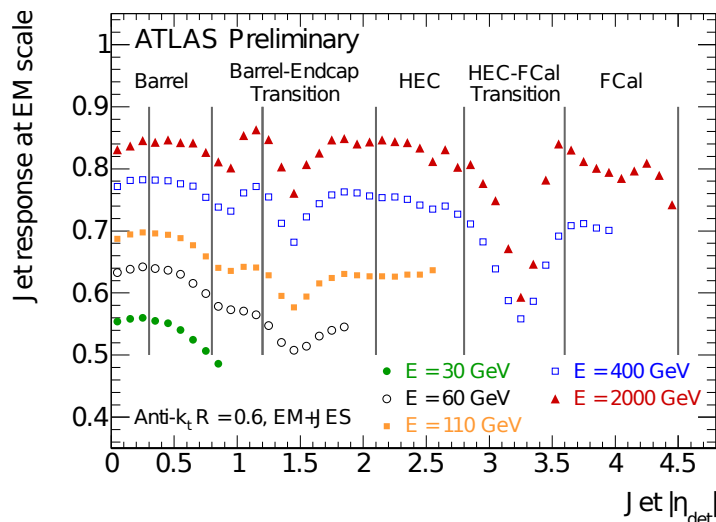


**Figure 4.4.:** 2010 jet energy responses at EM scale from simulation for jets calibrated with the EM+JES scheme. The inverse of the response gives the JES calibration factor [35].

corrected to the hadronic scale via

$$E_{calo}^{EM+JES} = \frac{E_{calo}^{EM}}{\mathcal{C}_{cal}(E_{calo}^{EM})|_{\eta_{det}}} \quad (4.6)$$

with  $\mathcal{C}_{cal}(E_{calo}^{EM})|_{\eta_{det}}$  evaluated at the  $\eta_{det}$  region of the jet. Evaluating the function at a given jet energy (at a fixed  $\eta$  bin) and taking its inverse, gives the calibration constant.

In Figure 4.4, the exemplary jet energy responses at EM scale from simulation are shown for jets calibrated with the EM+JES scheme from 2010<sup>8</sup>. The jet response is different for calorimeter jets with different energy. The inverse of the jet energy response is the calibration constant, e.g. for jet responses of  $\mathcal{R} = 0.5$  the calibration constant is  $c = 2$ . The calibration constants are smaller for high energetic jets in the forward region ( $c \approx 1.2$ ) and are higher for lower energetic jets and jet in the transition region with  $c \approx 2.0$ .

Additionally, another correction of the pseudorapidity is done. The ATLAS calorimeters cover almost the full pseudorapidity range up to  $|\eta| < 4.9$ , but nevertheless crack or transition regions are unavoidable. A jet will have less measured energy in these regions compared to the measured energy in a region well instrumented. Hence, the direction of the jets is biased towards well instrumented detector regions. To correct this bias, for each  $(E_{truth}, \eta_{det})$  bin, an averaged pseudorapidity value  $\Delta\eta = \eta_{truth} - \eta_{reco}$  is determined. This correction of the pseudorapidity value is smaller than  $\Delta\eta < 0.01$  for well instrumented regions and rises in the transition regions up to  $\Delta\eta \approx 0.05$ .

<sup>8</sup>At the day of printing, no official jet calibration results of the ATLAS group was published and hence, jet energy responses from 2010 are depicted here. Qualitatively, there is no difference in 2010 and 2011 jet responses.

### **Local Cell Weighting Scheme**

The second main calibration method, the local cell weighting, only utilizes energy clusters at EM scale. The clusters are classified into EM, hadronic or unknown clusters and a local calibration is done by weighting each cell of the cluster separately. The calibration constants are also determined from simulation and take the different classifications into account since electromagnetic clusters need smaller calibration factors than hadronic clusters. Afterwards, further energy losses due to passive material in front of the calorimeter and out-of-cluster depositions are corrected for. When the clusters are calibrated to this local hadronic scale, the jets are reconstructed using the desired reconstruction algorithm and further corrections are applied, including noise and pileup corrections. In the end, the jets are calibrated to particle level.



# In-situ Jet Calibration

The jet calibration described in the previous Chapter is validated by several *in-situ* studies, based on real data. Beside the validation of the jet energy scale, the in-situ measurements are also used to determine the jet energy scale uncertainty. In this Chapter, some important in-situ methods are presented, especially the standard methods for the jet  $\eta$  intercalibration in ATLAS. The jet pseudorapidity intercalibration is performed to ensure equal calorimeter responses for jets with equal transverse momenta in all pseudorapidity regions. At the end of this Chapter, a new method to select appropriate dijet events, the so called Trigger Combination Method, is presented.

## 5.1. Jet Energy Scale Uncertainty

To validate the *Jet Energy Scale* (JES) correction and its uncertainty, several in-situ measurements can be used. These measurements include

- balancing the transverse momenta of well calibrated objects, like a  $Z$ -boson or a photon ( $\gamma$ ), against the momentum of a jet. This is used for corrections in  $|\eta| < 1.2$ .
- balancing multijets, to estimate the JES uncertainty for jets with large  $p_T$ .
- balancing dijet events, to obtain an equal response over the entire pseudorapidity range.

The uncertainties of all these measurements are combined to the total jet energy scale uncertainty. In 2010, this was done by adding the single contributions in quadrature. In 2011, the combination of the different contributions is more advanced by determining a covariance matrix to take correlations into account. In 2010, the JES uncertainty was 2%-4% for jets in the central region with transverse momenta less than 60 GeV and for higher energetic jets in the range  $60 \text{ GeV} \leq p_T < 800 \text{ GeV}$  slightly smaller with about 2.5%. In the transition region, the JES uncertainty was larger with 7% for jets with momenta  $p_T < 60 \text{ GeV}$  and approximately 3% for jets with higher momenta. The JES uncertainty is largest in the forward region with 13% for jets with momenta  $p_T < 60 \text{ GeV}$  [35]. The JES uncertainty for 2011 is expected to be smaller, but no official results were yet published on the day of printing.

## Balancing $Z/\gamma$ +Jet

For this method, events with one  $Z$ -boson or one photon plus one jet are used and further denoted with  $Z/\gamma$ +jet events. The  $Z$ -boson is reconstructed either via the electron decay  $Z \rightarrow e^+e^-$  or via the muon decay  $Z \rightarrow \mu^+\mu^-$ . The calibration uses transverse momentum balance of a very precisely measured electromagnetic particle against the jet. For events with exactly one jet and one  $Z$ -boson or one  $\gamma$  the transverse momenta of the two-body system are balanced due to momentum conservation. The balance  $B$  is defined as

$$B = \frac{p_T^{jet} - p_T^{Z/\gamma}}{p_T^{Z/\gamma}} \quad (5.1)$$

with  $p_T^{jet}$  the transverse momentum of the jet and  $p_T^{Z/\gamma}$  the momentum of the  $Z$ -boson or  $\gamma$ , respectively. However, this topology is very rare in the detector. It is more likely to have, in addition to the  $Z$ -boson or the  $\gamma$ , several jets in the event. This leads to two different ways to perform the analysis:

- Application of a tight  $\Delta\varphi$  selection between the leading jet and the  $Z/\gamma$  to ensure that they are back-to-back in the  $\varphi$ -plane. Furthermore, additional jets are required to have small transverse momenta, such that their contribution to the momentum balance is negligible. In this case, the balance  $B$  is expected to be zero and deviations give the calibration factors. A disadvantage is that these strong selection criteria decrease the available statistics, but nevertheless this is a very precise way of measuring the momentum of the jet, since the momenta of the  $Z$ -boson and the  $\gamma$  are measured with high accuracy in the detector.
- Events with more than one jet are selected and no selection criteria on the transverse momenta of the jets are applied. Instead, all jets in the event are required to pass a specific quality selection. The sum of all transverse momenta is taken to balance the  $Z$ -boson or  $\gamma$  momentum. The balance  $B_s$  is then defined as:

$$B_s = \frac{|\sum_j \vec{p}_{t,j}| - p_T^{Z/\gamma}}{p_T^{Z/\gamma}} \quad (5.2)$$

with  $j \in \text{jets}$ . This approach gives more statistics than the previous one, but more sophisticated techniques are needed to relate to the energy scale for each jet with the measured balance  $B_s$ .

With these methods the  $\gamma$ +jet calibration has a total uncertainty of less than 1% within  $110 \text{ GeV} < p_T^\gamma < 500 \text{ GeV}$  [37]. The  $Z$ +jet has an uncertainty about 10% at low transverse momenta and for  $p_T^Z > 30 \text{ GeV}$  between 1%-2% [38]. Even though the  $\gamma$ +jet analysis has more statistics, it suffers from large QCD background, especially in the low transverse momentum range. For high transverse momenta, both  $Z/\gamma$ +jet suffer from reduced statistics. Hence, other suitable physics processes are necessary.

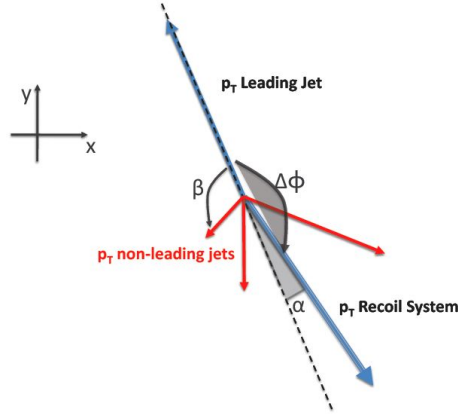


**Figure 5.1.:** Event topology for multijet events. The transverse momentum of the leading jet is balanced to the transverse momentum of the recoil system [39].

## Multijet Technique

For high transverse momenta  $p_T \gtrsim 500$  GeV, QCD multijet events are used to determine the JES uncertainty since the production cross section remains high at high transverse momenta. It is similar to the second method presented for the  $Z/\gamma$ +jet events. The events must have more than two jets and the balance is determined between the transverse momentum of the leading jet<sup>1</sup> and the transverse momentum of the *recoil system*. The transverse momentum of the recoil system is the vectorial sum of all non-leading jets in the event. The topology of a multijet event is shown in Figure 5.1. Furthermore, it is important to ensure that the leading jet has a higher transverse momentum scale compared to the momentum scale of the non-leading jets. This can be achieved by constraining the ratio of the transverse momentum of the second leading jet and the transverse momentum of the recoil system  $\frac{p_T^{second}}{p_T^{recoil}}$ . The balance  $B_{mj}$  is defined as the ratio

$$B_{mj} = \frac{|\vec{p}_t^{leading}|}{|\vec{p}_t^{recoil}|}. \quad (5.3)$$

Ideally, this balance  $B_{mj}$  is expected to be equal to unity, but besides a miscalibration, several sources can influence the balance, such as pileup, soft gluon emission or close-by-jets<sup>2</sup>. The precision on the jet energy scale with this method is about 5% for jets with transverse momenta up to 1 TeV<sup>3</sup>.

<sup>1</sup>The leading jet is defined as the jet with the highest transverse momentum in an event.

<sup>2</sup>Close-by jets are jets where depending on the jet reconstruction algorithm, either one or two jets are reconstructed.

<sup>3</sup>For jets reconstructed with the anti- $k_t$  algorithm and a radius  $R = 0.6$ . For a radius of  $R = 0.4$  the jet energy scale uncertainty is validated within 5% up to 800 GeV.

## 5.2. Standard Methods for Jet Pseudorapidity Intercalibration

The jet pseudorapidity intercalibration is done by balancing dijet events. Two jets which are back-to-back in the  $(x-y)$  plane should have the same momentum going in opposite directions, due to momentum conservation. It would also be possible to use  $Z/\gamma$ +jet events, but the cross section is much lower than for dijet events and especially at high transverse momenta, statistics are an issue. For the same luminosity, the jet pseudorapidity intercalibration achieves higher precision when using the dijet balance method as when balancing  $Z/\gamma$ +jet events due to statistics.

The jet pseudorapidity intercalibration is done in bins of the averaged transverse momentum of the leading and next-to-leading jet,  $p_T^{avg}$ , and in bins of the uncorrected pseudorapidity,  $\eta_{det}$ . There are two standard methods used in ATLAS for the jet pseudorapidity intercalibration: the *Classical Method* (CM) and the *Matrix Method* (MM). The CM has a fixed reference region and all other regions are intercalibrated with respect to this region whereas the MM intercalibrates all regions with respect to each other.

### Classical Method

The Classical Method uses the dijet balance to perform the jet pseudorapidity intercalibration. In a dijet event comprising two back-to-back jets in the azimuthal plane, the transverse momenta of the jets should be equal due to transverse momentum conservation. To assure the  $2 \rightarrow 2$  topology of the event, several selection criteria are necessary. The event selection requires at least two jets in the event, with the  $\Delta\varphi$  angle between the two leading jets to be large enough to ensure that the jets are well separated and back-to-back in the azimuthal plane. Since it is unlikely to have exactly two jets, events with more than two jets are allowed but only when the other jets do not contribute significantly to the dijet balance<sup>4</sup>. In the central region of the detector a reference region,  $-0.8 < \eta_{ref} < 0.8$ , is defined and the other regions are intercalibrated with respect to this reference region. One of the two jets is required to fall within the reference region and is called the *reference jet*, whereas the other jet is called the *probe jet*. In the case that both jets fall in the reference region, they are both used to probe each other. The asymmetry  $\mathcal{A}$  is defined using the measured transverse momenta of the jets:

$$\mathcal{A} = \frac{p_T^{probe} - p_T^{ref}}{p_T^{avg}} \quad (5.4)$$

with  $p_T^{avg} = \frac{1}{2} (p_T^{probe} + p_T^{ref})$ . The asymmetry is determined for each  $p_T^{avg}$  and  $\eta$  bin. This definition of the asymmetry is chosen since it yields a symmetric distribution, contrary to the simple  $\frac{p_T^{probe}}{p_T^{ref}}$  ratio, which is intrinsically asymmetric. When the detector is perfectly intercalibrated this asymmetry is expected to be gaussian distributed with the mean value  $\langle \mathcal{A} \rangle = 0$ . For a non perfect intercalibration the mean value  $\langle \mathcal{A} \rangle$  is shifted. In Figure 5.2, an expected asymmetry distribution is shown when a miscalibration is present. By fitting a gaussian distribution to the dijet asymmetry with the mean value  $\langle \mathcal{A} \rangle$  as a free parameter of

<sup>4</sup>The selection criteria used in the final analysis are described in detail in Chapter 6.

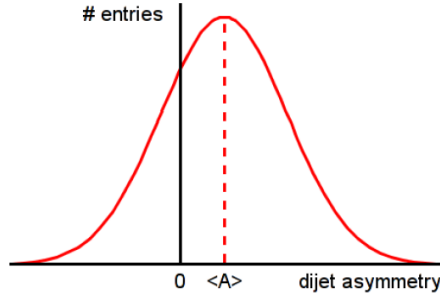


**Figure 5.2.:** An expected dijet asymmetry distribution. The mean value  $\langle \mathcal{A} \rangle$  is shifted around 0, which means there is a miscalibration in the detector.

the fit. With the mean asymmetry value  $\langle \mathcal{A} \rangle$  it is easy to determine the ratio

$$\frac{p_T^{probe}}{p_T^{ref}} \hat{=} \frac{2 + \langle \mathcal{A} \rangle}{2 - \langle \mathcal{A} \rangle} = \frac{1}{c} \quad (5.5)$$

which gives the relative response of the probe jet with respect to the reference jet. The intercalibration constant  $c$  is equal to unity for a correctly intercalibrated detector, otherwise it has a different value. The  $p_T^{avg}$  bins are chosen according to the trigger turn-on curves, described in more detail in the trigger selection section. Each  $p_T^{avg}$  bin extends over the entire pseudorapidity range in separate  $\eta$  bins. The detector geometry determines the  $\eta$  binning and is listed in Table 5.1. The bins are symmetric in positive and negative direction. For the analysis, the uncorrected detector pseudorapidity  $\eta_{det}$  is used. With this binning, the intercalibration constants can be calculated for all  $p_T^{avg}$  bins  $k$  and each probe jet  $\eta$  bin  $i$ . The calibration constants from equation 5.5 become

$$c_{ik} = \frac{2 - \langle \mathcal{A}_{ik} \rangle}{2 + \langle \mathcal{A}_{ik} \rangle}. \quad (5.6)$$

With this intercalibration constants the jet energy scale of the probe jet can be corrected to the jet energy scale of the reference jet. The statistical uncertainty for the asymmetry  $\langle \mathcal{A} \rangle$  of each distribution is

$$\sigma_{\langle \mathcal{A} \rangle} = \frac{RMS}{\sqrt{N}} \quad (5.7)$$

with  $RMS$  being the root-mean-squared and  $N$  being the number of events in a given  $\eta$  and  $p_T^{avg}$  bin. The binning has been chosen such that the statistics in each  $p_T^{avg}$  bin are approximately the same, except for the lowest and highest bins. The lowest  $p_T^{avg}$  bins are filled with events taken by low threshold triggers with large prescale factors leading to less statistics. They are more sensitive to pileup and hence, more events are rejected because of the selection criteria and finally due to the worse jet resolution they have broader asymmetry distributions. For high  $p_T^{avg}$  bins statistics are naturally getting low.

$\eta$ Bin	ATLAS Detector Region
$0.0 <  \eta  \leq 0.3$	Central Barrel
$0.3 <  \eta  \leq 0.8$	
$0.8 <  \eta  \leq 1.2$	Endcap
$1.2 <  \eta  \leq 2.1$	
$2.1 <  \eta  \leq 2.8$	
$2.8 <  \eta  \leq 3.2$	Transition Region (HEC-FCal)
$3.2 <  \eta  \leq 3.6$	Forward Calorimeter
$3.6 <  \eta  \leq 4.5$	

**Table 5.1.:** The pseudorapidity binning used for the analysis. The bins follow the geometry of the ATLAS detector [35].

## Matrix Method

The Matrix Method is currently the primary standard method at ATLAS for  $\eta$  intercalibration. This method also uses dijet balance but it evades the main disadvantage of the Classical Method. In the Classical Method, at least one of the two jets is required to be in the reference region, whereas the Matrix Method abandons this restriction and hence gets more statistics. The difference in the dijet selection is depicted in Figure 5.3. The 'reference' and 'probe' jets are replaced by 'left' and 'right', according to the requirement  $\eta^{left} < \eta^{right}$ . The asymmetry is defined equivalent to Equation 5.4 as

$$\mathcal{A} = \frac{p_T^{left} - p_T^{right}}{p_T^{avg}}. \quad (5.8)$$

The binning for the Matrix Method is similar to the binning of the Classical Method with the  $p_T^{avg}$  bins  $k$  having two different sub-binnings in  $\eta$ : an  $\eta^{left}$  bin  $i$  and an  $\eta^{right}$  bin  $j$ . The ratio of the responses  $\mathcal{R}$ , for a given  $p_T^{avg}$  bin  $k$ , is defined as

$$\frac{p_T^{left}}{p_T^{right}} \cong \frac{2 + \langle \mathcal{A}_{ik} \rangle}{2 - \langle \mathcal{A}_{jk} \rangle} = \frac{c_{jk}}{c_{ik}} = \mathcal{R}_{ijk} \quad (5.9)$$

and determined for all  $p_T^{avg}$  and  $\eta$  bins. Corresponding to the Classical Method, the  $c_{ik}$  and  $c_{jk}$  are the intercalibration constants for the left and right jet, respectively in a given  $p_T^{avg}$  bin  $k$ . The evaluation the relative intercalibration constant for a jet in a given  $p_T^{avg}$  bin  $k$  and an  $\eta$  bin  $i$ , is done by minimizing a matrix  $M$  of linear equations

$$M(c_{1k}, \dots, c_{N_\eta k}) = \sum_{j=2}^{N_\eta} \sum_{i=1}^{j-1} \left( \frac{1}{\Delta \langle \mathcal{R}_{ijk} \rangle} (c_{ik} \langle \mathcal{R}_{ijk} \rangle - c_{jk}) \right)^2 + X(c_{ik}) \quad (5.10)$$

with  $\Delta \langle \mathcal{R}_{ijk} \rangle$ , the statistical uncertainty of  $\langle \mathcal{R}_{ijk} \rangle$ , and  $N_\eta$  the number of pseudorapidity bins. The additional function  $X(c_{ik})$  is given by

$$X(c_{ik}) = K \left( \frac{1}{\underbrace{N_\eta}_{\bar{c}_k}} \sum_{i=1}^{N_\eta} c_{ik} - 1 \right)^2 \quad (5.11)$$

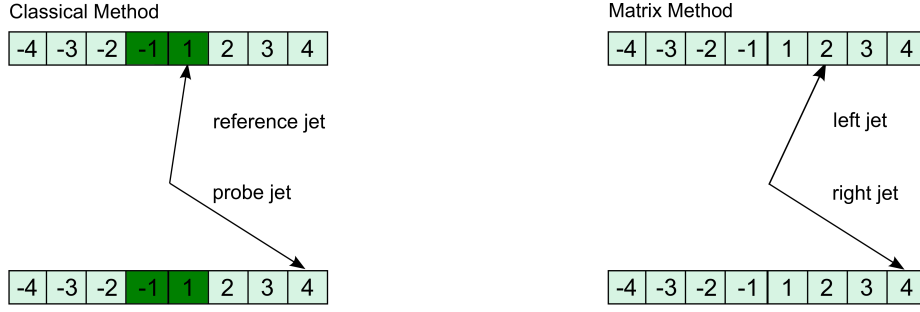


**Figure 5.3.:** The left Figure shows the dijet selection for the Classical Method. One jet is required to be in the reference region (green area), the other jet can be in an arbitrary  $\eta$  bin. The right side depicts the dijet selection for the Matrix Method. There is no reference region, both jets can lie in any  $\eta$  bin.

with a constant  $K$  and  $\overline{c}_k$ , the average calibration constant for a given  $p_T^{avg}$  bin  $k$ . This function  $X(c_{ik})$  is necessary to prohibit the trivial solution of the minimization with  $c_{ik} = 0 \forall i \in N_\eta$  and  $\forall k \in N_{p_T^{avg}}$ . For a perfectly intercalibrated detector all calibration constants  $c_{ik}$  are equal to unity and all mean values  $\langle \mathcal{R}_{ij} \rangle$  are also equal to unity. With this condition, the first term of each linear equation is equal to zero<sup>5</sup> and the second term is also equal to zero since  $\sum_{i=1}^{N_\eta} c_{ik} = N_\eta$ . As expected, for a perfectly intercalibrated detector, the matrix  $M$  vanishes. The trivial solution  $c_{ik} = 0, \forall i, k$  also gives zero for the first term and yields the linear equations to be  $M(c_{1k}, \dots, c_{N_\eta k}) = K$ . By choosing the constant  $K$  sufficiently large,  $K \approx 10^6$ , it is avoided that it becomes a solution of the minimization. Excluding only the trivial solution  $c_{ik} = 0, \forall i, k$  could also lead to a solution where all calibration constants have very small values, which would be equivalent to the trivial solution. Hence, the additional term omits the trivial solution, but does not influence the minimization for real miscalibrations by quadratically suppressing average calibration constants, deviating from unity. The intercalibration constants are calculated for each  $p_T^{avg}$  bin, such that the resulting intercalibration constants  $c_i$  (within a  $p_T^{avg}$  bin) are only dependent on the  $\eta$  value of the jet. These calibration constants  $c_i$ , are additionally scaled in such a way that in the reference region the average correction is equal to unity [3].

## Trigger Selection

The ATLAS single jet triggers are used to select dijet events. The jet triggers have a transverse energy condition. For example, a jet is required to have a transverse energy  $E_T > 20$  GeV to be accepted by the EF\_j20\_a4tc\_EFFS<sup>7</sup> trigger. The trigger efficiency for the online energy is a pure  $\theta$  function, jumping from 0 to 1 at 20 GeV. Due to the fact that offline and online energy are not the same, the trigger efficiency for offline energies is not a pure  $\theta$ -function but has a softened edge. In this rising part the trigger is not fully efficient<sup>8</sup>. In Figure 5.4 the trigger efficiencies for seven 'combined triggers' as a function of  $p_T^{avg}$  are shown. 'Combined'

<sup>5</sup>For sufficient small statistical uncertainties.

<sup>7</sup>Name convention: EF stands for Event Filter, j\* gives the  $E_T$  threshold, a4tc stands for AntiKt4 jet algorithm using topological clusters as input and EFFS denotes that it was a so called full scan mode.

<sup>8</sup>For this analysis a trigger is called fully efficient when it is at its 99% efficiency level.

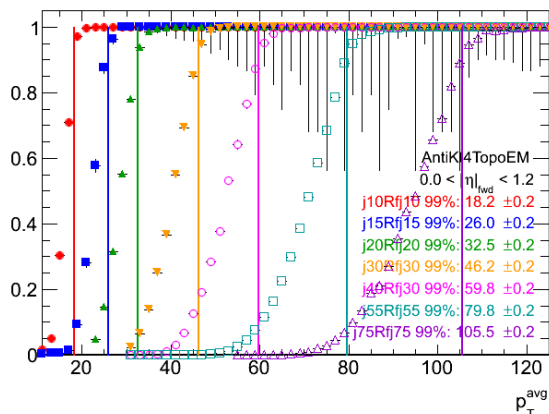


**Figure 5.4.:** The Figure shows jet trigger efficiencies<sup>6</sup> for seven different triggers, always combined with the logical OR, e.g. if the central trigger j10 OR the forward trigger fj10 have selected the event. Additionally, the 99% efficiency point is given. The  $p_T^{avg}$  bins are chosen accordingly to the fully efficient ranges of the triggers [40].

here implies a logical OR between the central and the corresponding forward trigger. The  $p_T^{avg}$  bins for the jet intercalibration are chosen such that the efficiency of the combination, central OR forward trigger, is fully efficient. It is necessary to use the combined trigger efficiency, since the standard methods also use this combined trigger condition: it is always required that either the central OR the corresponding forward trigger must have selected the event. Hence, it must be ensured that the combination of the two triggers is fully efficient in that  $p_T^{avg}$  bin.

As described in Chapter 3, higher threshold triggers have a lower prescale factor. Due to this lower prescale factor it would be desirable to use a higher threshold trigger since it would provide more statistics. In Figure 5.5 the dijet asymmetry distribution for a jet trigger with  $E_T > 30$  GeV is shown. The data, recorded with ATLAS in 2011, corresponds to an integrated luminosity of  $\mathcal{L} = 4.55 \text{ fb}^{-1}$ . A central  $\eta$  bin was chosen  $1.2 < \eta \leq 2.1$  and the  $p_T^{avg}$  bin is  $40 \text{ GeV} \leq p_T^{avg} < 55 \text{ GeV}$ . The shown trigger is not fully efficient in the  $p_T^{avg}$  bin and the shape is clearly not gaussian. Instead, a double peak structure is recognizable. This can be understood since it is more likely that a trigger selects a higher-energetic jet, biasing the dijet asymmetry distribution. From Equation 5.4 one can see that the left peak is dominated by jets originating from events where the reference jet has a higher  $p_T$ , whereas the right peak arises from events where the probe jet has a higher  $p_T$ . This double peak structure is not desirable, since it is not possible to determine the correct intercalibration constants from such a case. To avoid this bias, only fully efficient triggers in a given  $p_T$  range are used for the standard methods.

In Table 5.2, the  $p_T^{avg}$  binning for 2011 and the AntiKt4 algorithm is listed as well as the fully efficient central and forward triggers in that bin. The lowest  $p_T^{avg}$  bin is chosen the way that the combination of the lowest threshold triggers EF\_j10\_a4tc\_EFFS OR EF\_fj10\_a4tc\_EFFS is fully efficient in that  $p_T$  range. Hence, one can assure that only fully efficient triggers are used in each bin.

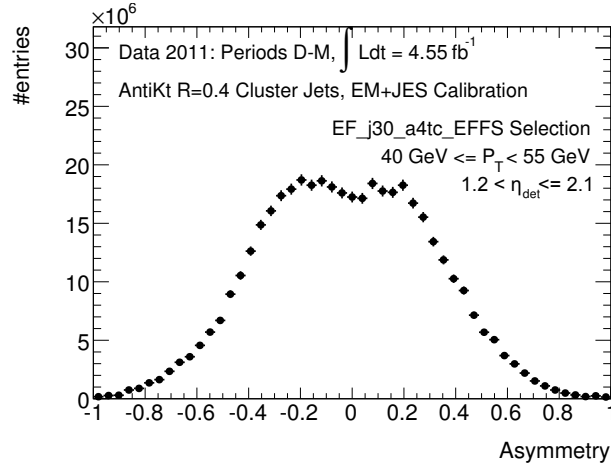


**Figure 5.5.:** The dijet asymmetry for a not fully efficient trigger in the  $p_T^{avg}$  bin  $40 \text{ GeV} \leq p_T^{avg} < 55 \text{ GeV}$  and a central  $\eta$  bin  $1.2 < \eta \leq 2.1$ . The shown trigger is the EF\_j30.a4tc.EFFS which reaches its efficiency plateau at around 55 GeV.

As shown, the use of triggers which are not fully efficient in a given  $p_T^{avg}$  range, bias the dijet asymmetry distribution. The standard methods avoid this problem by only using fully efficient triggers and hence are statistically limited. A different solution to this problem is provided by the Trigger Combination Method which utilizes significantly more statistics.

$p_T^{avg}$ [GeV]	central trigger	forward trigger
22 - 30	j10	fj10
30 - 40	j15	fj15
40 - 55	j20	fj20
55 - 75	j30	fj30
75 - 100	j40	fj30
100 - 130	j55	fj55
130 - 170	j75	fj75
170 - 220	j100	fj100
220 - 300	j135	fj100
300 - 400	j180	fj100
400 - 600	j240	fj100
600 - 800	j240	fj100
800 - 1000	j240	fj100
1000 - 1500	j240	fj100

**Table 5.2.:** Used  $p_T$  bins in 2011 and for the AntiKt4 algorithm with the highest fully efficient central and forward trigger in each  $p_T$  range. For a better readability the triggers are abbreviated (EF\_\*.a4tc.EFFS).

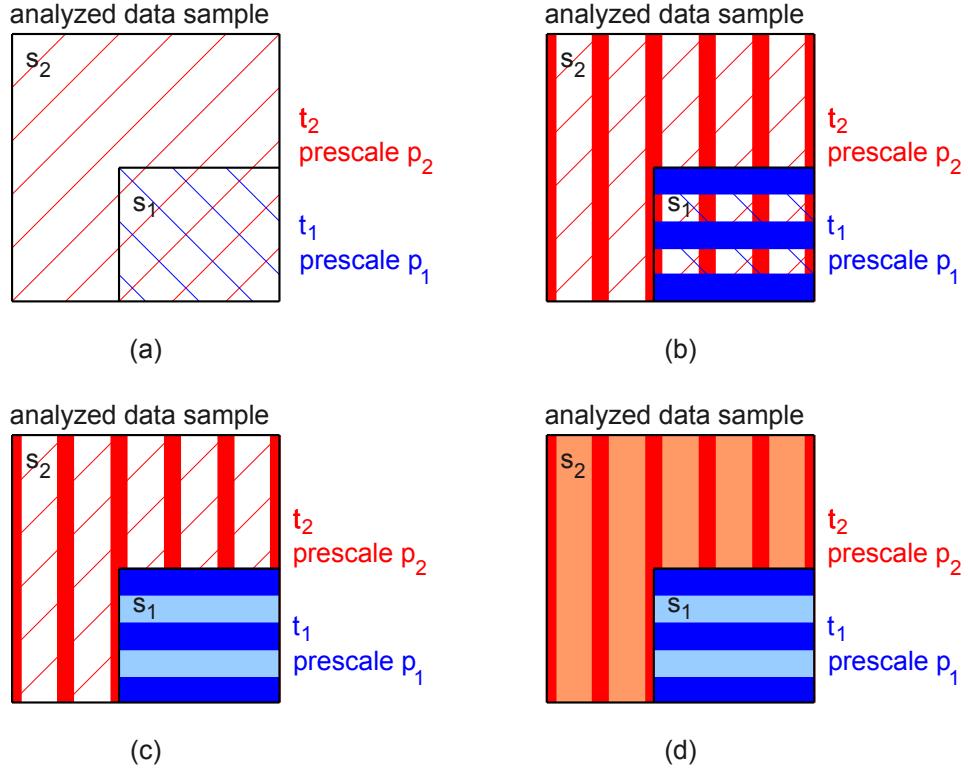


Figure 5.6.: A simple example to reconstruct a given data sample.

### 5.3. Trigger Combination Method

Another approach to solve the problem of not fully efficient triggers in a given range, is using the *Trigger Combination Method* (TCM) [41]. In this method, many, not necessarily fully efficient, triggers are combined such that they compose a fully efficient set of triggers. The TCM, as a new way of selecting appropriate dijet events, is studied by using the Classical Method as analysis. It is also possible to apply the TCM to the Matrix Method, to gain even more statistics. For this thesis the so called *exclusion method* is used.

To introduce the TCM, it is first explained using a simplified example shown in Figure 5.6. A given data sample is supposed to be reconstructed using the Trigger Combination Method. There are two triggers, a fully efficient trigger  $t_2$  which collects the entire sample  $s_2$  with a prescale factor  $p_2$ . The second trigger  $t_1$  is a not fully efficient trigger with a prescale factor  $p_1$  and it collects only a subsample  $s_1 \subset s_2$ . In Figure 5.6 (a), the entire data sample is shown. The hatched areas represent the raw decisions of the triggers - red for the fully efficient trigger  $t_2$  and blue for the non fully efficient trigger  $t_1$ . Figure 5.6 (b) indicates besides the raw decision (hatched area) also the actual physics decisions (solid bars). The

two different prescale factors satisfy the condition  $p_2(t_2) > p_1(t_1)$ . For the event selection the lowest prescaled trigger  $t_1$  is checked for an actual physics decision. If it has an actual physics decision, the event is weighted with the prescale factor and kept. Taking all the events, which are selected by the lowest prescaled trigger and multiplied with the correct weight, return the entire subsample  $s_1$ . This is shown in Figure 5.6 (c). To reconstruct the missing ( $s_2 - s_1$ ) area, Figure 5.6 (d), the actual physics decision of trigger  $t_2$  is checked, but it has to be outside the blue area to avoid double counting of the subsample  $s_1$ . Hence the requirement that  $t_1$  must not have a raw decision is necessary. When the event fulfills these requirements, it is weighted with the prescale and kept. After taking all events which fulfill the criteria, the missing area is reconstructed and the complete data sample, represented by the rectangle, is reconstructed without double counting any events.

The previous simple example with only two triggers can be generalized, to an arbitrary number of triggers  $t_1, t_2, \dots, t_n$ , with  $n \in \mathbb{N}$ . It has to be ensured, that the combination of all triggers yields full efficiency, but each single trigger has not necessarily to be fully efficient. Each trigger has a prescale factor  $p(t_1), p(t_2), \dots, p(t_n)$  and it is assumed that the triggers are sorted with respect to their prescales, so that  $p(t_1) < p(t_2) < \dots < p(t_n)$ . For each trigger  $i$ , a weight  $w_i$  can be determined, which is a function of its prescale  $p_i$ . The event selection starts with validating whether the lowest prescaled trigger  $t_1$  has selected the event. If it has selected the event, it is taken and weighted with the corresponding weight  $w_1$ . If the lowest prescaled trigger, in this case  $t_1$ , did not select the event, the next lowest prescaled trigger  $t_2$  is checked. In case  $t_2$  successfully accepted the event, it has to be validated that the previous trigger  $t_1$ , has no positive raw decision. Only if both requirements are fulfilled, the event is taken and weighted with the weight  $w_2$ . This procedure is reapplied for all triggers, always checking for an actual physics decision of the next lowest prescaled trigger together with the requirement that all the triggers with lower prescale factors have no raw decisions. This is necessary to avoid double counting of events. After applying this method to the entire data set, the number of the accepted events is maximized, due to an optimal utilization of the triggers and their prescale factors.

The weight  $w_i$  for a given trigger  $t_i$  is defined as

$$w_i := \frac{N_{orig}}{N} \quad (5.12)$$

with  $N_{orig}$  the number of events accepted by a trigger without any prescale factor applied and  $N$  the number of events accepted by the trigger with the prescale factor applied. In case the prescale factor is constant within a luminosity block, the weight is just the prescale factor itself. In case of changing prescale factors within a luminosity blocks, the weight  $w$  for each trigger is not only the prescale of the trigger. The ratio can be expanded with the total cross section  $\sigma$  of the triggered process:

$$w_i = \frac{N_{orig}/\sigma}{N/\sigma}. \quad (5.13)$$

This can be rewritten as:

$$w_i = \frac{\sum_k \mathcal{L}_k}{\sum_k \frac{\mathcal{L}_k}{p_k(t_i)}} = \frac{\sum_k \mathcal{L}_k}{\int \mathcal{L}} \quad (5.14)$$

with  $k$  running over all luminosity blocks. For the second equation the relation  $\int \mathcal{L} = \sum_k \frac{\mathcal{L}_k}{p_k(t_i)}$  was used. This simplifies the determination of the weights by using the integrated luminosity collected by each trigger.

The statistical uncertainty on the original number of events  $N_{orig}$  when  $N$  events are taken by the TCM is given by:

$$\delta N_{orig} = \sqrt{\sum_{i=1}^N w_i^2}. \quad (5.15)$$

The statistical uncertainty  $\delta N_{orig}$  is minimal when using averaged event weights, since the sum of the squared weights is minimal for equal weights. This method can be applied to the Classical Method as well as to the Matrix Method, since it is a new way to select the events and does not change the Intercalibration method itself. For this thesis the TCM is only applied to the Classical Method. The systematical uncertainty can be neglected for non-deterministic prescaling procedures, such as the HLT trigger at ATLAS. The L1 trigger has a deterministic prescaling, but due to the extremely high statistics it can also be neglected. If  $t_i$  is a trigger chain, the raw decision has to be checked for all trigger levels.

# Jet Pseudorapidity Intercalibration with 2011 Data

This Chapter provides a detailed analysis of the jet pseudorapidity intercalibration with 2011 data using the trigger combination method. First, the event selection for data and simulation is described. This is followed by studying which jet triggers contribute to the event selection in different bins. Then the achieved calorimeter responses are presented and compared to results from simulation as well as to results from the Classical and Matrix Method. Finally, a study to estimate the systematical uncertainty of the Trigger Combination Method is presented. Calorimeter responses are also determined for 2010 and 2012 ATLAS data and can be found in Appendix A and Appendix C, respectively. The analysis is described using 2011 data, since this permits a direct comparison with the official ATLAS results. In 2011, the main reconstruction algorithm is AntiKt with the distance parameter  $R = 0.4$  and hence, it is used in this Chapter. The analysis was also performed using  $R = 0.6$  as distance parameter. This results can be found in Appendix B.

In this Chapter, CM refers to the analysis of the Classical Method, with the standard trigger selection, TCM refers to the analysis of the Classical Method but using the Trigger Combination Method for selecting the events. MM refers to the Matrix Method analysis using the standard trigger selection.

## 6.1. Dijet Selection

For the jet pseudorapidity intercalibration, dijet events are needed. To select appropriate events, several criteria need to be fulfilled including requirements on the quality of the jet reconstruction, the relative position of the jets to each other, the detector region, where the jets lie in or on general detector conditions.

### Preselection

The analysis is performed on 2011 ATLAS data, corresponding to an integrated luminosity of  $4.55 \text{ fb}^{-1}$ . Simulations from two different Monte Carlo generators, Pythia and Herwig++, are used as references. To select events which have dijet topologies, a preselection and several selection criteria are necessary. The preselection includes a Good Run List (GRL) selection

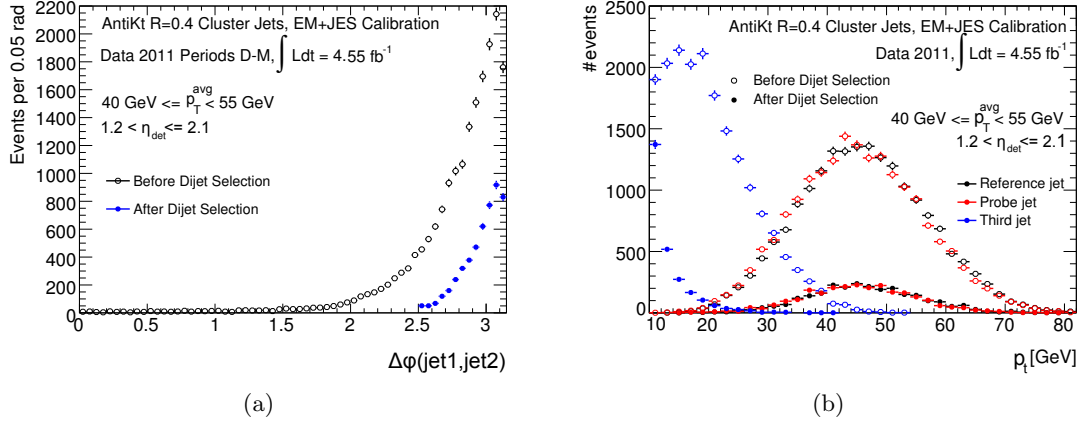


**Figure 6.1.:** 6.1(a) Shows the  $\Delta\phi(\text{jet}_1, \text{jet}_2)$  distribution before (open circles) and after the selection is shown (blue dots). The requirement ensures the jets to be back-to-back in the  $\varphi$ -plane. 6.1(b) The  $p_T$  distributions for the reference and probe jet as well as for the third jet.

to ensure that the entire detector and all subsystems were working properly. Furthermore, at least one good primary vertex, with a minimum of five associated tracks, is required as a sanity check to guarantee a hard scattering event. At least two jets must be in the event and the jets have to pass so called cleaning requirements to reject not well reconstructed jets and jets which are originating from detector noise, LHC beam conditions or cosmic-ray showers. Additionally, in 2011 some cells of the LAr calorimeter at ATLAS were not working properly and hence a requirement is set, to ensure that the jets in an event do not lie within this region.

## Data

Additional selection requirements are necessary to assure only events with dijet topologies. To guarantee that only back-to-back events are taken, a minimum azimuthal separation of the leading and next-to-leading jet is required to be:

$$\Delta\phi(\text{jet}_1, \text{jet}_2) > 2.5. \quad (6.1)$$

In Figure 6.1(a) the  $\Delta\phi(\text{jet}_1, \text{jet}_2)$  distribution is shown for events before and after the dijet selection. The  $p_T$  bin  $40 \text{ GeV} \leq p_T^{avg} < 55 \text{ GeV}$  and a central pseudorapidity bin,  $1.2 < \eta_{det} \leq 2.1$  are shown. The open circles denote jets before the dijet selection and it is evident that there are hardly any dijet events jets with  $\Delta\phi(\text{jet}_1, \text{jet}_2) < 1.5$ , which means the two leading jets are almost never in the same direction. The blue circles are dijet events after the dijet selection. The  $\Delta\phi(\text{jet}_1, \text{jet}_2)$  requirement from Equation 6.1 is clearly visible and was optimized to accept mostly back-to-back events and reduce activity from pileup or underlying events on one hand and enough statistics on the other. Furthermore, selection criteria on additional jets are required to suppress soft radiation, e.g. that extra jets do not contribute significantly to the dijet balance. In order to ensure that additional jets originate from the hard interaction vertex, the *Jet Vertex Fraction* (JVF) for each jet is determined. It is defined as the summed

transverse momentum of all tracks associated with a given vertex, divided by the summed transverse momentum matched to the probed jet [42]. The JVF has large values when the jet originates from a given vertex. The selection requires the third jet to have at least a JVF value of 0.6. Furthermore, the fraction of the transverse momentum of the third jet with respect to the average transverse momentum of the two leading jets is required to be smaller than a given value. Since no tracking is available in the forward region  $|\eta_{det}| > 2.5$  and hence no JVF values are available, the requirements for central and forward jets are different. Central third jets must have transverse momenta less than 25% of the average momentum of the two leading jets and at least 12 GeV. Forward jets are required to have a transverse momentum less than 20% of the average momentum of the two leading jets,  $p_T^{avg}$ , and at least 10 GeV. The impact of the selection requirements on the third jet, can be seen in Figure 6.1(b) where the  $p_T$  distributions for the first three jets before and after the dijet selection are shown. Before the dijet selection, the reference and probe jet distributions have gaussian shape, with the maximum in the center of the  $p_T^{avg}$  bin. The third jet is clearly shifted to lower  $p_T$  values and has a long tail to higher  $p_T$ . It overlaps in the tail with the distributions of the reference and probe jets. After applying the dijet topology selection, the reference and probe jet  $p_T^{avg}$  distribution is still gaussian, with the maximum in the middle of the  $p_T^{avg}$  bin, only count less events. The  $p_T^{avg}$  distribution of the third jet shows that the selection requirement successfully suppresses third jets with high transverse momentum resulting in the desired dijet topology.

## Simulation

To validate the results from the TCM, the same analysis with simulated samples was performed. Simulated events from two Monte Carlo generators, Pythia and Herwig++, are used. The same selection criteria required on data are applied and in addition, requirements on the simulation quality are set. The condition requires the ratios  $r_1 = \frac{\text{truth } p_T}{\text{parton } p_T}$  and  $r_2 = \frac{\text{reconstructed } p_T}{\text{truth } p_T}$  to be within  $0.6 < r_{1,2} < 1.6$ , mainly to remove pileup events. Due to the splitting of the simulation samples in subsamples with different cross sections, the different subsamples have to be weighted differently. The subsample weight is defined as

$$w_{sim} = \frac{\text{Cross section}}{\#\text{Events}}. \quad (6.2)$$

Since no direct shape comparisons between simulation and data are done, the simulation samples are not normalized to the integrated luminosity of the data.

## Trigger and Trigger Emulation

For this study eighteen jet trigger chains with different threshold and pseudorapidity conditions are used: eleven central triggers and seven forward triggers. In Table 6.1 a complete list of the used trigger chains, including their integrated luminosities and corresponding weights is given. The random trigger, as the name indicates, does not check any transverse energy condition but selects random events. As mentioned in the previous Chapter, in case of trigger

EF_*_a4tc_EFFS	L2_*	L1_*	$\int \mathcal{L} [\mu\text{b}^{-1}]$	Weight
j240	j95	J75	$4.55 \cdot 10^9$	1.0
j180	j95	J75	$1.22 \cdot 10^9$	3.7
j135	j95	J75	$1.61 \cdot 10^8$	28.3
j100	j95	J75	$1.86 \cdot 10^7$	244.5
j75	j70	J50	$5.40 \cdot 10^6$	843.3
j55	j50	J30	$1.48 \cdot 10^6$	3068.8
j40	j35	J15	$4.18 \cdot 10^5$	10891.5
j30	j25	J10	$3.47 \cdot 10^5$	13117.6
j20	rdm	rdm	$2.49 \cdot 10^5$	146224.8
j15	rdm	rdm	$8.12 \cdot 10^4$	448469.6
j10	rdm	rdm	$1.82 \cdot 10^4$	1997839.2
fj100	fj95	FJ75	$4.55 \cdot 10^9$	1.0
fj75	fj70	FJ50	$6.92 \cdot 10^8$	6.6
fj55	fj50	FJ30	$5.90 \cdot 10^7$	77.1
fj30	fj25	FJ10	$3.60 \cdot 10^6$	1263.7
fj20	rdm	rdm	$3.97 \cdot 10^5$	91600.0
fj15	rdm	rdm	$3.19 \cdot 10^5$	114168.0
fj10	rdm	rdm	$9.59 \cdot 10^4$	379448.0

**Table 6.1.:** The table shows the trigger chains in 2011 which were used in this analysis. The total integrated luminosity as well as the weight for the TCM is listed, sorted with respect to the weight.

chains, the raw and actual decisions for the TCM have to be checked at each level. The ATLAS trigger system, described in detail in Chapter 3, uses three levels: L1, L2 and the EF. Unfortunately, due to the limited storage volume for data, not all trigger information can be kept and stored. In particular, an L2 object does not exist if L1 passed the raw criteria but not the actual physics criteria. The raw decisions for L1 and EF are emulated for the analysis by checking two conditions. First, if the transverse online energy is above a certain trigger threshold and second, if the online pseudorapidity (not corrected) is central,  $|\eta_{det}| \leq 2.3$ , or forward,  $|\eta_{det}| \geq 2.3$ , to decide if it is a central or forward trigger, respectively. The emulation of L1 and EF is used to ensure that the raw decision is checked in terms of the method. L2 is very difficult to emulate due to the limited availability of L2 objects. A possible emulation of the L2 decision needs to first validate if L2 objects are available (equivalent to L1 passing the actual decision). For available L2 objects, the previous emulation can be applied, otherwise L2 trigger efficiencies can be used to determine a probability if the object would have passed the conditions. Nevertheless, a systematical uncertainty has to be assigned as well, since L1 objects would be used for the emulation of the L2 decision. Another possibility is to rerun the complete L1, L2 and EF algorithms and store the necessary information. This is a more precise way compared to the emulation, but also a lot more storage space and run time are needed. Both ways are too extensive within the framework of this thesis and the systematical studies at the end of this Chapter, have shown that the negligence of the L2 emulation contributes only little to the total systematical uncertainty.

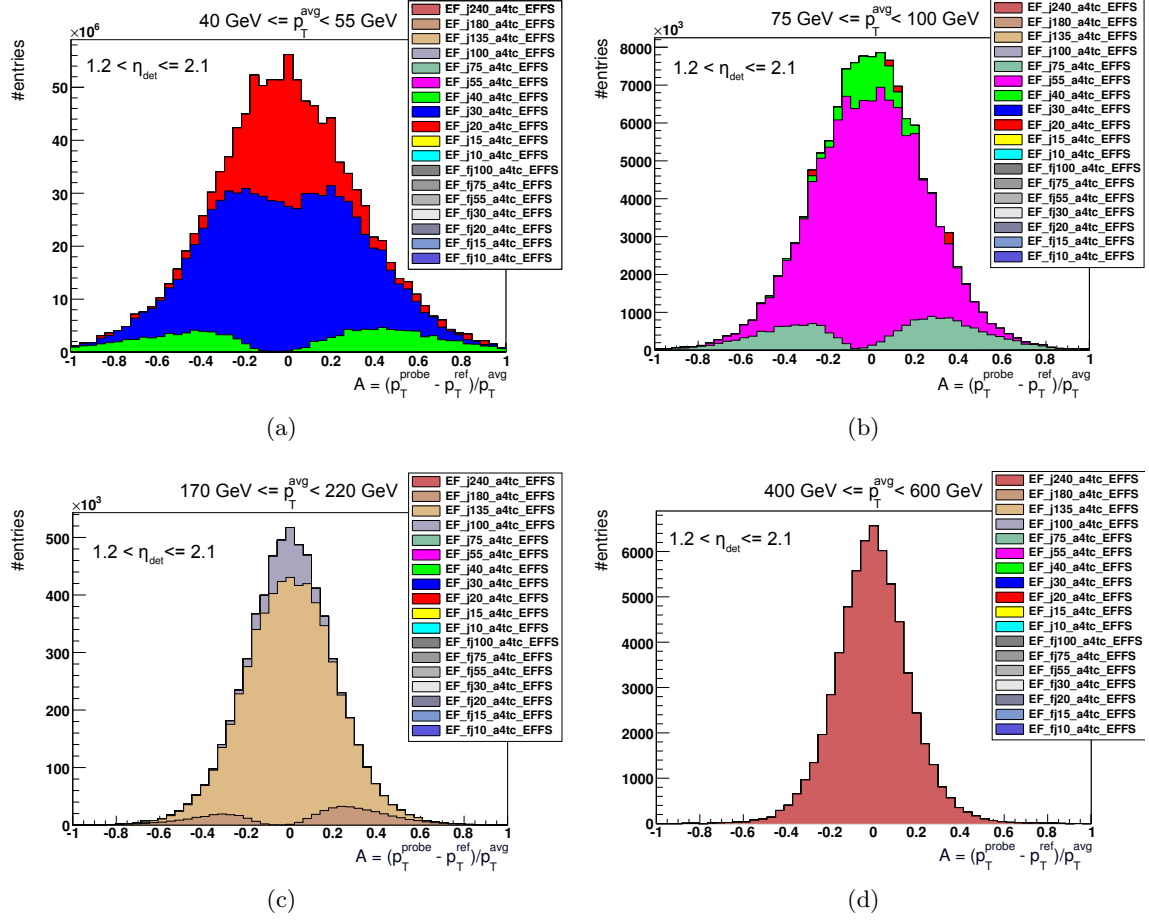


**Figure 6.2.:** Dijet asymmetries for a central  $\eta_{\text{det}}$  bin,  $1.2 < \eta_{\text{det}} \leq 2.1$  and four different  $p_T^{\text{avg}}$  bins. Eighteen different triggers have been used for the analysis.

## Trigger Contributions

In this Section the asymmetry distributions for several different bins are studied, with a focus on the several different triggers, which are selecting events when using the TCM. Furthermore, the statistical differences between the TCM and the CM are discussed.

### Central Region

When using so many different jet trigger chains it is interesting to see the contributions from different trigger chains, which have selected the events. These contributions are studied using the asymmetry distributions for different bins. This is shown in Figure 6.2 for a central  $\eta_{\text{det}}$  bin,  $1.2 < \eta_{\text{det}} \leq 2.1$ , and four different  $p_T^{\text{avg}}$  bins, one bin in the low momentum region,  $40 \text{ GeV} \leq p_T^{\text{avg}} < 55 \text{ GeV}$ , two bins in the medium high momentum region,  $75 \text{ GeV} \leq p_T^{\text{avg}} < 100 \text{ GeV}$  and  $170 \text{ GeV} \leq p_T^{\text{avg}} < 220 \text{ GeV}$ , and one bin in the high momentum region,  $400 \text{ GeV} \leq$

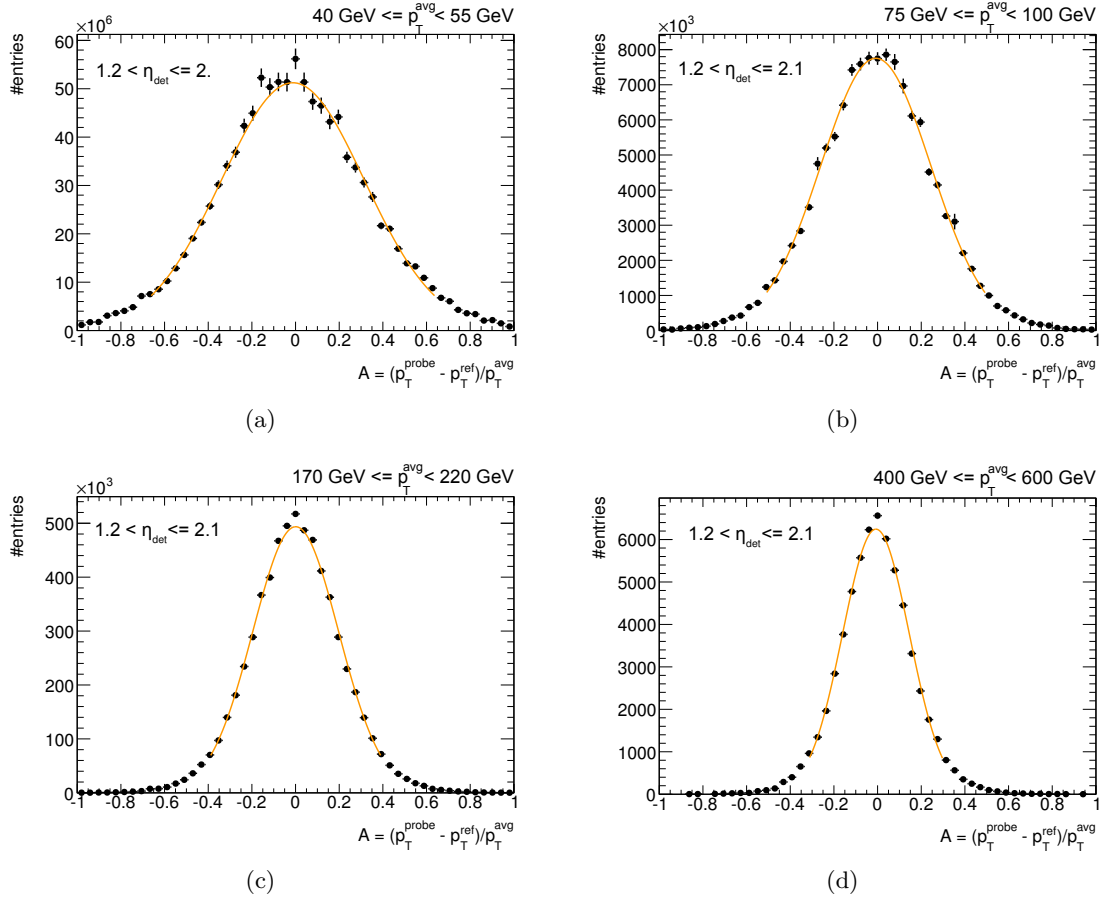


**Figure 6.3.:** Dijet asymmetry for a central  $\eta_{det}$  bin,  $1.2 < \eta_{det} \leq 2.1$  and four different  $p_T^{avg}$  bins. The asymmetry distributions are fitted with a gauss function.

$p_T^{avg} < 600$  GeV. On the right side of each Figure the single jet triggers are listed with the color code. In Figure 6.2(a), the lowest shown  $p_T^{avg}$  bin, three different triggers contribute dominantly to the asymmetry, the j40<sup>1</sup> (green), j30 (blue) and the fully efficient j20 (red). The efficiency curve of the j40 trigger barely started rising and is far away from being on its plateau, hence its contribution is very small and a clear double peak structure is recognizable. The j30 is also not fully efficient in that  $p_T^{avg}$  bin and also shows a double peak structure. This contribution was already shown in Figure 5.5, as the asymmetry distribution for a not fully efficient trigger in a given  $p_T^{avg}$  bin. Compared to the j40, the j30 is closer to its plateau and hence contributes more events to the distribution. The rest of the data was taken by the j20, which is fully efficient in that  $p_T^{avg}$  bin. All together add up to a gaussian distribution. The next highest  $p_T^{avg}$  bin,  $75 \text{ GeV} \leq p_T < 100 \text{ GeV}$ , is depicted in Figure 6.2(b). The contributing triggers are j75 (light green), j55 (cyan), j40 (dark green) and tiny contributions from j20 (red), but no contributions from j30. This is surprising, since already the j40 is fully efficient and should provide the fully efficient trigger. If the two jets have very different energies, e.g. one with high and one with low energy, it might be that the low energy jet was taken by the j20 trigger. Nevertheless, this argument holds only for contributions with large asymmetry

<sup>1</sup>Abbreviated form for EF\_j40\_a4tc\_EFFS.

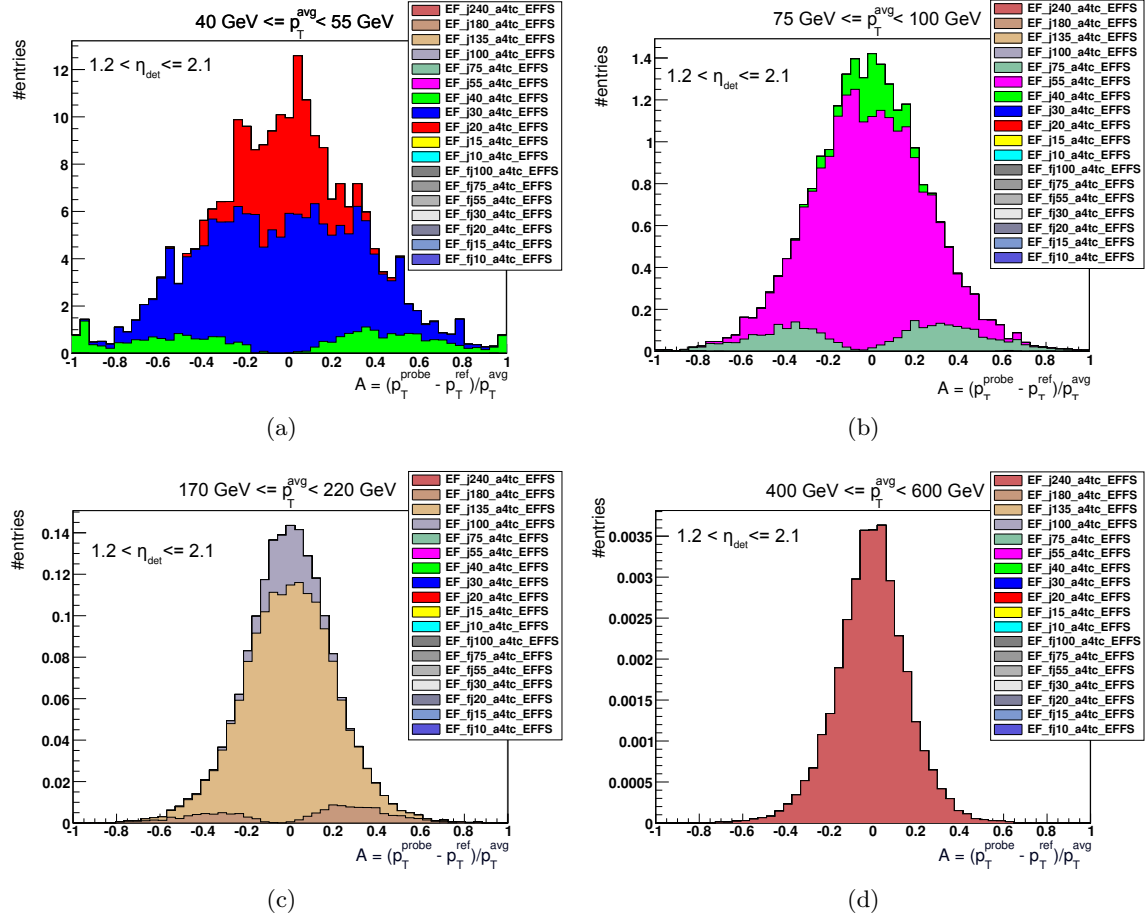


**Figure 6.4.:** Contributions from different trigger to the dijet asymmetry for the Pythia simulation. The expected contributing triggers from simulation agree well with the contributing triggers in corresponding data bins.

values. All pseudorapidity bins for the  $p_T^{avg}$  bin show the same behavior, but no other  $p_T^{avg}$  bin shows this surprising contribution. Hence it is assumed, that it is not a systematical bias in the method. It seems to be small statistical fluctuations, which are not influencing the dijet asymmetry and hence can be neglected. Figure 6.2(c) shows the  $170 \text{ GeV} \leq p_T < 220 \text{ GeV}$  and the three contributing triggers are j180 (grey), j135 (light brown) and the fully efficient trigger j100 (dark brown). In the last Figure 6.2(d),  $p_T^{avg}$  bin  $400 \text{ GeV} \leq p_T < 600 \text{ GeV}$ , only the highest threshold trigger j240 (orange) contributes, because it is fully efficient in that  $p_T^{avg}$  bin. Overall, all the fully efficient triggers and the according  $p_T^{avg}$  ranges are in good agreement with the Table 6.1.

The calibration constants are determined from the asymmetry distributions, by fitting a gaussian distribution to the data and  $\langle \mathcal{A} \rangle$  being a free parameter of the fit. The fits are shown in Figure 6.3 for the same bins as before. The asymmetry distributions are broadened towards larger asymmetry values, and hence the entire range should not be fitted. This is most probably an effect of pileup: low energetic jets from inelastic scattering might pass the selection criteria and contribute to large asymmetry values. For high  $p_T^{avg}$  bins the effect

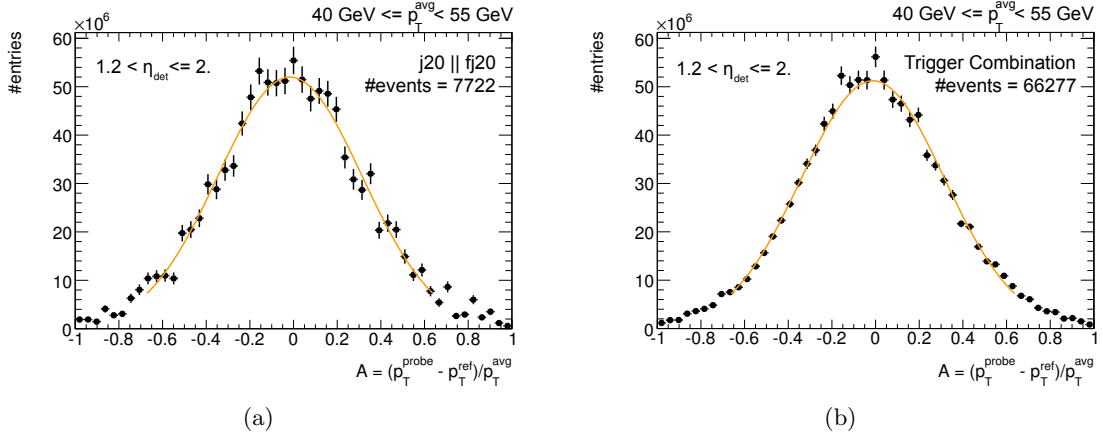


**Figure 6.5.:** Direct comparison between the TCM and the CM for one bin. (a) Shows the dijet asymmetry obtained when using the CM (b) Show the dijet asymmetry using the TCM. The statistical uncertainties are significantly smaller when using the TCM.

decreases which is consistent with this hypothesis. The fitting procedure starts with an optimal rebinning of the histogram using Scott's choice<sup>2</sup> and then an iterative fitting procedure within  $2\sigma$  of the distribution is applied. The range for the first fit is chosen to be  $[-0.8, 0.8]$  to account for the broadening of the distribution. The fitting procedure was done in agreement with the ATLAS pseudorapidity intercalibration group [44]. For all bins, within the errors the fits follow the shapes well.

As a cross-check of the jet trigger contributions, the same analysis has been performed using simulated samples. Figure 6.4 shows the contributions from different jet triggers to the dijet asymmetry using Pythia as simulation. Even though the simulation suffers from low statistics, the gaussian shape is clearly visible. Comparing the contributions to the asymmetry from the simulation and data, depicted in Figure 6.2, one can see that the trigger contributions from simulations are in good agreement with the obtained data distributions. For the lowest  $p_T^{avg}$  bin shown, the contribution of j40, j30 and j20 are very similar to the respective contribution in data. The contributions to the asymmetry in the next visible bin,  $75 \text{ GeV} \leq p_T^{avg} < 100 \text{ GeV}$ , predicts the expected jet triggers j75, j55 and j40 to contribute, but not the j20 trigger. For both other bins,  $170 \text{ GeV} \leq p_T^{avg} < 220 \text{ GeV}$  and  $400 \text{ GeV} \leq p_T^{avg} < 600 \text{ GeV}$ , the predicted jet trigger contributions from the simulation support the contributions in data.

In Figure 6.5 a direct comparison of the TCM and the CM for the lowest visible  $p_T^{avg}$  and pseudorapidity bin as before, is shown. Figure 6.5(b) shows the obtained asymmetry distribution when using the TCM and Figure 6.5(a) shows the same asymmetry when using the CM with the standard trigger selection. In this  $p_T^{avg}$  bin, the standard trigger selection requires the j20 OR the fj20 to have accepted the event. The same weight as for the TCM was applied to the j20 and fj20, respectively for a better comparison. The unweighted number of events  $N$ , selected with the TCM is  $N_{TCM} = 66277$  whereas the unweighted number of selected events

<sup>2</sup>Scott's choice is a method to rebin a histogram by minimizing the integrated mean squared error. The optimal bin width  $w$  is given as  $w = \frac{3.5 \sigma}{\sqrt[3]{n}}$  with  $\sigma$  being the standard deviation and  $n$  the total number of events in the histogram [43].

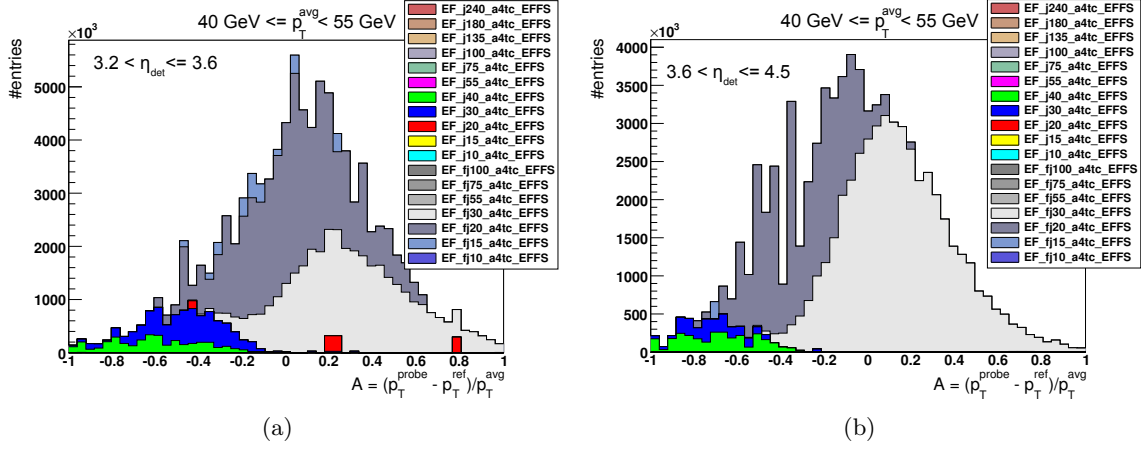


**Figure 6.6.:** Trigger contributions to the dijet asymmetry in the two most forward bins. Besides several forward triggers, also several central triggers have selected events.

with the CM is  $N_{CM} = 7722$ . Event selection with the TCM allows to use about nine times more statistics, compared to the standard trigger selection. From Equation 5.7 the influence on the statistical uncertainty can be determined. This reduces the systematical uncertainty in this  $p_T^{avg}$  bin from 0.4% for the CM to 0.1% in the central region. In the forward region, the systematical uncertainty can be reduced by a factor of 10 from 1% for the CM to 0.1% for the TCM method.

### Forward Region

For the forward  $\eta_{det}$ -region, the asymmetry distributions look similar. In Figure 6.6 the  $p_T^{avg}$  bin  $40 \text{ GeV} \leq p_T^{avg} < 55 \text{ GeV}$  and the two most forward  $\eta_{det}$  bins  $3.2 < \eta_{det} \leq 3.6$  (left) and  $3.6 < \eta_{det} \leq 4.5$  (right) are shown. Contributions arise from the forward jet triggers fj30, fj20 and fj15 as well as from the central jet triggers j40, j30 and on the left side also small contributions from j20. The reference jet is always selected by a central jet trigger, since the reference region is chosen accordingly. As opposed to the probe jet, which is always accepted by a forward trigger, since the pseudorapidity bin is determined using the probe jet. Hence, the contributions from central triggers arise from events, where the reference jet was accepted by the trigger. Additionally, the statistics are lower in the forward region compared to the central region at equal  $p_T^{avg}$  bins, but the gaussian shape of the distributions is nevertheless recognizable.

## 6.2. Calorimeter Responses

By fitting all asymmetry distributions with a gaussian function, the mean value  $\langle \mathcal{A} \rangle$  can be determined for each  $p_T^{avg}$  and  $\eta_{det}$  bin. The calorimeter response, which is defined as the inverse calibration constant  $1/c$  is calculated with Equation 5.5 and is visualized in response plots.

### Comparison with Simulation

The calorimeter response to jets, as a function of the average transverse momentum and the pseudorapidity, are shown in Figure 6.7. The relative calibration constants are depicted as a function of the pseudorapidity for four  $p_T^{avg}$  bins. For comparison, the responses obtained with the Monte Carlo generators Pythia (red) and Herwig++ (blue) are also shown. Two different Monte Carlo generators are used. Since the hadronization models used for generating the events are not the same, the outcome is different on a level of a few percent. In the lower part, the ratio of the simulations over the data (MC/Data) is shown, for a better comparison of the relative differences between them. All  $p_T^{avg}$  bins show a mostly flat distribution, but in forward region the response is always below one. This is expected, since forward jets are expected to have additional radiation. The comparisons between data and the simulations show, over all average transverse momentum bins and all available pseudorapidity bins, a very good agreement.

In the Figures 6.7(a) and 6.7(b) four points in the forward region stick out compared to the other. The concerning pseudorapidity bin,  $3.2 \leq \eta_{det} < 3.6$ , includes the transition region between the barrel calorimeters and the forward calorimeter. Hence, the calorimeter response in this region is significantly influenced by the detector geometry. The lowest  $p_T^{avg}$  bin,  $40 \text{ GeV} \leq p_T^{avg} < 55 \text{ GeV}$ , shows the largest differences between simulation and data, up to about 20% differences in the forward region, but the differences in the majority of the pseudorapidity bins are smaller than 5%. In the central region, the agreement is within 1% to 3% and hence slightly better. In the forward region, Herwig seems to describe the data a little better than Pythia whereas in the central region, Pythia is closer to the data. This tendency is also visible in the medium high  $p_T^{avg}$  bins  $75 \text{ GeV} \leq p_T^{avg} < 100 \text{ GeV}$  and  $170 \text{ GeV} \leq p_T^{avg} < 220 \text{ GeV}$ . In the highest visible  $p_T^{avg}$  bin this difference is not visible anymore, since at a hadron collider with a center-of-mass energy of  $\sqrt{s} = 7 \text{ TeV}$ , jets with such high transverse momenta cannot be produced in the very forward pseudorapidity range. In the second highest visible bin, the relative deviation between the simulation and data is only in the transition region about 10% for Pythia and less than 5% for Herwig. The majority of the central pseudorapidity bins,  $|\eta_{det}| < 2.1$ , has differences of 1% to 2%. In the  $p_T^{avg}$  bin  $170 \text{ GeV} \leq p_T^{avg} < 220 \text{ GeV}$ , shown in Figure 6.7(c), the responses in the transition regions deviate about 5% and for ranges  $|\eta_{det}| > 2.1$  the differences are about 3% to 5%. In the central region  $|\eta_{det}| < 2.1$  the agreement between simulation and data is better than 1%. For the highest visible  $p_T^{avg}$  bin,  $400 \text{ GeV} \leq p_T^{avg} < 600 \text{ GeV}$ , in Figure 6.7(d), almost over the entire pseudorapidity range the agreement is better than 1%, only in the range  $0.8 < |\eta_{det}| < 1.2$  it is slightly worse with an agreement of about 2%.

## 6.2. Calorimeter Responses

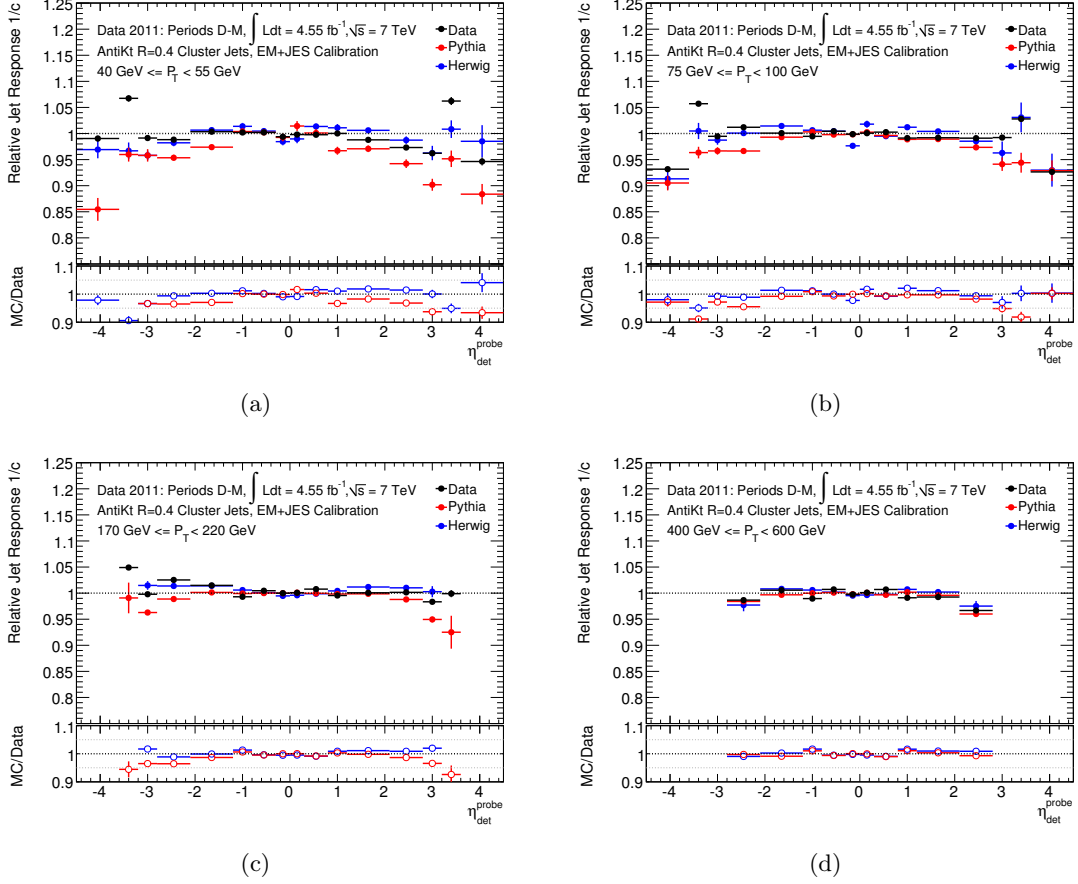


**Figure 6.7.:** Calorimeter responses to jets for four  $p_T^{avg}$  bins. The data (black) is compared to Pythia (red) and Herwig++ (blue).

Two further conspicuous characteristics should be mentioned. First, in the forward region  $2.8 < |\eta_{det}| < 3.5$  there seems to be a minor asymmetry in the two forward directions. In the negative range, the response seems to be always slightly higher, than in the positive forward region. Interestingly, the systematic error, discussed later in this Chapter, seems to have a similar tendency: the uncertainties in the positive forward region are slightly larger compared to the uncertainties in the corresponding negative pseudorapidity range. Second, for higher  $p_T^{avg}$  bins, starting at  $75 \text{ GeV} \leq p_T^{avg} < 100 \text{ GeV}$ , the  $0.8 < |\eta_{det}| < 1.2$  bin has always a lower response in data compared to simulation, which is also seen when using the standard methods, discussed in the next Section. This is a little surprising, since there is no transition region or crack region in the calorimeter design. Nevertheless, it is unlikely due to a physics effect, presumably it is rather due to detector effects. Maybe more passive material is in front of the calorimeter in that  $\eta_{det}$  bin or noisy cells worsen the response. Nevertheless, over the entire  $p_T^{avg}$  range, the responses are stable and show overall a good agreement with the simulation.

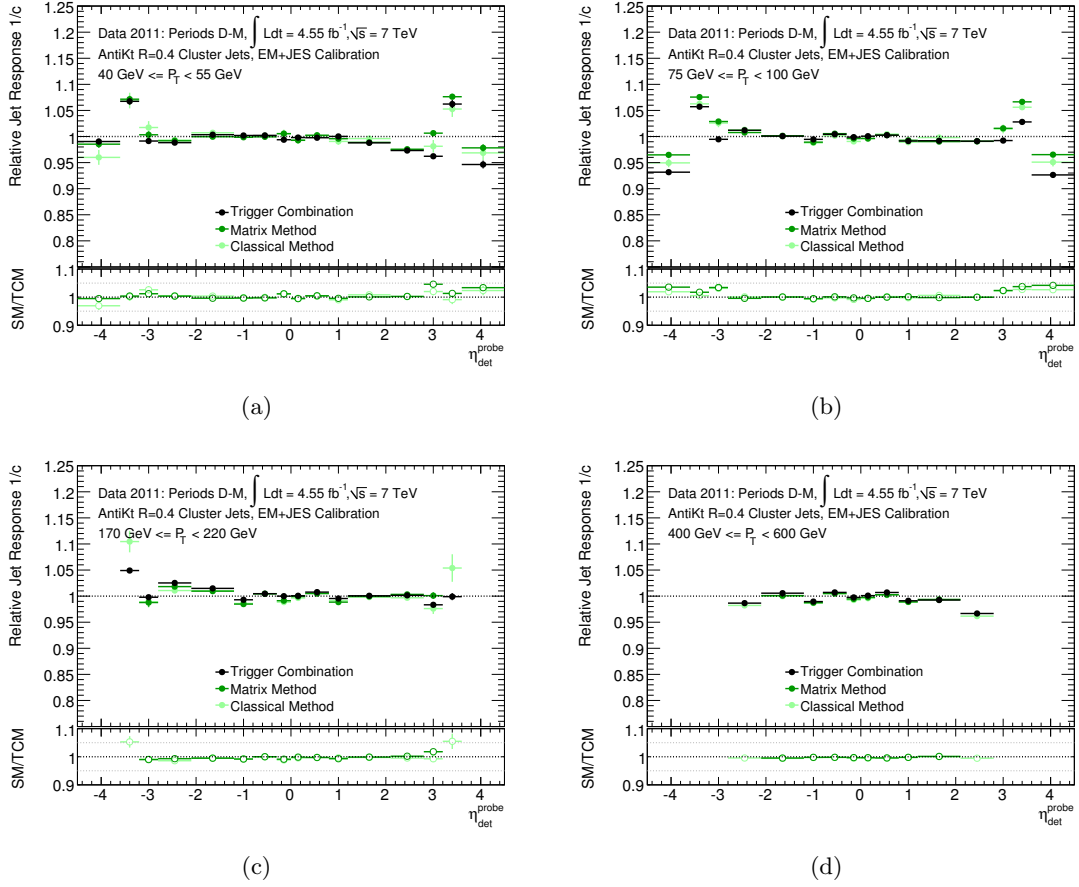


**Figure 6.8.:** Calorimeter responses to jets for the same four  $p_T^{avg}$  bins as before. In black the results from the TCM, in dark green the results from the Matrix Method and in light green the results from the Classical method are depicted.

## Comparison with Standard Methods

The results obtained by the Trigger Combination Method, are now compared with the official in-situ jet pseudorapidity intercalibration results of the ATLAS collaboration in 2011. The data files for the Classical and Matrix Method [44] and the official intercalibration results from 2011 were published in an ATLAS internal note, see reference [4]. In general a good agreement between the official results and the results obtained with the TCM are visible. The statistical uncertainty of the CM is about 2% in the lower transverse momentum bins and falls below 1% in the central region for higher transverse momentum bins. The statistical uncertainty of the Matrix Method is below 0.5% for the most pseudorapidity bins and rises to 1% for very forward jets with high transverse momenta. The statistical errors of the TCM are of comparable size.

In Figure 6.8 the comparison between the three methods is shown, the response from the TCM in black, the Matrix Method in dark green and the Classical Method in light green. The same four  $p_T^{avg}$  bins as before are shown. For each bin the relative responses are depicted

in the upper part and the ratios between the Standard Methods and TCM (MM/TCM or CM/TCM) in the lower part. In the lowest visible  $p_T^{avg}$  bin,  $40 \text{ GeV} \leq p_T^{avg} < 55 \text{ GeV}$ , shown in Figure 6.8(a), the agreement in the central region,  $|\eta_{det}| < 2.8$ , is better than 1%. In the forward region, it is mostly better than 4% only in the bin  $2.8 < \eta_{det} < 3.2$  the MM and the TCM have a difference of 5%. The difference between the CM and the TCM in that bin is only about 2%. Figure 6.8(b) shows the next higher  $p_T^{avg}$  bin,  $75 \text{ GeV} \leq p_T^{avg} < 100 \text{ GeV}$ , here again in the central region  $|\eta_{det}| < 2.8$  the three methods agree better than 1%. In the forward region the agreement gets a little worse with about 5% between the MM and the TCM and the difference between the CM and the TCM is smaller than 3%. In the forward region of that  $p_T^{avg}$  bin, the TCM has always a lower response compared to the two other methods. Nevertheless, this tendency is neither seen in the lower nor in the higher  $p_T^{avg}$  bins and hence, it is assumed that it is not a systematical bias. The  $p_T^{avg}$  bin,  $170 \text{ GeV} \leq p_T^{avg} < 220 \text{ GeV}$ , is depicted in Figure 6.8(c). In the bin  $3.2 < |\eta_{det}| < 3.6$  the MM runs out of statistics and hence, no data points are shown. The agreement between the three methods is over most of the pseudorapidity range better than 1%. An exception is the previously named  $\eta_{det}$  bin, with a difference between the CM and the TCM of about 5%, but within the large errors of the CM, the agreement is still acceptable. Also, the alleged systematical shift in the forward region vanishes in the last reachable  $\eta_{det}$  bin. In the highest visible  $p_T^{avg}$  bin,  $400 \text{ GeV} \leq p_T^{avg} < 600 \text{ GeV}$ , shown in Figure 6.8(d) the agreement between all three methods over the entire pseudorapidity range is better than 1%.

In summary, there is a good agreement between the three methods over the entire  $p_T^{avg}$  range. The largest differences in the calorimeter responses between the three methods appear in forward direction. It seems, that in general CM and TCM have slightly smaller differences than the MM compared to the TCM. This might arise from the underlying analysis: Classical and Trigger Combination Method utilize the same analysis technique whereas the analysis of the MM is very different.

### 6.3. Systematical Uncertainty

Selection requirements and differences in the modeling of the simulations, set a systematical uncertainty on the TCM. In this Section, influences of these sources, as well as the choice of the triggers and the negligence of the L2 trigger decision in the emulation are studied and summarized at the end.

#### Azimuthal Separation Selection

The event selection requires the two leading jets to have a minimum separation of  $\Delta\varphi > 2.5$ . To estimate the influence on the dijet balance, the analysis is performed with varied values. The variation was done in both directions in the range  $\pm 0.4 \text{ rad}$  around the original value, in steps of  $0.2 \text{ rad}$ . The uncertainty was taken as the largest deviation between the responses of the variations and the nominal  $\Delta\varphi_{1,2}$  selection. In the forward region, it contributes with  $\sim 1\%$  to the total uncertainty and in the central region mostly less than  $0.1\%$ .

## Soft Radiation Suppression

The presence of soft radiation can influence the dijet balance and hence different soft radiation conditions have been studied. In order to do so, the requirements on the third jet, described earlier in this Chapter, were varied. This includes independent variations of the selection criteria of the JVF value, the relative amount of the  $p_T$  of the third jet compared to the  $p_T^{avg}$  of the two leading jets, and the minimum  $p_T$  value. The JVF selection requires a nominal value of 0.6 and was varied in steps of 0.1 in a range  $\pm 0.2$  of the nominal value. The relative amount of transverse momentum of the third jet was varied in the range of  $\pm 10\%$  around the nominal values in steps of 5%. The minimum transverse momentum of the third jet was varied by  $\pm 4$  GeV around the nominal value in 2 GeV steps. The contribution to the total uncertainty is about 1% in the central region and can rise to 7% to 8% in the forward direction.

## Trigger Selection

The Trigger Combination Method combines many different triggers, each of them not necessarily fully efficient, but the set of them must be fully efficient. To estimate the influence of the number of triggers to the dijet balance, the analysis was rerun with different numbers of triggers. Two additional runs were performed: in the first run, two triggers, j240 and fj100, were excluded and in the second four triggers, j180, j40, fj100 and fj30, were excluded. The maximum difference between the dijet response with all available triggers and the two runs with reduced number of triggers was taken as systematical uncertainty. The contribution to the total uncertainty is larger in the forward region with about 3% and about 0.5% in the central region.

## L2 Emulation

As mentioned earlier, the trigger emulation only emulates the L1 and the EF decision. At L2 the required information is not always stored, e.g. in case the L1 had a raw decision but no physics. Then the L2 objects are not available to check a potential acceptance. Hence, an estimation of the negligence of the L2 decision was derived by emulating the L2 decision in the simulation. This was possible, since the simulated samples have all the needed information to emulate the L2 decision. The difference between the simulation with and without the L2 emulation was taken as another source of systematic uncertainty. Two different simulation samples were used, namely Pythia and Herwig++, to estimate the uncertainty. The two Monte Carlo generators utilize different showering models leading to differences in the number of produced jets or differences in the angular distributions. The differences of the two generators were also observed in the calorimeter response and are visible in Figure 6.7. Especially in the forward region, the prediction of the two simulations deviate from each other. Since none of the two simulations has an a priori reason to be more truthful, both samples were used to determine the L2 influence. The differences, of the simulation with and without the L2 decision, were taken for both simulations and the averaged difference was

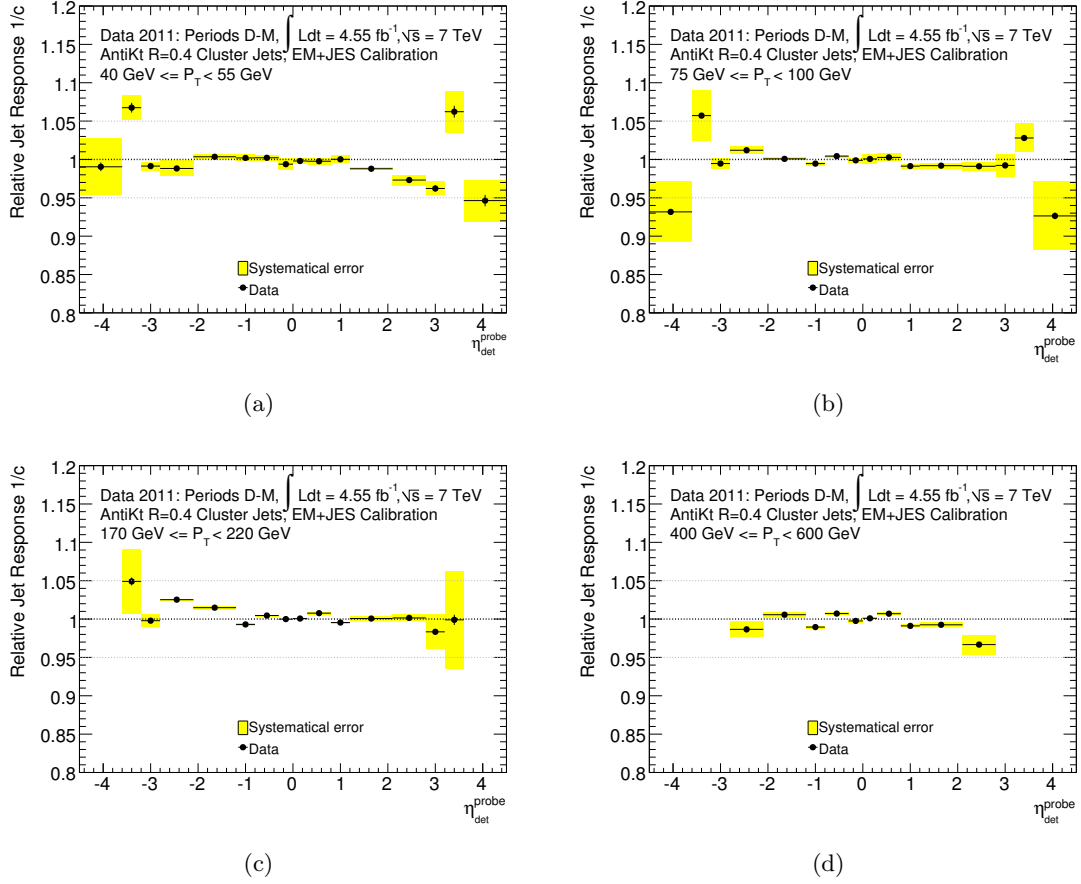


**Figure 6.9.:** Statistical (black error bars) and systematical (yellow rectangles) uncertainties of the TCM. The TCM is clearly limited by systematical effects.

included in the total systematical uncertainty. The contribution to the total systematical uncertainty is less than 0.5 %.

## Total Uncertainty

The total systematic uncertainty was determined by taking the quadratic sum of the individual components. In Figure 6.9 the calorimeter responses obtained with the TCM as well as the statistical (black error bars) and systematical uncertainties (yellow rectangles) are shown. The errors of the TCM, using the complete 2011 data from ATLAS, are clearly dominated by systematical effects. The shown  $p_T^{avg}$  bins are the same as discussed before. In Figure 6.9(a), the lowest visible  $p_T^{avg}$  bin  $40 \text{ GeV} \leq p_T^{avg} < 55 \text{ GeV}$ , the largest errors are in the most forward pseudorapidity range  $3.6 < |\eta_{det}^{probe}| < 4.5$  with 3% - 4%, followed by the pseudorapidity bins in the transition region  $3.2 < |\eta_{det}^{probe}| < 3.6$  with 2% - 3%. The central region has a maximum error of 1%, often even less. The same tendency is seen in the next visible  $p_T^{avg}$  bin  $75 \text{ GeV} \leq p_T^{avg} < 100 \text{ GeV}$  in Figure 6.9(b). The largest errors are in the most forward bin with errors up to 4% and errors in the transition region between 2% and 3%. The  $2.8 < \eta_{det}^{probe} < 3.2$

bin is a little higher compared to the remaining bins with about 1.5%. All other central bins have a maximum of about 1%, often less. In the  $p_T^{avg}$  bin,  $170 \text{ GeV} \leq p_T^{avg} < 220 \text{ GeV}$ , shown in Figure 6.9(c), the central bins  $|\eta_{det}| < 2.8$  show a systematical uncertainty smaller than 1%. In the positive forward region, the errors are slightly larger than in the negative forward region with 2% ( $2.8 < \eta_{det} < 3.2$ ) and 6% ( $3.2 < \eta_{det} < 3.6$ ) and 1% ( $-2.8 > \eta_{det} > -3.2$ ) and 4% ( $-3.2 > \eta_{det} > -3.6$ ), respectively. Figure 6.9(d) also has the highest uncertainty in the accessible forward bins  $2.1 < |\eta_{det}| < 2.8$  with less than 2%, and also here the positive forward direction has a slightly larger uncertainty than the negative direction. All remaining bins have an uncertainty significantly smaller than 1%.

As mentioned before, for most of the  $p_T^{avg}$  bins, the positive forward direction has slightly larger systematical uncertainties and hence can cover the asymmetry seen in positive and negative forward direction.

The negligence of the L2 decision gives only small contributions to the total systematic uncertainty. Its largest contribution is in the bin  $40 \text{ GeV} \leq p_T^{avg} < 55 \text{ GeV}$  with a maximum of 0.5%. Hence the negligence of the L2 trigger decision can be justified.

The systematical uncertainty is dominated by changing soft radiation conditions which is not a direct systematic of the TCM itself and in some very forward bins of the chosen triggers. The large contribution from additional soft radiation might arise from a conservative treatment of this contribution by varying the selection criteria on the third jet and always considering the largest deviation from the nominal data. The standard methods, compare [4], are not dominated by this contribution since they use a slightly different way to estimate the contribution. The variations of the third jet selection are applied to data and MC obtaining a new intercalibration. The percent difference between the nominal and varied intercalibration are used as uncertainty estimation. More detailed studies of the influences of changing soft radiation conditions on the dijet balance might be able to reduce the total systematical uncertainty.

# Conclusions

The accurate knowledge of the jet energy scale (JES) and its uncertainty is a crucial part for many SM and new physics analyses. The determination of the JES uncertainty consists of various steps and several in-situ measurements, which are combined to the total JES uncertainty. One of these in-situ measurements is the jet pseudorapidity intercalibration to obtain an equal calorimeter response to jets over the entire pseudorapidity range. The standard methods utilize only fully efficient triggers for the event selection which limits their statistics due to high prescale factors of some triggers. This thesis presented a new method of selecting appropriate dijet events, the so called Trigger Combination Method (TCM). The method combines many different triggers and allows an optimal utilization of the triggers and their prescale factors. This new way of selecting dijet events was applied to the Classical Method (CM) of the jet pseudorapidity intercalibration with the goal to decrease the statistical component of the JES uncertainty.

The TCM was implemented and tested using 2011 data collected with the ATLAS detector. Comparisons of the obtained calorimeter response to calorimeter response obtained from two different simulation samples showed overall a good agreement. The obtained calorimeter response was also compared to official ATLAS results using the Classical and Matrix Method (MM) with the standard trigger selection. Over the entire momentum and pseudorapidity range a good agreement was observed between the different methods. Depending on the momentum region, the TCM accepts up to ten times more events in the central barrel region and up to forty-eight times more events in the forward region compared to the Classical Method with the standard trigger selection. This reduces the statistical uncertainties in the barrel region up to a factor of three and in the forward region up to a factor of ten. The MM and the TCM, used with the CM, have statistical uncertainties of comparable sizes. Systematical studies have shown small systematical uncertainties of about 1% in the central region but larger uncertainties of about 6% in the forward region. The dominant contribution to the total systematic uncertainty arises from additional soft radiation which is not directly arising from TCM. For the official jet pseudorapidity intercalibration results of ATLAS this contribution is determined differently and it is not dominating the total uncertainty. Hence, more systematical studies are encouraged to reduce the total systematical uncertainty of the TCM. Studies to explain the origin of the asymmetry in the forward directions and if it can be eliminated are also recommended.

Applying the Trigger Combination Method to the jet pseudorapidity intercalibration showed good agreement in comparisons between data and simulation as well as between TCM results and the official ATLAS jet intercalibration results. This successful application of the TCM to the CM provides a good alternative to the MM and allows the application of the TCM to the MM to further reduce the statistical uncertainty or to physics analyses in order to improve the usage of the available statistics.

# Jet Pseudorapidity Intercalibration using 2010 Data

The TCM method was first tested using data, collected by the ATLAS detector in the first half of the year 2010 and corresponds to an integrated luminosity of  $2.9 \text{ pb}^{-1}$ . The trigger setup was very different from the setup in the following years, since no jet trigger chains were used and only L1 trigger was on. The method was easier to implement since only the L1 decision needed to be emulated. A list of the available jet triggers in 2010 are listed in Table A.1 with the collected integrated luminosities and the corresponding weights. Compared to 2011, less jet triggers were used: only four central triggers, two forward triggers and the *Minimum Bias Trigger Scintillator* (MBTS), an effectively random trigger. The triggers had already prescales applied, and the corresponding weights were calculated with Equation 5.14. For the analysis, the same preselection has been used: a primary vertex with at least five tracks, at least two jets in the event, neither bad nor ugly jets are allowed in the event and a GRL was applied. The azimuthal difference between the two jets has to be larger than  $\Delta\varphi(\text{jet}_1, \text{jet}_1) > 2.6$  and the restriction on additional jets was less advanced: the transverse momentum of the third jet had to be smaller than 15 % of the average transverse momentum of the two leading jets:  $p_T^{j3} < 0.15 \frac{(p_T^{j1} + p_T^{j2})}{2}$ .

The  $p_T^{avg}$  binning was different for the Classical and the Matrix Method, listed in Table A.2. The  $\eta$  binning was also slightly different for the CM and the MM, with the reference region  $0.1 < |\eta| < 0.6$  for the CM and  $|\eta| < 0.8$  for the MM. For a better comparison, the analysis using the TCM has been performed with both binnings. The asymmetry distributions are determined and fitted with a gaussian with the mean value as free parameter. The calorimeter responses are shown in Figure A.1 obtained with the TCM (black) in comparison with the results from the Classical Method (light green). The results for the official jet pseudorapidity intercalibration are published under reference [3].

## Calorimeter Responses

The calorimeter responses for the TCM using 2010 data are shown in Figure A.1 in black with the Classical Method in light green. The used jet reconstruction algorithm is the AntiKt algorithm with the distance parameter  $R = 0.6$ . The first  $p_T^{avg}$  bin,  $20 \text{ GeV} \leq p_T^{avg} < 30 \text{ GeV}$ , is depicted in Figure A.1(a). Classical Method and Trigger Combination Method agree over most of the pseudorapidity range very well. The errors<sup>1</sup> are always smaller for the TCM

<sup>1</sup>Only statistical uncertainties are shown.

jet trigger	$\int \mathcal{L} [\mu\text{b}^{-1}]$	Weight
J30	1752997.8	1.5
J15	436434.7	5.9
J10	93533.7	27.3
J5	21895.5	116.8
FJ30	2558104.8	1.0
FJ10	221097.0	11.6
MBTS	772.8	3310.2

**Table A.1.:** The table shows the available jet triggers in 2010 which were used for the analysis. Besides the jet triggers with thresholds, the MBTS trigger was available, a trigger which selects events effectively on a random basis.

Matrix Method	Classical Method
$20 \text{ GeV} \leq p_T^{avg} < 30 \text{ GeV}$	$20 \text{ GeV} \leq p_T^{avg} < 30 \text{ GeV}$
$30 \text{ GeV} \leq p_T^{avg} < 45 \text{ GeV}$	$30 \text{ GeV} \leq p_T^{avg} < 40 \text{ GeV}$
$45 \text{ GeV} \leq p_T^{avg} < 60 \text{ GeV}$	$40 \text{ GeV} \leq p_T^{avg} < 50 \text{ GeV}$
$60 \text{ GeV} \leq p_T^{avg} < 80 \text{ GeV}$	

**Table A.2.:** The Tables shows the used  $p_T^{avg}$  binning in 2010 for the Classical and the Matrix Method.

compared to the CM and no systematical shift is observed. The same tendency is observed in the other bins  $30 \text{ GeV} \leq p_T^{avg} < 40 \text{ GeV}$  and  $40 \text{ GeV} \leq p_T^{avg} < 50 \text{ GeV}$ , shown in Figures A.1(b) and A.1(c), respectively. The TCM shows over all three  $p_T^{avg}$  bins a more stable and a flatter response than the CM. Additionally, the errors of the TCM are significantly smaller, up to 4% less, than for the CM.

Comparisons of the 2010 calorimeter response with the Matrix Method are shown in Figure A.2. In the lowest bin, Figure A.2(a), a systematical shift is observable: the TCM response is always below the MM. Nevertheless, this is not observed for any other  $p_T^{avg}$  bin. This might be an effect from using the MBTS trigger. In this  $p_T^{avg}$  bin, the MBTS trigger is needed for the fully efficient combination. Due to its extremely high prescale, the statistics are rather low and maybe this causes a slight systematic effect. This hypothesis is also supported by the fact, that almost all other bins have no, or just very little contribution from the MBTS trigger and none of the additional bins show this systematical deviation. In the next visible bin, Figure A.2(b), the two responses agree well within their errors. The TCM shows also a slightly more flat response compared to the MM. Both other bins, in Figure A.2(c) and Figure A.2(d) have similar characteristics. Almost over all shown  $p_T^{avg}$  bins, the TCM has smaller statistical errors, than the MM or at least errors of comparable sizes. Only in the forward region of the two high  $p_T^{avg}$  bins has the MM smaller errors.

Comparisons of the TCM to the MM and the CM using 2010 data, demonstrate a good agreement of the obtained calorimeter responses. The CM and the TCM have a largest

deviation of 4% and the MM and the TCM of about 5%. The statistical uncertainties are always smaller for the TCM, compared to the CM, and often also smaller compared to the MM. For the high  $p_T^{avg}$  bins, the errors of TCM and MM become of comparable sizes and in the forward region the MM has slightly smaller errors. No comparisons to simulation were made for 2010 data. Applying the TCM successfully to the jet pseudorapidity intercalibration using 2010 data, encouraged deeper studies using 2011 data.

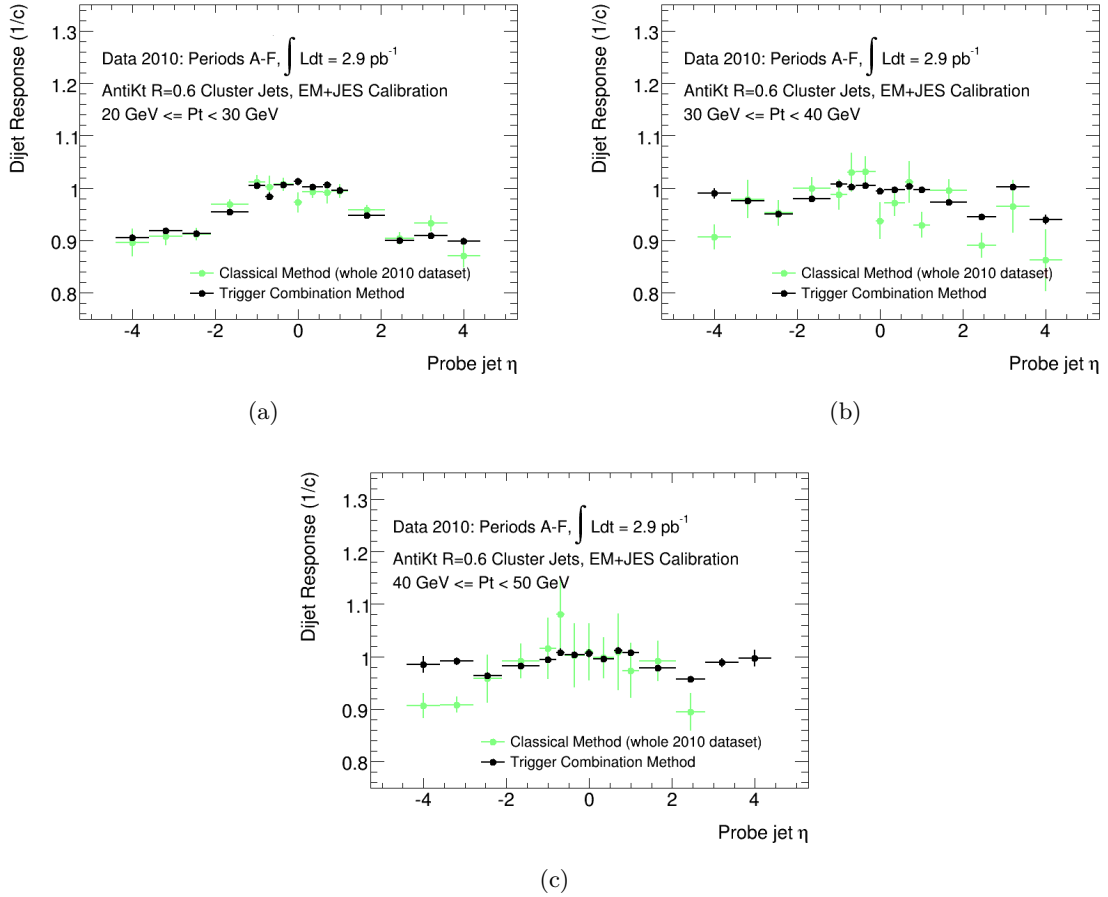


**Figure A.1.:** Calorimeter responses for the TCM (black) and the CM (light green) using 2010 data. Over all bins a good agreement is observable. The TCM has always smaller error than the CM.

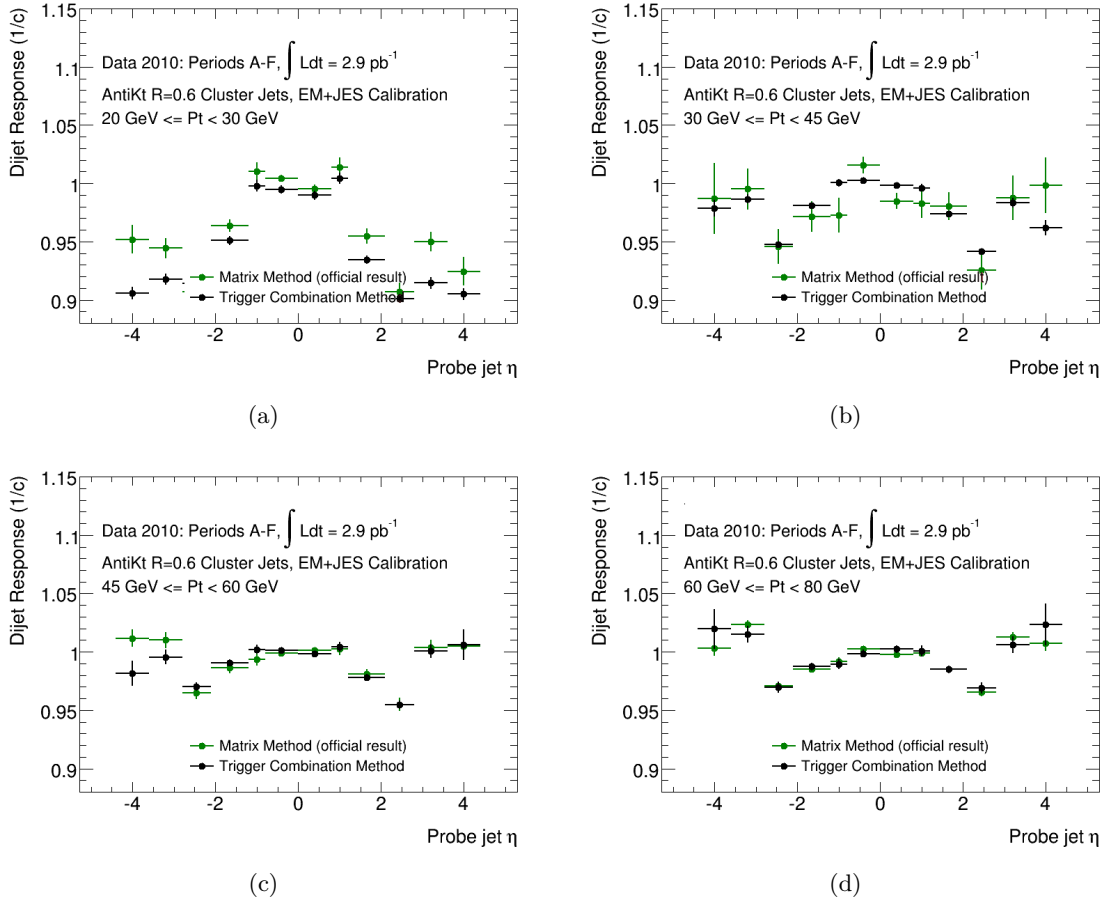


**Figure A.2.:** Calorimeter responses for the TCM (black) and the MM (dark green) using 2010 data. Over all bins a good agreement is observable. The TCM has often smaller or at least comparable errors as the MM, only in the forward pseudorapidity bins for the two highest  $p_T^{avg}$  bins, the MM has smaller statistical errors.

# Calorimeter Responses for 2011 using AntiKt6

The jet pseudorapidity intercalibration is also performed using jets reconstructed via the AntiKt algorithm, using the distance parameter  $R = 0.6$ . The trigger setup is the same, but the trigger efficiencies are slightly different for AntiKt6 and hence the  $p_T^{avg}$  binning is different. The  $p_T^{avg}$  binning and the used triggers are listed in Table B.1.

$p_T^{avg}$ [GeV]	trigger	complementary fwd. trigger
30 - 40	j10	fj10
40 - 55	j15	fj15
55 - 70	j20	fj20
70 - 105	j30	fj30
105 - 145	j55	fj55
145 - 190	j75	fj75
190 - 240	j100	fj100
240 - 300	j135	fj100
300 - 400	j180	fj100

**Table B.1.:**  $p_T$  bins for the AntiKt6 algorithm and the highest fully efficient central and forward trigger in that  $p_T$  range. Triggers are abbreviated for EF\*\_a4tc\_EFFS.

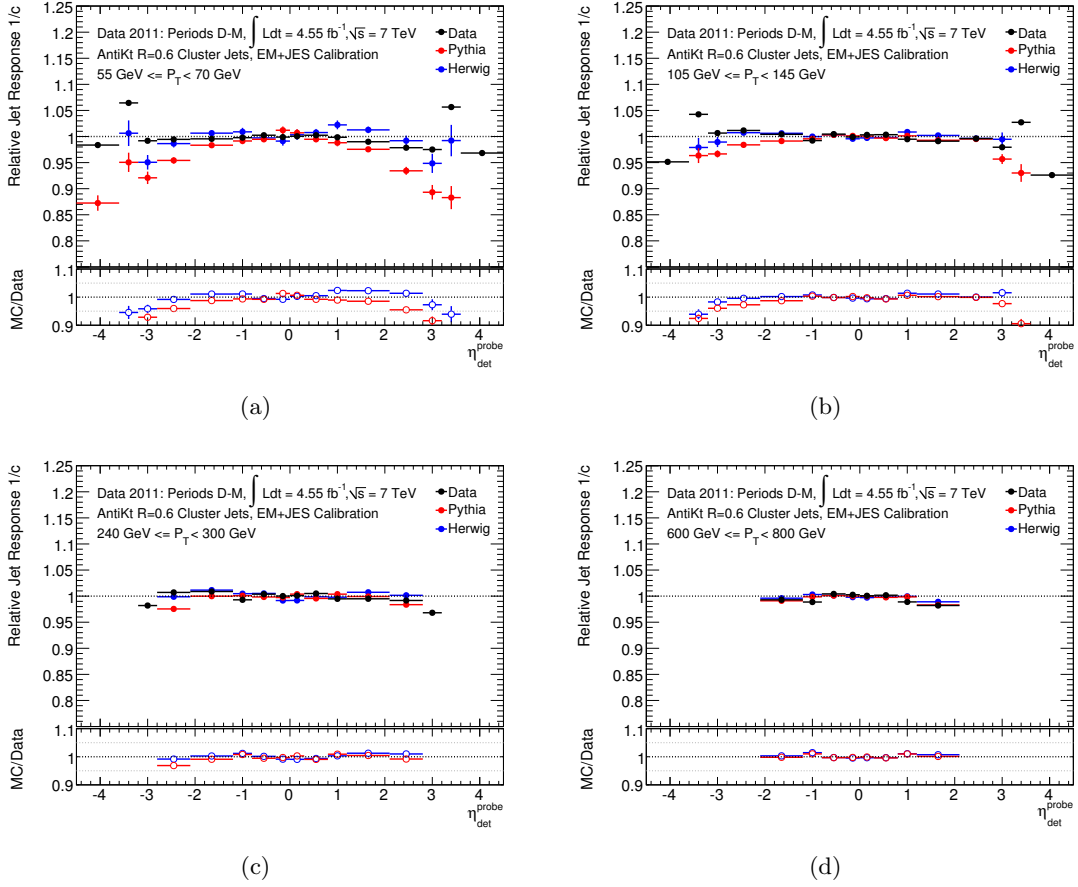


**Figure B.1.:** Calorimeter responses to jets four  $p_T^{avg}$  bins. The data (black) is compared to Pythia (red) and Herwig++ (blue). The used jet reconstruction algorithm is AntiKt6.

The determined calorimeter responses are shown in Figure B.1 for data (black), Pythia (red) and Herwig++ (blue). The four shown  $p_T^{avg}$  bins show similar behavior as the corresponding responses using the AntiKt4 algorithm. The deviation from the simulation samples and data are largest for the lowest visible  $p_T^{avg}$  bin with more than 10% in the forward region. The central region has smaller differences within 5%. For all other shown bins, the differences are mainly smaller than 5% in the forward region and smaller than 1% in the central region. An exception is the transition region,  $2.9 < |\eta| < 3.2$ , where the differences are up to 10%. Also, as already seen in the comparison using the AntiKt4 algorithm in Figure 6.7, Herwig++ describes the data better in the forward region, whereas Pythia is slightly better in the central region.

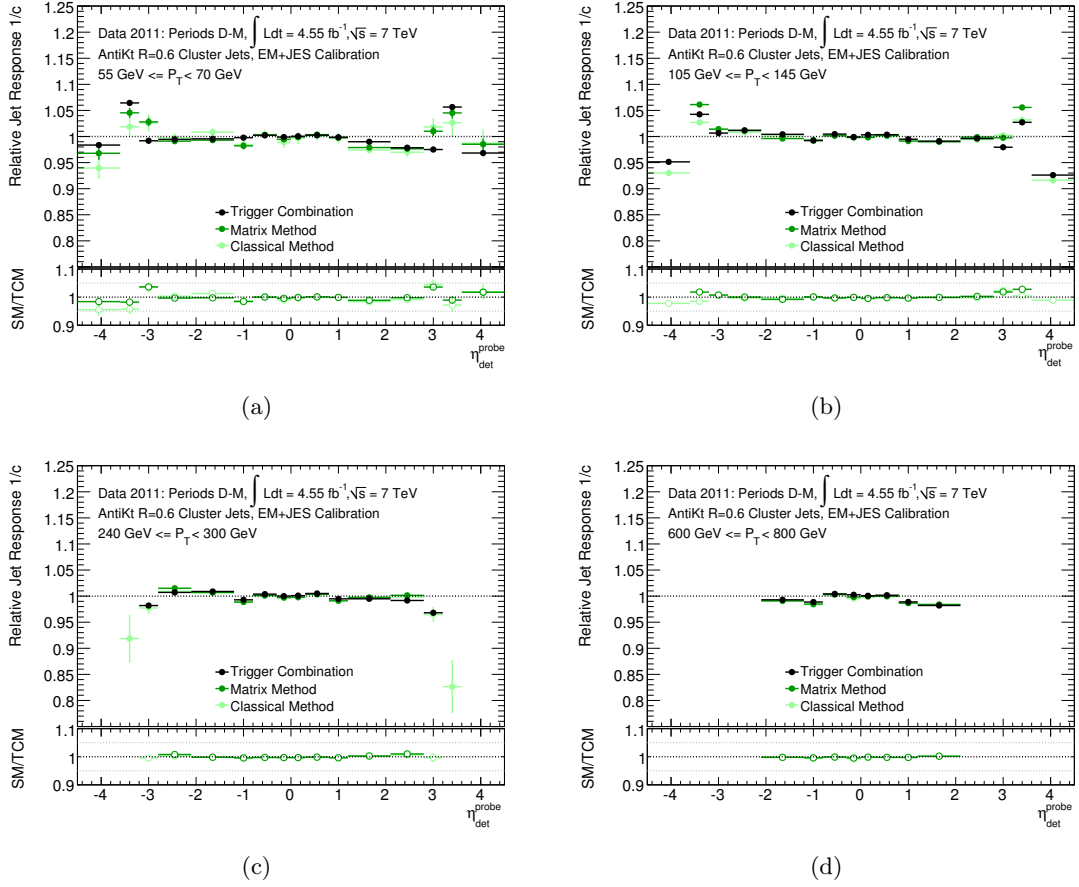


**Figure B.2.:** Calorimeter responses to jets for the same four  $p_T^{avg}$  bins as before. In black the results from the TCM, in dark green the results from the Matrix Method and in light green the results from the Classical method are depicted. The used jet reconstruction algorithm is AntiKt6.

Comparisons of the calorimeter responses to jets obtained with the standard methods are shown in Figure B.2. The agreement between the standard methods and the TCM is over all shown bins very good. The largest deviation occurs in the transition region,  $2.9 < |\eta| < 3.2$ , in the lowest shown  $p_T^{avg}$  bin with about 5%. The differences in the forward region are mostly about 3% and in the central region it is often less than 1%. Remarkable are the high statistics the TCM utilizes: for the three high  $p_T^{avg}$  bins shown, the statistical uncertainties for all three methods are very small, but in the lowest  $p_T^{avg}$  bin the statistical uncertainty is smaller for the TCM over the entire pseudorapidity range compared to the CM and also smaller than the uncertainties of the MM in the forward bins.

# Jet Pseudorapidity Intercalibration using 2012 Data

The jet pseudorapidity intercalibration using the TCM method is also performed using early 2012 data, collected by the ATLAS detector, corresponding to an integrated luminosity of  $2.0 \text{ fb}^{-1}$  at a center-of-mass of  $\sqrt{s} = 8 \text{ TeV}$ . The trigger setup is similar to the setup used in 2011, but changed slightly. The name convention for the standard jet triggers changed to  $EF\_*\_a4tchad$ , with  $EF$  for event Filter and  $a4tchad$  denotes that the jet reconstruction was done with a full-scan from topological clusters using the AntiKt4 reconstruction algorithm at EM+JES scale [45]. For 2012, as a part of the thesis, the trigger efficiencies are produced to determine the correct  $p_T^{avg}$  binning. In Figure C.1 one exemplary trigger efficiency, for the combination j80 OR fj80, in a central  $\eta$  bin,  $|\eta| < 1.2$ , is shown. The fit and the point of 99% is done in agreement with the official ATLAS jet pseudorapidity intercalibration group [44]. The resulting  $p_T^{avg}$  bins are listed in Table C.1 with the fully efficient triggers.

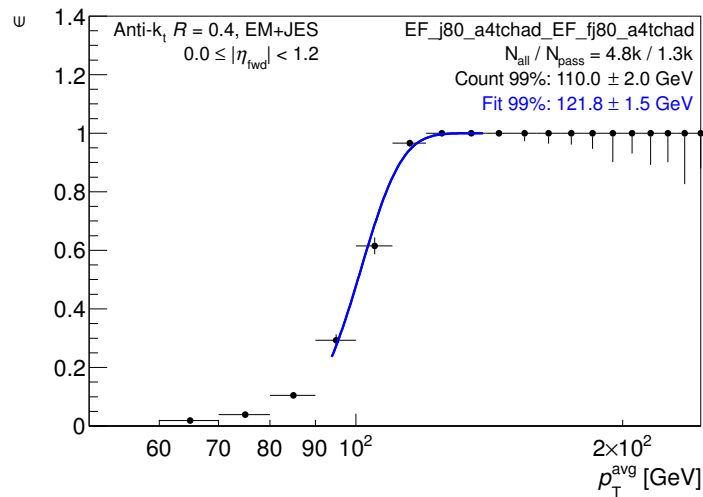


**Figure C.1.:** For the 2012 data, jet trigger efficiencies are derived. Here, the trigger efficiency curve for the combination of j80 OR fj80 is shown.

$p_T^{avg}$ [GeV]	trigger	complementary fwd. trigger
30 - 45	j15	fj15
45 - 60	j25	fj25
60 - 75	j35	fj30
75 - 90	j45	fj45
90 - 125	j55	fj55
125 - 160	j80	fj80
160 - 185	j110	fj110
185 - 240	j145	fj145
240 - 300	j180	fj180
300 - 380	j220	fj220
380 - 480	j220	fj220
480 - 600	j360	fj220
600 - 760	j460	fj220
760 - 1200	j460	fj220
1200 - 1500	j460	fj220

**Table C.1.:**  $p_T$  bins for the AntiKt4 algorithm and the highest fully efficient central and forward trigger in that  $p_T$  range. Triggers are abbreviated for EF\_\*\_a4tc\_EFFS .

The trigger setup from 2012 is listed in Table C.2, with the event filter and its L2 and L1 seeds, as well as their weights for the analysis. The *c4cchad* in the naming convention for the L2 triggers denotes jets, which are reconstructed from ROI-based calorimeter cells using a cone algorithm with a radius of  $R = 0.4$  at EM+JES scale<sup>1</sup>.

## Calorimeter Response

The calorimeter responses for four representative  $p_T^{avg}$  bins are shown in Figure C.2. In black, responses from data and in red the responses from Pythia are drawn. The lowest  $p_T^{avg}$  bin,  $30 \text{ GeV} \leq p_T^{avg} < 45 \text{ GeV}$ , depicted in Figure C.2(a), has deviations of less than 5%. The largest deviations appear in the barrel-endcap transition region ( $1.2 < |\eta| < 2.1$ ) and in the HEC-FCal transition region ( $2.8 < |\eta| < 3.2$ ). In the other regions, the agreement is better than 2%. In the next visible  $p_T$  bin,  $90 \text{ GeV} \leq p_T^{avg} < 125 \text{ GeV}$ , shown in Figure C.2(b) the central region,  $|\eta| < 2.1$ , has an agreement of about 1% or better between data and Pythia. In the more forward pseudorapidity bins the agreement is about 5%. The most forward pseudorapidity bin ( $2.8 \leq |\eta| < 3.2$ ) has a deviation of almost 10%, but within the errors data and Pythia are still in acceptable agreement. In Figure C.2(c), the  $p_T$  bin  $380 \text{ GeV} \leq p_T^{avg} < 480 \text{ GeV}$  the agreement is in the majority of bins about 1% or better. Only the most forward pseudorapidity bins have a slightly worse agreement of 2% to 3%. The last  $p_T^{avg}$  presented bin is  $760 \text{ GeV} \leq p_T^{avg} < 1200 \text{ GeV}$ , in Figure C.2(d). Over the entire accessible pseudorapidity range the agreement is 1% or better.

The comparison of data and simulation shows over all  $p_T^{avg}$  bins a good agreement. As in

<sup>1</sup>Which denotes not the complete calibration, but just a correction using one global constant.

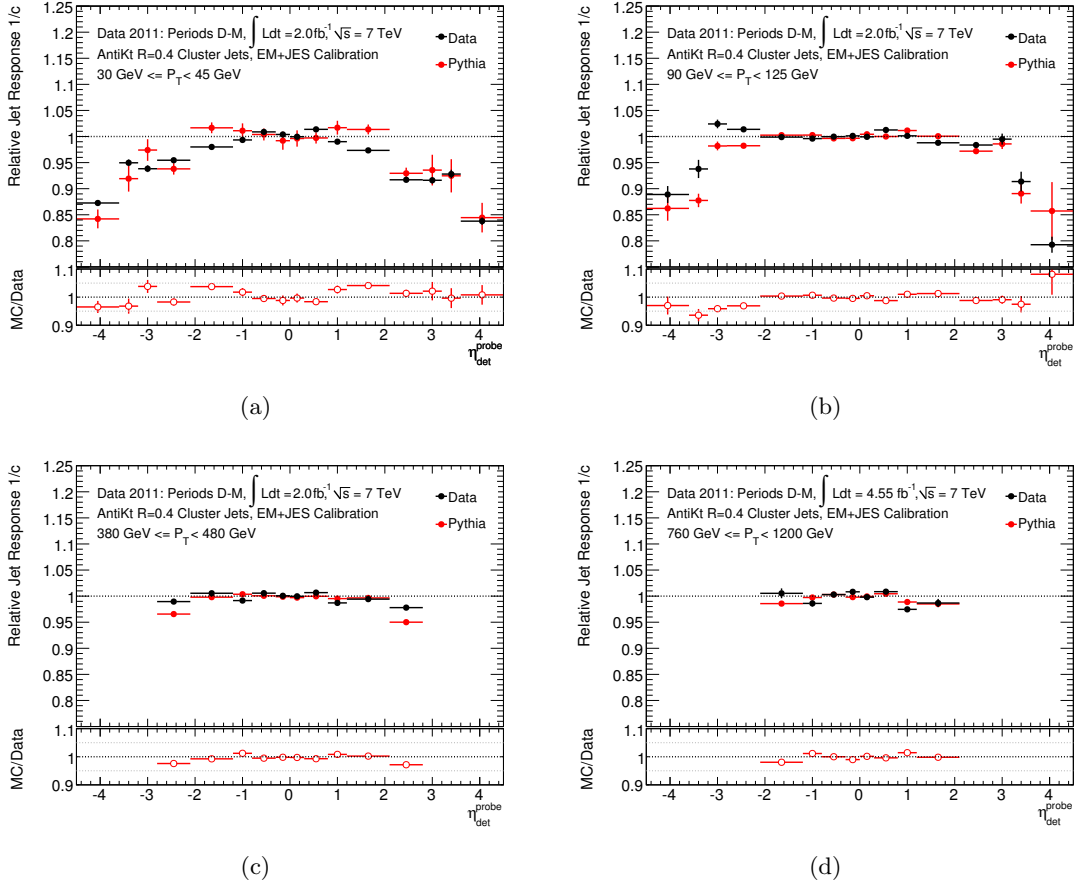


**Figure C.2.:** The figure shows the calorimeter responses of four  $p_T^{avg}$  bins. The data (black) is compared to Pythia (red) using 2012 data from ATLAS.

2011, in the pseudorapidity bin  $0.8 < |\eta| < 1.2$ , the calorimeter response for data is slightly below the response from simulation. Other than that, no systematic biases are observed.

No direct comparisons with the standard methods are possible for 2012, since the ATLAS collaboration did not publish the official intercalibration results before the printing.

EF_*_a4tchad(L2FS)	L2_*_c4cchad	L1_*	Weight
j460	j165	J75	1.0
j360	j165	J75	1.0
j280	j165	J75	4.7
j220	j165	J75	26.8
j180	j165	J75	138.6
j145	j140	J75	186.7
j110	j105	J55	707.0
j80	j75	J30	2892.5
j55	j55	J15	15476.7
j35	rdm	rdm	95872.0
j25	rdm	rdm	731653.6
j15	rdm	rdm	288961.6
fj220	fj140	FJ75	1.0
fj180	fj140	FJ75	1.0
fj145	fj140	FJ75	1.3
fj110	fj105	FJ50	3.7
fj80	fj75	FJ30	132.4
fj55	fj50	rdm	44729.6
fj35	rdm	rdm	44741.6
fj25	rdm	rdm	85754.4
fj15	rdm	rdm	224018.4

**Table C.2.:** 2012 single jet trigger chains used for the analysis.

---

# List of Figures

2.1. Production cross sections at LHC. . . . .	8
2.2. Dijet production plus X. . . . .	9
2.3. Leading order dijet production Feynman diagrams. . . . .	10
2.4. Double differential dijet cross section. . . . .	11
2.5. SUSY cascade decay. . . . .	13
2.6. Exclusion limits on SUSY searches. . . . .	14
3.1. LHC and its preaccelerating system. . . . .	17
3.2. ATLAS coordinate system. . . . .	18
3.3. ATLAS detector. . . . .	20
3.4. ATLAS inner detector. . . . .	22
3.5. ATLAS magnet system. . . . .	23
3.6. ATLAS calorimeter system. . . . .	24
3.7. An EM calorimeter module. . . . .	26
3.8. An hadronic tile calorimeter module. . . . .	27
3.9. ATLAS muon spectrometer. . . . .	30
3.10. ATLAS trigger system. . . . .	32
3.11. Overview of the L1 trigger. . . . .	33
3.12. Sliding windows for the CP. . . . .	35
3.13. Sliding windows for the JEM. . . . .	36
3.14. Prescales for L1 and HLT. . . . .	37
4.1. Jet levels in ATLAS. . . . .	40
4.2. Jet calibration schemes. . . . .	43
4.3. Pileup correction in JES calibration. . . . .	45
4.4. Jet energy response. . . . .	46
5.1. Multijet topology. . . . .	51
5.2. Dijet asymmetry. . . . .	53
5.3. Pseudorapidity requirements for CM and MM. . . . .	55
5.4. Jet Trigger Efficiencies. . . . .	56
5.5. Dijet asymmetry for a not fully efficient trigger. . . . .	57
5.6. TCM example. . . . .	58
6.1. Azimuthal separation and soft radiation suppression requirement. . . . .	62
6.2. Dijet asymmetry with contributions from different triggers. . . . .	65
6.3. Dijet asymmetry with fit. . . . .	66
6.4. Dijet asymmetry with trigger contributions, Pythia MC11b. . . . .	67

6.5. Comparison of the statistics for CM and TCM. . . . .	68
6.6. Dijet asymmetry with trigger contributions in the forward region. . . . .	69
6.7. Calorimeter response comparison between data and simulation. . . . .	71
6.8. Calorimeter response comparison between TCM and Standard Methods. . . . .	72
6.9. Statistical and systematical uncertainties. . . . .	75
A.1. Calorimeter response 2010 comparison with Classical Method. . . . .	80
A.2. Calorimeter response 2010 comparison with Matrix Method. . . . .	81
B.1. Calorimeter response 2011 comparison between data and simulation, AntiK6. . . . .	83
B.2. Calorimeter response 2011 comparison between SM and TCM, AntiKt6 . . . . .	84
C.1. Trigger efficiency 2012. . . . .	85
C.2. Calorimeter response comparison between data and simulation 2012. . . . .	87

---

# List of Tables

2.1. Fermions of the SM. . . . .	5
2.2. Bosons of the SM. . . . .	5
5.1. Pseudorapidity bins. . . . .	54
5.2. AntiKt4 $p_T^{avg}$ bins. . . . .	57
6.1. ATLAS trigger setup 2011. . . . .	64
A.1. Jet trigger used in the 2010 analysis. . . . .	79
A.2. AntiKt4 $p_T^{avg}$ bins for 2010. . . . .	79
B.1. AntiKt6 $p_T^{avg}$ bins. . . . .	82
C.1. AntiKt4 $p_T^{avg}$ bins for 2012. . . . .	86
C.2. ATLAS trigger setup 2012. . . . .	88

---

# Bibliography

- [1] ATLAS COLLABORATION. *Observation of a new particle in the search for the Standard Model Higgs boson with the ATLAS detector at the LHC* . Phys.Rev.Lett.B **716** (2012) 1.
- [2] CMS COLLABORATION. *Observation of a new boson at a mass of 125 GeV with the CMS experiment at the LHC*. Phys.Rev.Lett.B **716** (2012) 30.
- [3] ATLAS COLLABORATION. *In-situ pseudo-rapidity inter-calibration to evaluate jet energy scale uncertainty and calorimeter performance in the forward region*. ATLAS Conference Note, ATLAS-CONF-2010-055, CERN, Geneva (2010).
- [4] D. GILLBERG, J. LACEY, R. KING, G. BROWN, C. SUHR, Y. DAVYGORA, A. BAAS, T. CARLI, JB. SAUVAN, M. RELICH AND A. TAFFARD. *In situ jet pseudorapidity intercalibration of the ATLAS detector using dijet events in  $\sqrt{s} = 7$  TeV proton-proton 2011 data*. ATLAS Conference Note, ATLAS-COM-CONF-2012-079, CERN, Geneva (2012).
- [5] S. L. GLASHOW. *Partial-symmetries of weak interactions*. Nuclear Physics **22** (1961) 579.
- [6] S. WEINBERG. *A Model of Leptons*. Phys.Rev.Lett. **19** (1967) 1264.
- [7] J. GOLDSTONE, A. SALAM, AND S. WEINBERG. *Broken Symmetries*. Phys.Rev. **127** (1962) 965.
- [8] N. CABIBBO. *Unitary Symmetry and Leptonic Decays*. Phys.Rev.Lett. **10** (1963) 531.
- [9] M. KOBAYASHI AND T. MASKAWA. *CP-Violation in the Renormalizable Theory of Weak Interaction*. Phys.Rev.Lett. **49** (1973) 652.
- [10] B. PONTECORVO. *Neutrino Experiments and the Problem of Conservation of Leptonic Charge*. Soviet Journal of Experimental and Theoretical Physics **26** (1968) 984.
- [11] J. BERINGER ET AL. (PARTICLE DATA GROUP) *Review of Particle Physics*. Phys.Rev. **D86** (2012) 1 .
- [12] P. W. HIGGS. *Broken Symmetries and the Masses of Gauge Bosons*. Phys.Rev.Lett. **13**(1964) 508 .
- [13] F. ENGLERT AND R. BROUT. *Broken Symmetry and the Mass of Gauge Vector Mesons*. Phys.Rev.Lett. **13** (1964) 321.

- [14] G. S. GURALNIK, C. R. HAGEN AND T. W. B. KIBBLE. *Global Conservation Laws and Massless Particles*. Phys.Rev.Lett. **13** (1964) 585.
- [15] A. DJOUADI. *The Anatomy of electro-weak symmetry breaking. I: The Higgs boson in the standard model*. Phys.Rept. **457** (2008) 1.
- [16] P. JENNI, M. NESSI, M. NORDBERG AND K. SMITH. *ATLAS high-level trigger, data-acquisition and controls: Technical Design Report*. Technical Design Report (TDR) ATLAS. CERN, Geneva (2003).
- [17] PAVEL WEBER. *ATLAS Calorimetry: Trigger, Simulation and Jet Calibration*. PhD thesis Heidelberg University (2008).
- [18] R. KEITH ELLIS, W. JAMES STIRLING AND B. R. WEBBER. *QCD and Collider Physics*. Cambridge University Press **8** (1996).
- [19] ATLAS COLLABORATION. *Measurement of inclusive jet and dijet production in pp collisions at  $\sqrt{s} = 7$  TeV using the ATLAS detector*. Phys.Rev.D **86** (2012) 014022.
- [20] S. DIMOPOULOS AND H. GEORGI. *Softly broken supersymmetry and SU(5)*. Nuclear Physics B **193** (1981) 150.
- [21] ATLAS COLLABORATION. *Hunt for new phenomena using large jet multiplicities and missing transverse momentum with ATLAS in  $4.7 \text{ fb}^{-1}$  of  $\sqrt{s} = 7$  TeV proton-proton collisions*. JHEP **2012** (2012) 176.
- [22] ATLAS COLLABORATION. *The ATLAS Experiment at the CERN Large Hadron Collider*. JINST **3** S08003, (2008).
- [23] EUROPEAN ORGANIZATION FOR NUCLEAR RESEARCH (CERN). *LHC Machine*. CERN, Geneva, 2008. JINST **3** S08001, (2008).
- [24] ATLAS COLLABORATION. *ATLAS Experiment - Public Results*. URL: <https://twiki.cern.ch/twiki/bin/view/AtlasPublic/>.
- [25] CERN COLLABORATION. *European Organization for Nuclear Research*. URL: <http://public.web.cern.ch/public/>.
- [26] M. CAPEANS, G. DARBO, K. EINSWEILLER, M. ELSING, T. FLICK, M. GARCIA-SCIVERES, C. GEMME, H. PERNEGGER, O. ROHNE AND R. VUILLERMET. *ATLAS Insertable B-Layer Technical Design Report*. Technical Design Report (TDR) ATLAS-TDR-019, CERN, Geneva, (2010).
- [27] ATLAS COLLABORATION. *ATLAS Insertable B-Layer Technical Design Report Addendum*. Technical Design Report (TDR) ATLAS-TDR-019-ADD-1, CERN, Geneva (2012). Addendum to ATLAS-TDR-019.
- [28] R. ACHENBACH ET AL. *The ATLAS Level-1 Calorimeter Trigger*. JINST, **3** P03001 (2008).
- [29] B. ANDERSSON, G. GUSTAFSON, G. INGELMAN AND T. SJÖSTRAND. *Parton fragmentation and string dynamics*. Physics Reports **97** (1983) 31.

- [30] D. GILLBERG. *A Study of Jet Response in the  $D\bar{O}$  Calorimeters*. Master thesis, Lund Institute of Technology (2004).
- [31] ATLAS COLLABORATION. *Expected Performance of the ATLAS Experiment - Detector, Trigger and Physics*. CERN-OPEN-2008-020 (2009).
- [32] G. P. SALAM. *Towards Jetography*. Eur.Phys.J.C **67** (2010) 637.
- [33] G. P. SALAM AND G. SOYEZ. *A Practical Seedless Infrared-Safe Cone jet algorithm*. JHEP **0705** (2007) 086.
- [34] M. CACCIARI, G. P. SALAM, AND G. SOYEZ. *The Anti- $k(t)$  jet clustering algorithm*. JHEP **4** (2008) 63.
- [35] ATLAS COLLABORATION. *Jet energy scale and its systematic uncertainty in proton-proton collisions at  $\sqrt{s}=7$  TeV in ATLAS 2010 data*. ATLAS Conference Note, ATLAS-CONF-2011-032, CERN, Geneva (2011).
- [36] ATLAS COLLABORATION. *In-situ jet energy scale and jet shape corrections for multiple interactions in the first ATLAS data at the LHC*. ATLAS Conference Note, ATLAS-CONF-2011-030, CERN, Geneva (2011).
- [37] ATLAS COLLABORATION. *Probing the measurement of jet energies with the ATLAS detector using photon+jet events in proton-proton collisions at  $\sqrt{s} = 7$  TeV*. ATLAS Conference Note, ATLAS-CONF-2012-063, CERN, Geneva (2012).
- [38] ATLAS COLLABORATION. *Probing the measurement of jet energies with the ATLAS detector using  $Z$ +jet events from proton-proton collisions at  $\sqrt{s} = 7$  TeV*. ATLAS Conference Note, ATLAS-CONF-2012-053, CERN, Geneva (2012).
- [39] ATLAS COLLABORATION. *Probing the jet energy measurement at the TeV-scale using the multi-jet balance technique in proton-proton collisions at  $\sqrt{s} = 7$  TeV*. ATLAS Conference Note, ATLAS-CONF-2011-029, CERN, Geneva (2011).
- [40] C. SUHR. *Jet Trigger Studies for  $\eta$  Intercalibration*. Talk given in the 'Jet Trigger Signature Group Meeting', Nov 2011.
- [41] V. LENDERMANN, J. HALLER, M. HERBST, K. KRÜGER, H.-C. SCHULTZ-COULON AND R. STAMEN. *Combining Triggers in HEP Data Analysis*. Nuclear Instruments and Methods in Physics Research A **604** (2009) 707.
- [42] D. W. MILLER, A. SCHWARTZMAN AND D. SU. *Pile-up jet energy scale corrections using the jet-vertex fraction method*. Internal Note, ATL-PHYS-INT-2009-090, CERN, Geneva (2009).
- [43] D. W. SCOTT. *On optimal and data-based histograms*. Biometrika **66** (1979) 605.
- [44] D. GILLBERG. Private Communication.
- [45] M. BEGEL. *Jet Triggers in 2012*. Talk given in the 'SM Jet Physics meeting', Feb 2012.



---

# Danksagung

Am Ende meiner Arbeit möchte ich noch alljenen danken ohne die diese Arbeit nicht möglich gewesen wäre.

Als erstes möchte ich Herrn Prof.Dr. Hans-Christian Schultz-Coulon danken, dass er mir die Möglichkeit gegeben hat, dieses spannende Thema zu bearbeiten. Seine engagierte Art hat es mir ermöglicht das aktuelle Geschehen beim ATLAS Experiment kennenzulernen und selbst mitzugestalten. Herrn Dr. Klaus Reygers möchte ich ganz herzlich danken, dass er sich direkt bereit erklärt hat diese Arbeit als Zweitgutachter zu lesen.

Ein besonderer Dank geht an Dr. Rainer Stamen für seine kompetente Betreuung und für das geduldige und sorgfältige Korrekturlesen der Arbeit. Ich habe viel von ihm gelernt in dieser Zeit. Außerdem hat mich seine einmalige Art das ein oder andere Mal zum schmunzeln gebracht. Auch Dr. Victor Lendermann möchte ich danken, der mich besonders am Anfang mitbetreut hat und von seinem fundierten Wissen hat profitieren lassen.

Ohne Yuriy Dragunov eh...Davygora wäre diese Arbeit ebenfalls nicht möglich gewesen. Yuriy ist einer der verrücktesten Menschen die ich kenne und er kann schneller tippen als denken, was gelegentlich in 'uuuups...Aless, ich glaub ich hab deine Daten gelöscht!?' geendet hat. Aber er ist ebenfalls einer der hilfsbereitesten Menschen die ich kenne und er hatte immer Zeit mir bei meinen (2467841±5478) Fragen und Problemen mit Rat und Tat zur Seite zu stehen. Außerdem hat er dafür gesorgt, dass es in unserem Büro nie langweilig war und immer genug Gummibärchen als Nervennahrung in der Nähe waren. Vielen Dank, Yuriy.

Sahill Poddar und Heiko Laier möchte ich dafür danken, dass sie meine Arbeit Korrektur gelesen haben und gute Vorschläge für Verbesserungen hatten.

Außerdem möchte ich den gesamten ATLAS und ILC Gruppen danken, für die entspannte Atmosphäre, die netten Gespräche beim Mittagessen und den vielen Kuchen. Besonders bedanken möchte ich mich bei Tobias Harion, Konrad Briggel die immer ein offenes Ohr für mich hatten und mich so motiviert, unterstützt oder abgelenkt haben. Ebenfalls danken möchte ich Patrick Eckert, der gelegentlich meinen Computer überzeugen konnte weiterzuarbeiten, wenn ich mal wieder 'Kommunikationsprobleme' mit diesem hatte. Nicht zu vergessen, die 'regelmäßigen' Boulder- und Kletterabende (in variierender Besetzung) mit Tobias Harion, Felix Müller, Veit Scharf, Konrad Briggel, Dennis Schultz und Christian Graf, die für lustige Abwechslung gesorgt haben.

Ebenfalls sehr herzlich danken möchte ich Sebastian Niesporek, der mich immer unterstützt hat und besonders in letzter Zeit großes Verständnis für meine Arbeitszeiten gezeigt hat.

Zu guter Letzt möchte ich meinen Eltern und meiner Schwester danken. Ihr habt immer an mich geglaubt und mich bei allem unterstützt was ich machen wollte. Ohne euch hätte ich dieses Studium niemals erfolgreich beenden können. Vielen Dank!



Erklärung:

Ich versichere, dass ich diese Arbeit selbstständig verfasst habe und keine anderen als die angegebenen Quellen und Hilfsmittel benutzt habe.

Heidelberg, den (Datum)

.....